Final Report on the Structural Assembly Demonstration Experiment (SADE)

SSL Report 16–87

David L. Akin
Raymond A. Mills
Mary L. Bowden

MIT Space Systems Laboratory
Department of Aeronautics and Astronautics
Massachusetts Institute of Technology
Cambridge, Massachusetts

July 20, 1987

prepared for the

National Aeronautics and Space Administration
George C. Marshall Space Flight Center
Huntsville, Alabama

Contract Number NAS8-34959

INTRODUCTION

The Structural Assembly Demonstration Experiment (SADE) Program was conceived at the NASA Marshall Space Flight Center in 1980-81. The underlying concept of this experiment was to create a near-term Shuttle flight experiment focusing on the deployment and erection of structural truss elements. Although the exact configuration of the truss changed repeatedly over the life of the project, an attempt was always made to maintain a structural configuration relevant to some planned future space program. Thus, the structural configuration evolved throughout the project from the 10ft cubic truss of the Vought Corporation to a 5ft truss planned for use in the Science and Applications Space Platform (SASP) program. Various other augmentations were considered for incorporation, but always the core of the experiment consisted of a linear trusswork structure, with some cells deployed by the shuttle Remote Manipulator System (RMS) and some cells built up from individual struts by shuttle crew in extravehicular activity (EVA). An artist's concept of the "baseline" SADE structure is shown in Figure 1.

One of the unusual features of this program is that, thoughout its life, the SADE experiment was a program in search of a constituency. Thus, at various times the structure did and did not include automatically deployable cells, heat pipes, tip masses, reflective coatings, and mechanical and impulsive actuators. It is therefore somewhat ambiguous to speak of the "baseline" SADE structure, as this was subject to almost monthly revision. However, the involvement of the MIT Space Systems Laboratory in this experiment centered on two aspects. The initial (and primary) involvement of the SSL concerned the operational aspects of structural erection, especially including EVA assembly and RMS deployment. This interest grew from an accumulated data base of EVA manual assembly tests performed by MIT in the Marshall Neutral Buoyancy Simulator since January, 1980. A second interest area concerned the structural dynamics of the assembled truss, along with measurement of the applied loads during the assembly procedure. Thus, one of the important tasks of the MIT study team was to analyze the expected dynamic behavior of the SADE truss, and plan for the incorporation of a limited instrumentation system to obtain data on these structural issues.

This publication is the final report of the MIT work on the SADE experiment, performed under contract number NAS8-34959 for the NASA Marshall Space Flight Center (James Harrison, contract monitor). The activities of the MIT Space Systems Laboratory can be summarized in three major areas: preparing and conducting neutral buoyancy simulation

Figure 1
Artist's Concept of Complete SADE Structure

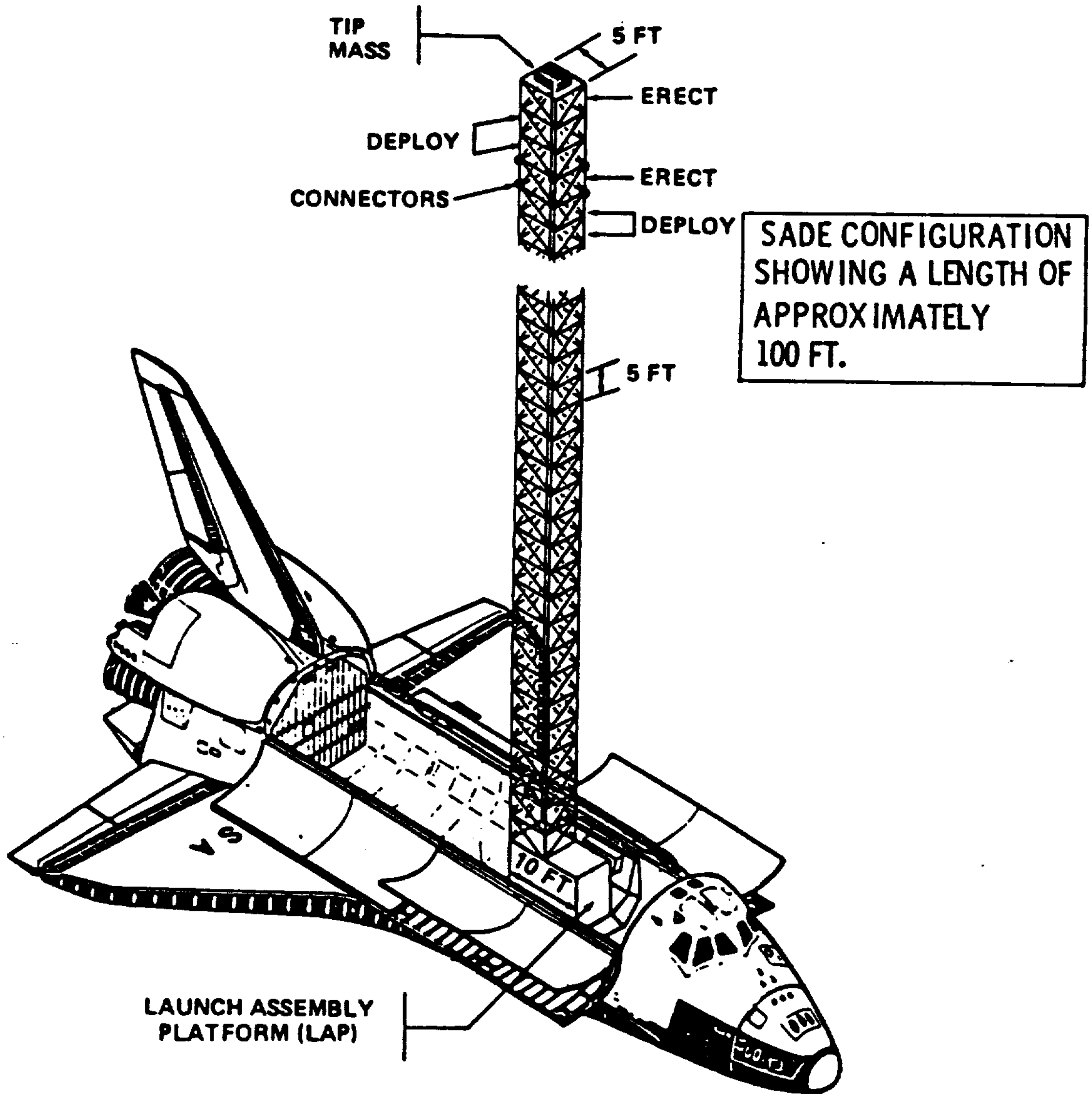

test series; producing a formal SADE Experiment Plan; and studying the structural dynamics issues of the truss structure. Each of these will be summarized in the following sections of the main body of this report, and covered in depth in individual appendices

NEUTRAL BUOYANCY TESTING

The SADE Program included four series of neutral buoyancy tests, over the two-year active period of the program. These neutral buoyancy tests were planned and carried out by MIT at the NASA Marshall Neutral Buoyancy Simulator, and resulted in substantial refinement of the SADE experimental objectives and methodology.

The first test series (NB-50A) was performed during the month of March, 1983, and focused on the design of the erectable module. During this test, a single cell was repeatedly assembled and disassembled by neutral buoyancy test subjects. This series incorporated the first test of the Launch Assembly Platform (LAP) design, and evaluation of the operational implications of the tip mass planned for incorporation into the final structure. Two tip masses were used during this test series: the first, constructed by NASA MSFC, was built to the envelope of the planned flight tip mass, to be used for investigating crew interfaces, launch restraints, etc. The second, designed and constructed by MIT, had in neutral buoyancy the full 5000lb mass of the flight tip mass, and was used to study the ability of the test subjects to manipulate such a large mass. Both tip masses proved to be easy to maneuver, and further use of the full-mass unit was discontinued for later test series. A typical assembly from this test series is shown in Figure 2.

The second test series (NB-50B) was held in August, 1983. The intent of this test was to go beyond the single-cell erection, and look at tasks more representative of the end-to-end SADE activities under consideration. Since the neutral buoyancy versions of the SADE deployable truss had not been completed, the MIT Space Systems Laboratory designed and fabricated a mockup of the two-cell deployable section. This mockup was a rigid truss, which could be slid down through the LAP on a sliding track arrangement. Thus, the EVA test subjects built the first cell on top of the deployable mockup, which was then slid upwards out of the LAP by a combination of manual force and RMS motion. A lower assembly fixture (the "mousetrap") was then swung across the top of the LAP, providing the location for completion of the lower assembled cell, to which the mockup of the deployable structure was mated. A four-cell SADE structure was the end result of this assembly procedure, as shown in Figure 3. This test series started to identify limitations in applied force levels obtainable from the RMS, as well as positioning accuracy limitations

Figure 2

Single SADE Assembled Cell from NB-50A

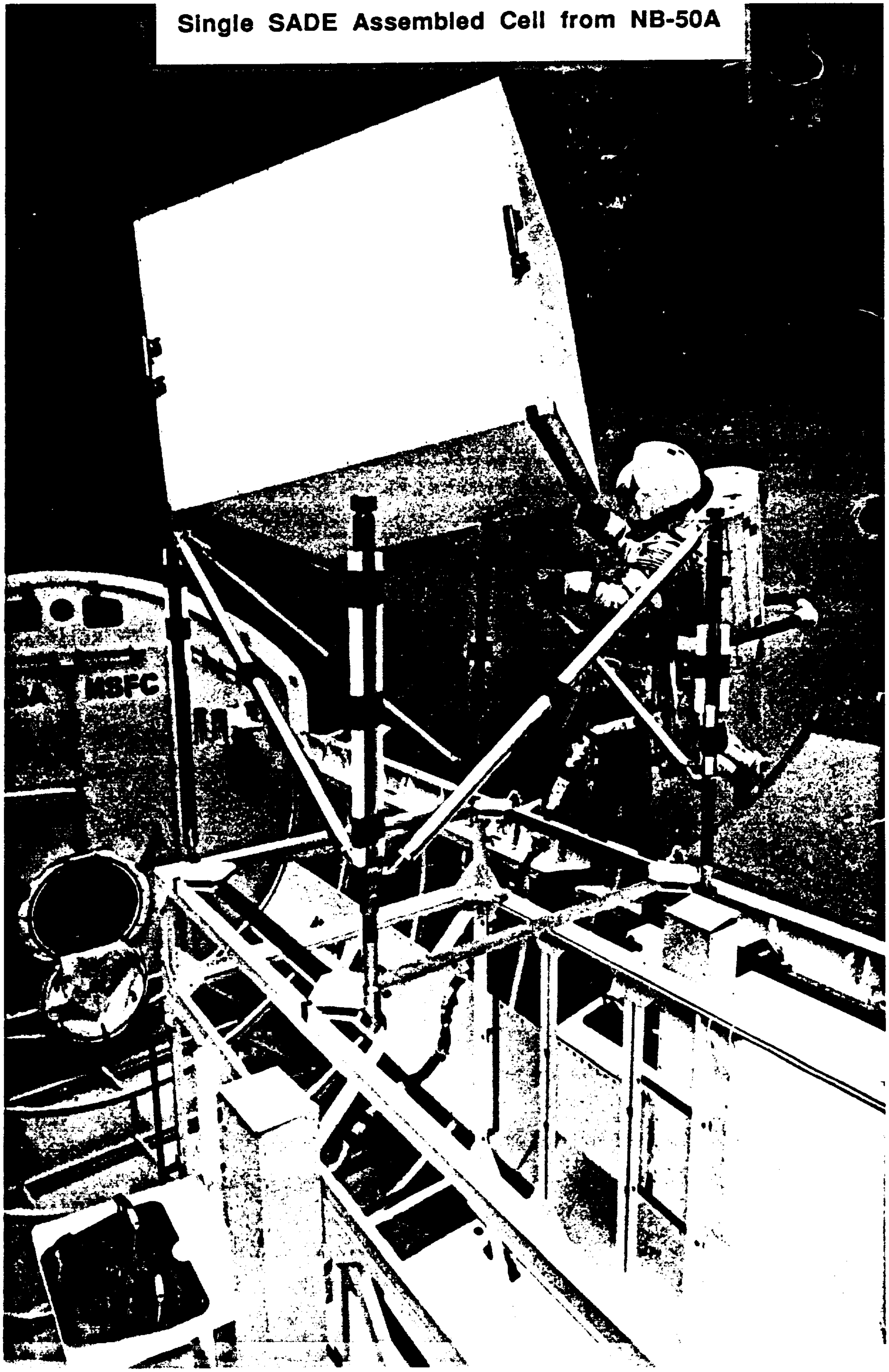

Figure 3
SADE Deployable Mockup from NB-50B

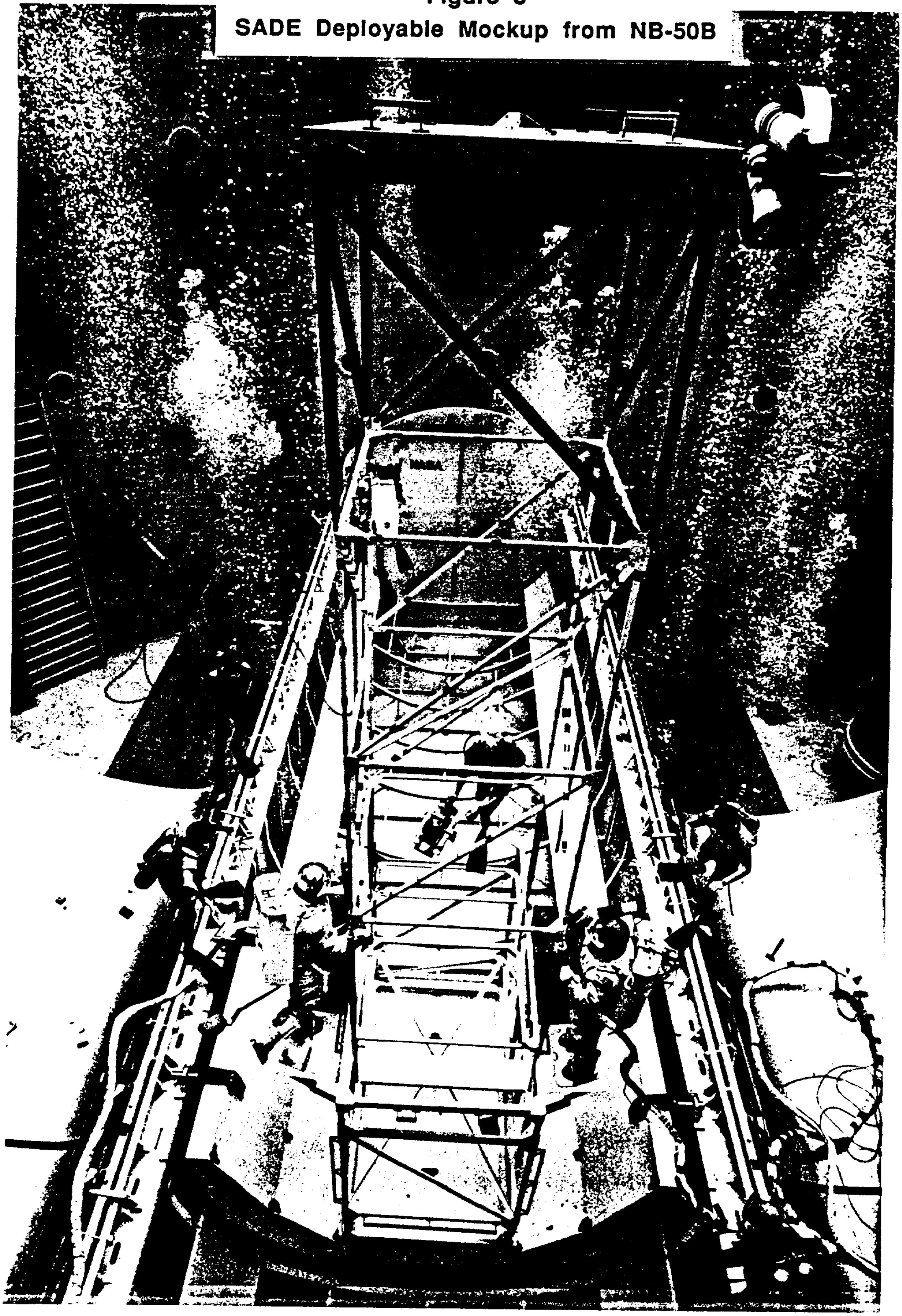

that were dealt with by final manual manipulation of the sections as they were joined. Modifications were also made to the type and number of structural connectors used, based on problems encountered with individual connector designs during the previous neutral buoyancy test series.

With the NB-50C tests in June, 1984, a functional deployable cell was incorporated for the first time into the assembly procedure. No launch support structure was available for the deployed cells, so the deployable module merely rested in the top of the LAP during the assembly of the top cell, and was then unfolded by the RMS and/or the EVA subjects. The structural configuration used during this test is shown in Figure 4. This test showed some difficulties in pure RMS deployment, as the latching mechanisms on the telescoping diagonal struts did not reliably engage under RMS actuation forces. As in the NB-50B tests with a mockup of the two-cell deployable section, this test was limited in water depth to four total cells of the structure.

Much effort was exerted to discover techniques by which the full seven-cell structure might be assembled in the neutral buoyancy tank. Since the seven cells formed a 35ft truss structure, there was not enough room to construct it vertically upwards, due to the height of the LAP and its mounting position in the payload bay mockup. It was suggested that two sections of the MSFC NBS shuttle bay mockup might be placed vertically on the tank wall, to allow the structure to be built horizontally across the diameter of the tank. This would allow the full construction of the truss, even with the height of the LAP mounted in the shuttle bay mockup. Although the preliminary hardware to perform this action was fabricated and tested, it was felt that this would require too much time from a busy NBS schedule to allow the rotation of the shuttle bay sections into the vertical arrangement. There were also problems with realistic mounting arrangements for the forward payload bay video cameras and remote manipulator system, which were needed for the test operations.

Due to the difficulties associated with the vertical test orientation of the payload bay, the decision was made for NB-50D (August, 1984) to accept the limitations of the vertical assembly procedure. In order to maximize the assembled hardware, one section of the shuttle payload bay mockup was removed, and the LAP placed directly on the floor of the neutral buoyancy tank. This allowed the construction of two assembled and two double-cell deployed modules, for a total six-cell structure (Figure 5). Some problems were associated with this operation, however: of particular nuisance was the proximity of the test subjects

Figure 4
Four-Cell SADE Structure from NB-50C

Figure 5

Six-Cell SADE Structure from NB-50D

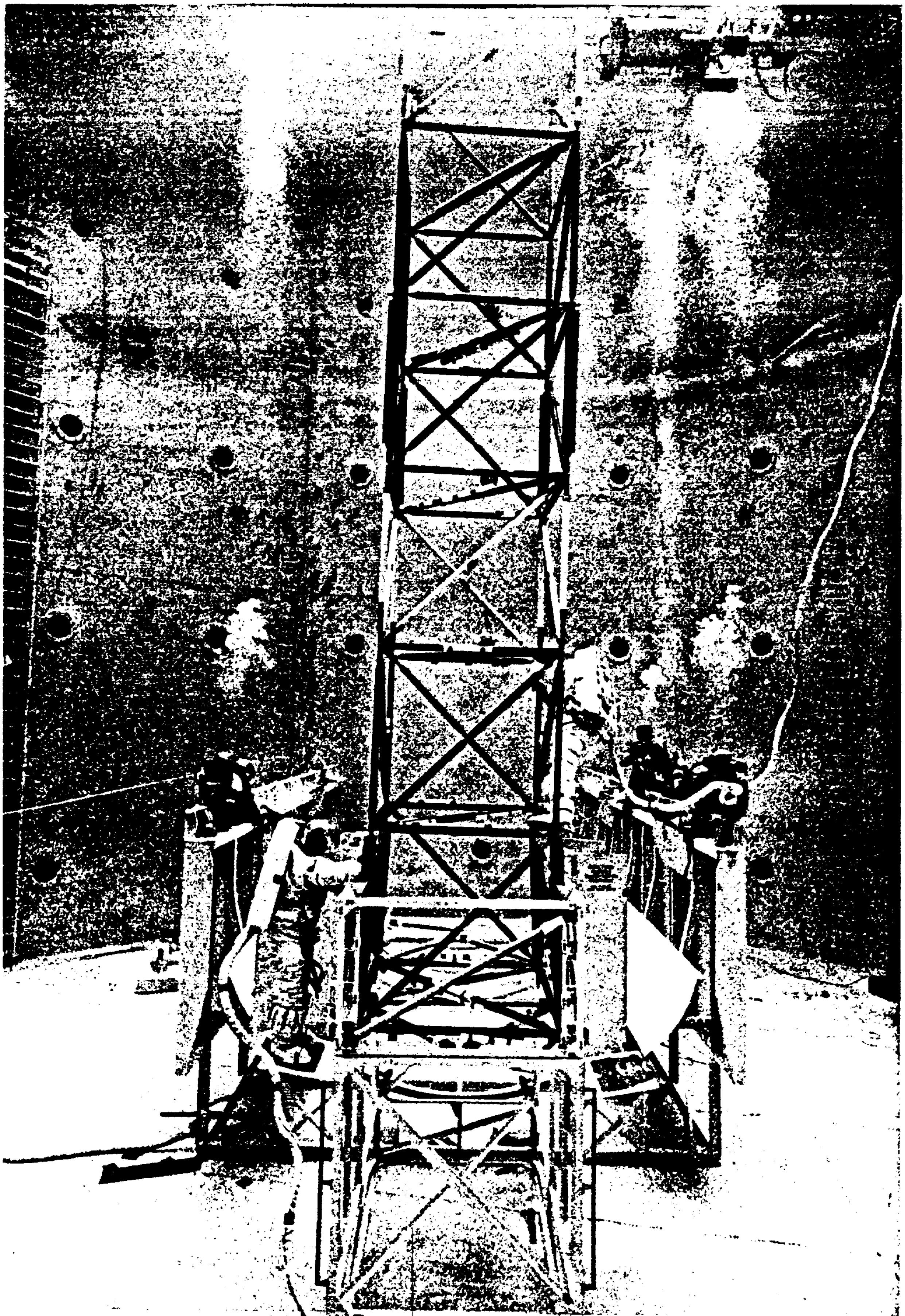

ORIGINAL PAGE IS
OF POOR QUALITY

to the bottom of the tank. It turned out that even leaning back could drop the pressure suit's regulator to an equivalent depth (including suit internal pressure) greater than 40 ft. This would necessitate the use of the 50ft dive tables for the test subject, which in several instances aborted active test runs for the much shorter bottom times available under this diving protocol.

NB-50D activities also included the use of a launch restraint fixture for the deployable cells, which proved to be less than a total success. In addition, changes were indicated in the choice of connectors for the assembled cells, and in the mockups to incorporate EVA overhead associated with the instrumentation system. For this reason, two further series of SADE tests were planned. A test in January, 1985 was to have verified the final configuration of the structural hardware, and would have incorporated the instrumentation system connections into the EVA procedures. A further test series in the summer of 1985 was to have been an all-up end-to-end test of SADE, including vertical orientation of the payload bay, and the full construction of seven bays with flight-configuration holddowns and support interfaces. Both of these test series were cancelled with the termination of the SADE program. As the NB-50D activities represent the most detailed SADE neutral buoyancy tests completed, the summary report from this test series is included in this final report as Appendix A.

EXPERIMENT PLANNING SUPPORT

As part of the MIT contract, the SSL participated in the formal development of the SADE Experiment Plan. This document went through several iterations, as the purposes and auxiliary experiments of the program changed over time. As mentioned above, the primary emphasis of the experiment was to correlate neutral buoyancy activities to the same tasks performed in space, to obtain data on the manual assembly and RMS-aided deployment of structures in the flight environment, and to obtain any structural data (on both the assembly process and the completed structure) which might be obtained without large additional expenditures on instrumentation. The formal SADE Experiment Plan, as produced by MIT, is included in this report as Appendix B. This plan was undergoing revisions at the termination of the SADE program. It was planned to incorporate the information from the later neutral buoyancy simulations (including the planned January 1985 test) into the final experiment baseline, and to produce the revised experiment plan concurrently with the all-up SADE neutral buoyancy test in the summer of 1985.

STRUCTURAL DYNAMICS ANALYSIS

The original impetus for the SADE experiment was the structural assembly aspect. However, it was felt that it would be unfortunate to construct a structure, without obtaining some information of the dynamics at the same time. While some members of the structures community were uninterested in SADE since it was not specifically designed as a structural dynamics experiment, the MIT experiment team felt strongly that some useful data could be obtained from SADE, without redefining the entire structure to meet dynamics goals. As part of this effort, the SSL performed an in-depth analysis on the dynamics of space structures, focusing on the SADE truss to obtain information necessary to decide upon the proper number and placement of sensors to maximize data return from limited instrumentation. This dynamics report is included herein as Appendix C.

CONCLUSIONS AND RECOMMENDATIONS

The SADE Program was (arguably) the first to address the issue of a near-term space test of assembly and deployment activities. Although the programmatic aspects of the SADE experiment were not within the scope of the MIT activities, it might be asserted that the biggest problem of SADE was an implicit assumption that a flight experiment which "only" did structural assembly was not of sufficient interest to merit the costs required. Thus, while SADE searched about for alternate investigations and configurations, it was (to some extent) superceded by the EASE and ACCESS experiments, which were kept tightly focused on structural assembly objectives.

SADE represented an interesting and ambitious project, which still has several attractive features even following the successful EASE/ACCESS experiments of STS 61-B. It addressed the issue of deployable trusses, and included an innovative use of the shuttle remote manipulator system to provide the actuation force for deployment and retraction. It addressed the issue of interfaces between manually assembled and automatically deployed structure, and had the capability to look at manual structural deployment as an alternative to the automated systems. It included an instrumentation system to measure loads applied during the assembly process, as well as loads present in the completed structure under normal "operations". The cubic truss of the SADE structure was much closer in configuration to the current Space Station truss than either the EASE or ACCESS configurations, and incorporated a number of connector designs that would have provided a wealth of data on alternative latching mechanisms and motions for EVA manual assembly. Later versions incorporating many automatically deployed cells would have produced a large truss structure with low natural frequencies, which would have been of interest in structural dynamics modeling of the Space Station. Alternative experiments such as heat pipe installation and thermal recoating would have likewise added to the data base of space spation operations.

Much of the data still needed for the Space Station and subsequent programs could have been obtained from the SADE flight experiment. Although, with the hiatus in shuttle flights and restrictions on the manifest for the foreseeable future, it is difficult to imagine a resurrection of SADE, it is very likely that future programs will require further flight experiments that, like EASE and ACCESS, will have a substantial legacy from the SADE program.

APPENDIX A: NB-50D SUMMARY REPORT

NB-50D SADE TEST OBJECTIVES

- HARDWARE EVALUATION:
  - MIT SUPPLIED ASSEMBLY HARDWARE
  - MSFC SUPPLIED DEPLOYABLE HARDWARE
  - RESTRAINT AND PERIPHERAL HARDWARE
- PROCEDURES EVALUATION:
  - ASSEMBLY PROCEDURES FOR TWO ERECTABLE CELLS
  - ASSEMBLY PROCEDURES FOR TWO DEPLOYABLE MODULES
  - DISASSEMBLY AND STOWAGE PROCEDURES
  - MANIPULATION OF TIP MASS
- ASSESSMENT OF EVA TIMELINES
- EVALUATION OF SHUTTLE EMU's

NOTE:

THE GOAL OF THIS TEST SERIES WAS TO PERFORM AS MUCH HARDWARE AND PROCEDURES EVALUATION AS POSSIBLE WITHOUT REQUIRING THAT THE SHUTTLE BAY MOCKUP IN THE NEUTRAL BUOYANCY TANK BE TURNED VERTICAL.

NB-50D SADE TEST HARDWARE

- MIT SUPPLIED HARDWARE:
  - 24 ASSEMBLED CELL STRUTS
  - 2 RESTRAINT BOXES FOR STRUTS
  - MODIFICATION HARDWARE FOR TIP MASS
  - INSTRUMENTED STRUT AND DATA COLLECTION SYSTEM

- MSFC SUPPLIED HARDWARE:
  - 2 DEPLOYABLE MODULES
  - RESTRAINT FIXTURE
  - LAUNCH/ASSEMBLY PLATFORM (LAP)
  - TIP MASS AND PORTABLE GRAPPLE FIXTURE
  - RMS AND OTHER SUPPORT HARDWARE

- STRUCTURAL CONNECTORS USED IN EACH ASSEMBLED CELL:
  - 4 MIT SLEEVE-LOCKING JOINTS
  - 4 VOUGHT QUICK CONNECTS (MODULE-TO-MODULE CONNECTORS)
  - 4 LANGLEY CONNECTORS (SIDE-LOCK, THUMB-RELEASE)
  - 4 VOUGHT CLEVIS COUPLERS

NB-50D SADE TEST RUNS
(8/15/84-8/23/84)

RUN NUMBER	ASSEMBLY/ DISASSEMBLY TIMES	NOTES
1	A - 52:28	Foot restraints not used
	D - 32:29	Stiff clevis springs
2	A - 39:54	Tip mass grapple fixture broken
	D - 41:20	Stiff clevis springs
3	A - 31:31	-
	D - 36:20	Stiff clevis springs
	A - 39:10	No RMS, all manual
4	A - 25:20	-
	D - 24:18	-
	A - 18:01	No RMS, incomplete assembly
5	A - 35:51	Tip mass installed manually
	D - 23:45	-
6	A - 39:36	-
	D - 29:24	-
	A - 25:30	Instrumented strut installed
	D - 19:30	-

- All of the structural assemblies (A) and disassemblies (D) liste above consisted of two assembled cells and two deployable modules, yielding a six-cell structure.
- Test subjects for all six runs were Dave Akin and Mary Bowden.
- Times listed above are in min:sec, and show learning trends as illustrated in the following graphs.

LEARNING RATE

NB-50D 6-CELL ASSEMBLY

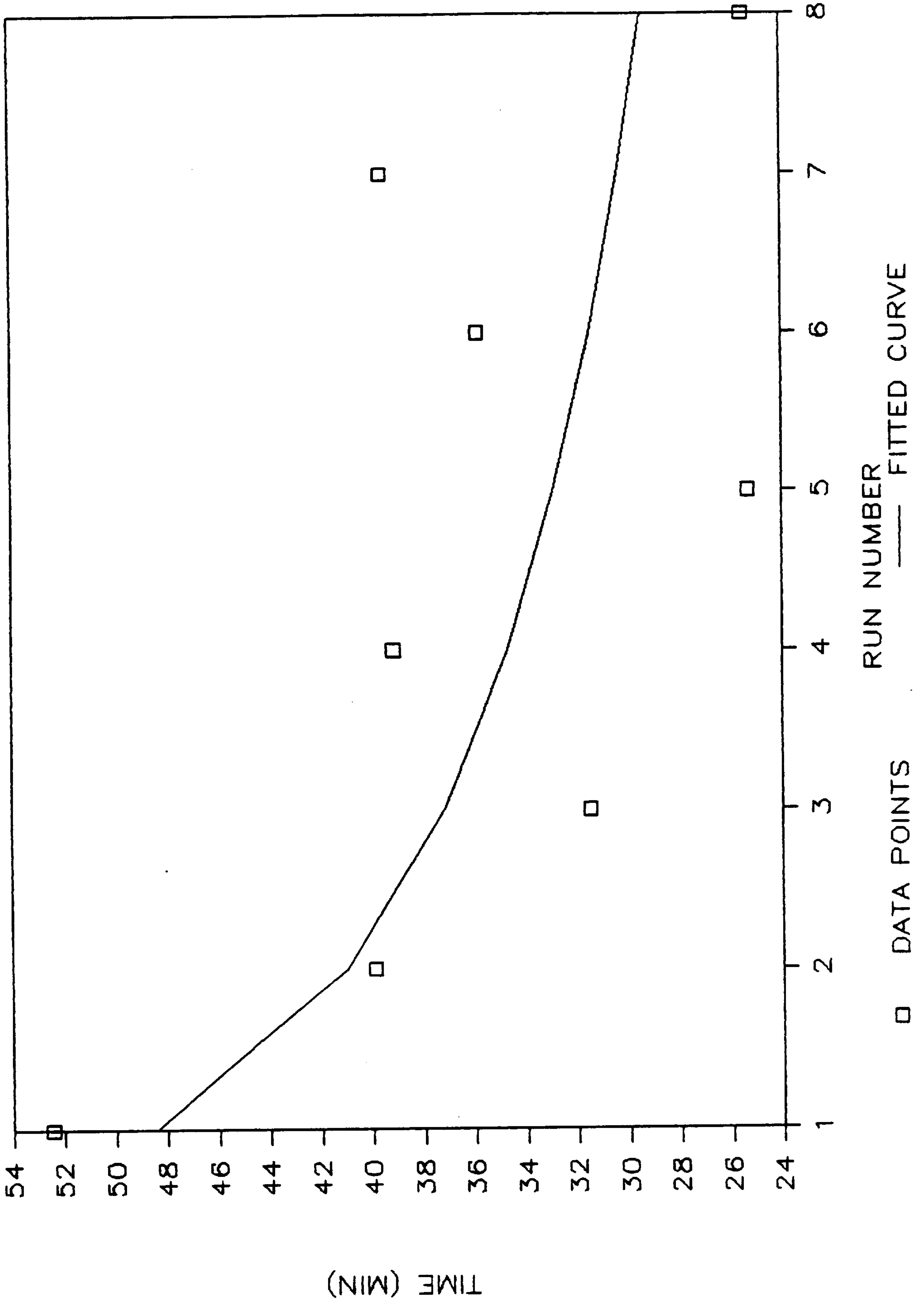

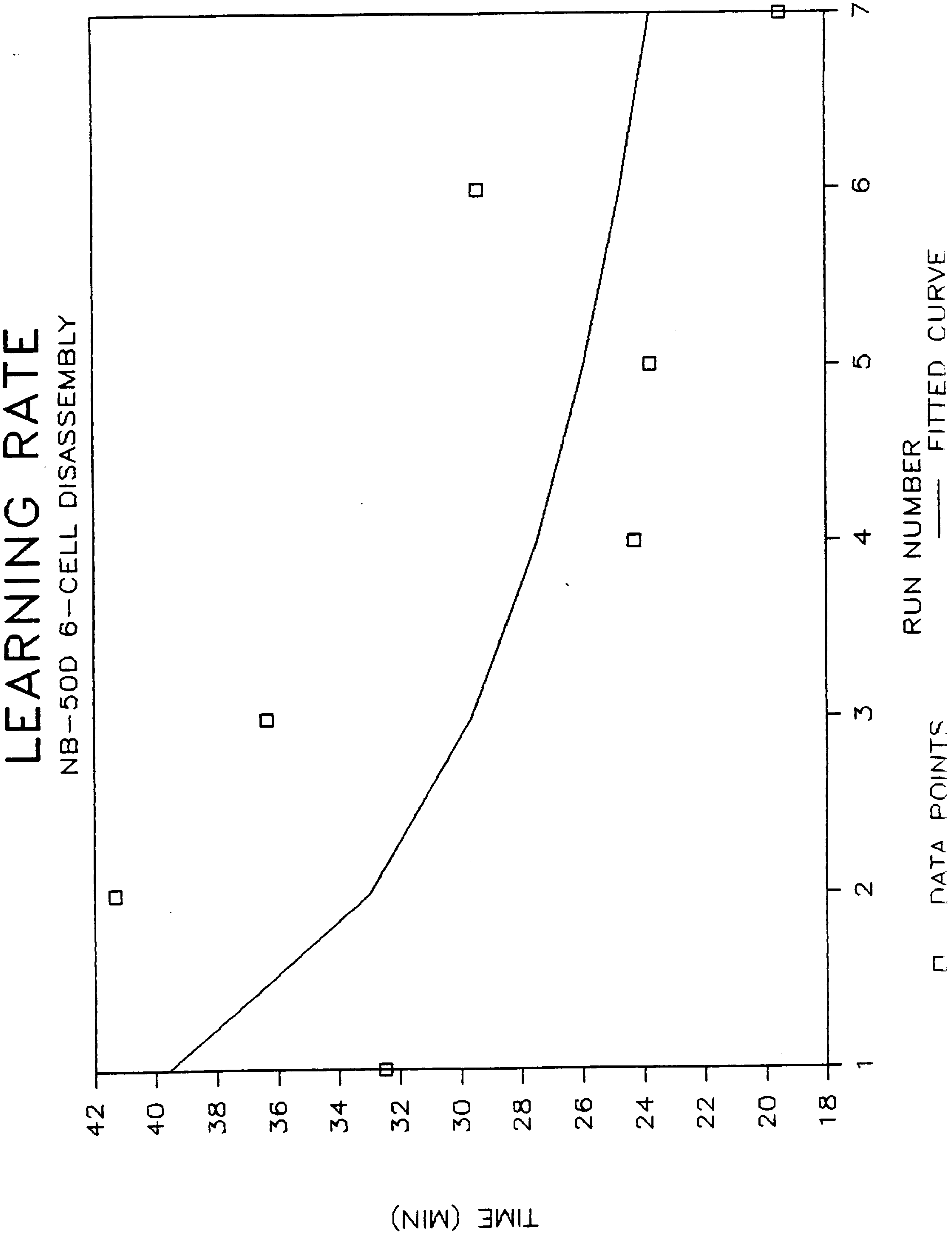
LEARNING RATE
NB—50D 6—CELL DISASSEMBLY
TIME (MIN)
42
40
38
36
34
32
30
28
26
24
22
20
18
RUN NUMBER
1
2
3
4
5
6
7
□ DATA POINTS
—— FITTED CURVE

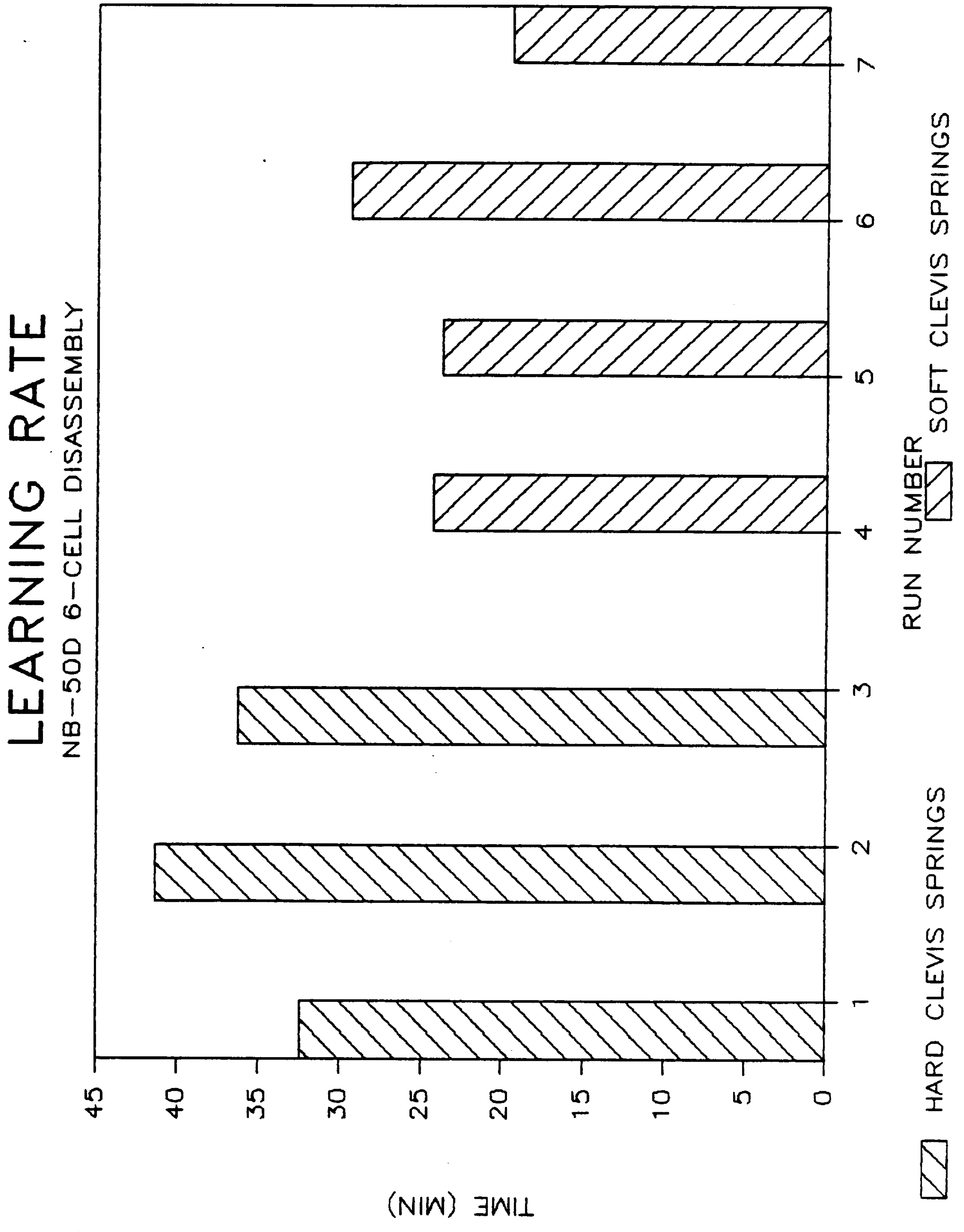
LEARNING RATE
NB-50D 6-CELL DISASSEMBLY
TIME (MIN)
0
5
10
15
20
25
30
35
40
45
RUN NUMBER
1
2
3
4
5
6
7
▨ HARD CLEVIS SPRINGS
▨ SOFT CLEVIS SPRINGS

SADE TEST RESULTS - HARDWARE EVALUATION

1. ASSEMBLED CELL HARDWARE AND RESTRAINT BOXES

- THE MIT JOINTS AND THE VOUGHT QUICK-CONNECTS BOTH WORKED VERY WELL ON THE LONGITUDINAL STRUTS. THE MIT JOINT COULD BE IMPROVED BY GUARANTEEING THAT THE PUSH BUTTON - SLIDE SLEEVE RELEASE MOTION CAN BE RELIABLY PERFORMED WITH ONE HAND.

- THE VOUGHT CLEVIS COUPLERS ON THE DIAGONAL STRUTS WERE FOUND TO BE UNACCEPTABLE BECAUSE OF MECHANICAL DIFFICULTIES DURING BOTH ASSEMBLY AND DISASSEMBLY. THE SUGGESTION WAS MADE TO REPLACE THIS CONNECTOR WITH ANOTHER ONE, YET TO BE DETERMINED, PERHAPS THE LANGLEY/ACCESS CONNECTOR. [MIT] THE LANGLEY CONNECTORS ON THE DIAGONALS WORKED WELL, EXCEPT THAT IT WAS OCCASIONALLY DIFFICULT TO DETERMINE IF THE CONNECTOR WAS FULLY LOCKED.

- ONE OF THE FOUR DIAGONALS IN EACH ASSEMBLED CELL IS SHORTER THAN THE OTHER THREE, BECAUSE OF THE DESIGN OF THE DEPLOYABLE MODULES. THIS WAS FOUND TO BE A MINOR INCONVENIENCE DURING ASSEMBLIES.

- THE STRUT RESTRAINT BOXES PERFORMED SATISFACTORILY, BUT IT WAS NOTED THAT A DOOR THAT FOLDS BACK OUT OF THE WAY IS PREFERABLE, AND NEW DOOR LATCHES ARE NEEDED. [MIT]

II. DEPLOYABLE MODULES

- DEPLOYMENT OF THE DEPLOYABLE MODULES WAS VERY DIFFICULT BECAUSE ONLY A SMALL COMPONENT OF THE UPWARD LIFTING RMS FORCE ACTED ALONG THE TELESCOPING DIAGONALS TO LOCK THE LATCHES, WHILE THE LATCHES BECAME INCREASINGLY TIGHT JUST BEFORE LOCKING. AN OVER-CENTER LATCHING MECHANISM COULD PROBABLY SOLVE THIS PROBLEM. [MSFC]

- RETRACTION OF THE DEPLOYABLE MODULES WAS ALSO MADE EXTREMELY DIFFICULT BECAUSE OF THE LATCHES ON THE DIAGONALS, WHICH SIMPLY COULD NOT BE OPENED OR HELD OPEN IN A PRESSURE SUIT GLOVE EVEN WITH THE AID OF THE PLIERS-TYPE TOOL DESIGNED FOR THIS PURPOSE. A RELEASABLE OVER-CENTER LATCH SHOULD SOLVE THIS PROBLEM, AND WOULD ALSO ELIMINATE THE NEED FOR A DISASSEMBLY TOOL. [MSFC]

- ONE OF THE DIAGONALS USED IN EACH ASSEMBLED CELL IS SHORTER THAN THE OTHER THREE,AS MENTIONED ABOVE, BECAUSE OF PARTICULARITIES IN TWO OF THE NODES OF THE DEPLOYABLE MODULE, DATING BACK TO A DESIGN WHICH ALLOWED THE STRUCTURE TO BE DEPLOYED AND RETRACTED AUTOMATICALLY. MAKING THESE NODES SIMILAR TO THE OTHERS ON THE DEPLOYABLE MODULE WOULD ELIMINATE THIS DISTINCTION. [MSFC]

- THE HAT SHAPED STRUTS OF THE DEPLOYABLE MODULES WERE FOUND TO HAVE TWO PROBLEMS: FIRST, THE FLANGES OVERLAPPED AND GOT HUNG UP ON THE TRACKS AND SIDES OF THE RESTRAINT FIXTURE; AND SECOND, THE EDGES WERE TOO SHARP AND THEREFORE HAZARDOUS TO THE SUIT GLOVES. [MSFC]

III. LAUNCH/ASSEMBLY PLATFORM AND RESTRAINT FIXTURE

- THE LAUNCH/ASSEMBLY PLATFORM (LAP) AND ESPECIALLY THE RESTRAINT FIXTURE BOTH NEED MORE HANDRAILS INSTALLED ALONG ALL TRANSLATION PATHS. [MSFC/MIT]

- THE STOWAGE LOCATION FOR THE TIP MASS AT THE BOTTOM OF THE LAP IS NO LONGER COMPATIBLE WITH THE DIMENSIONS OF THE TIP MASS, BECAUSE THIS WAS MODIFIED TO CONFORM TO THE NEW CONFIGURATION OF THE ASSEMBLED CELLS. THIS PROBLEM CAN MOST EASILY BE SOLVED BY BUILDING A NEW TIP MASS WITH COMPATIBLE DIMENSIONS. [MIT]

- THE GUIDE TRACKS ON THE RESTRAINT FIXTURE ARE COMPLETELY UNACCEPTABLE IN THEIR PRESENT CONFIGURATION, BECAUSE THEY DO NOT ADEQUATELY CONTROL THE UPWARDS AND DOWNWARDS SLIDING OF THE DEPLOYABLE MODULES. TRACKS THAT CLOSE SOMEWHAT AROUND THE BACK OF THE SLIDER BALLS, AND BALLS THAT ARE OFFSET FURTHER AWAY FROM THE DEPLOYABLES, SHOULD IMPROVE THE SITUATION CONSIDERABLY. [MSFC]

- THE T-HANDLE FORKLATCHES INSTALLED ON THE FORWARD TRACKS OF THE RESTRAINT FIXTURE NEED A GREATER RANGE OF ADJUSTABILITY UP AND DOWN, IN ORDER TO PROPERLY LOCK THE DEPLOYABLES IN PLACE. A MODIFIED VERSION OF THESE LATCHES, WITH SMALLER ACTUATION HANDLES FOR EXAMPLE, MUST BE INSTALLED ON THE MIDDLE TRACKS. IN ADDITION, TRACKS AND PERHAPS FORKLATCHES COULD BE INSTALLED ON THE AFT END OF THE RESTRAINT FIXTURE, ELIMINATING THE TAILGATE MECHANISM. [MSFC]

IV. TIP MASS

- MORE HANDRAILS SHOULD BE INSTALLED ON THE TIP MASS. [MSFC]
- THE JOINT FIXTURES INSTALLED ON THE BOTTOM SIDE OF THE TIP MASS WERE FOUND TO INTERFERE WITH THE STOWAGE TRACKS IN THE BOTTOM OF THE LAP. THESE FIXTURES WILL HAVE TO BE MODIFIED IN ORDER TO USE THIS STOWAGE LOCATION IN THE NEXT TEST SERIES. [MIT]
- THE PORTABLE GRAPPLE FIXTURE (PGF) USED DURING THE NB-50D TESTS WAS NOT REMOVABLE FROM THE TIP MASS. THIS DID NOT ALLOW INSTALLATION PROCEDURES FOR THE PGF TO BE TESTED. THE PGF SHOULD BE FIXED BY REMOVING A BROKEN PIP PIN, AND REPLACING IT WITH A NEW ONE. [MSFC]

V. RMS

- USE OF THE RMS WOULD BE GREATLY FACILITATED, AND TIMELINES IMPROVED, BY THE INTEGRATION OF A FLIGHT-TYPE CONTROL SYSTEM AT THE RMS WORKSTATION. [MSFC]
- THE RMS SNARE GRAPPLING MECHANISM DOES NOT PERFORM AS IT SHOULD, EVEN IN MANUAL MODE, BECAUSE OF THE LACK OF LATCHING MECHANISMS ON THE CLOSURE AND RETRACTION LEVERS OF THE END-EFFECTOR. ULTIMATELY, BOTH OF THESE OPERATIONS (CLOSURE AND RETRACTION) SHOULD BE CONTROLLED BY THE RMS OPERATOR AT THE WORK STATION. [MSFC]

VI. CAMERAS

- AN EVALUATION OF FLIGHT REALISTIC VIDEO COVERAGE COULD NOT BE PERFORMED DURING THIS TEST SERIES BECAUSE OF THE ABSENCE OF ALL NECESSARY CAMERAS. AT LEAST BOTH FORWARD BULKHEAD CAMERAS ARE ESSENTIAL FOR THE NEXT TEST SERIES. IDEALLY, ONE SHOULD HAVE A WIDE-ANGLE ZOOM LENS INSTALLED. [MSFC]
- THE AFT BULKHEAD CAMERAS, AND BOTH THE RMS ELBOW AND WRIST CAMERAS WILL ALSO BE USED TO SOME EXTENT IN FLIGHT. [MSFC]

SADE TEST RESULTS - PROCEDURES

I. ASSEMBLY PROCEDURE

- o THE PROCEDURE FOLLOWED FOR ALL OF THE ASSEMBLED CELLS WAS THAT OUTLINED AT THE END OF THE LAST SERIES OF SADE TESTS: FIRST, ALL FOUR LONGITUDINALS WERE INSTALLED AT THE LOWER END; THE UPPER SECTION OF STRUCTURE (EITHER TIP MASS OR DEPLOYABLE MODULE) WAS THEN BROUGHT INTO POSITION BY THE RMS AND ATTACHED MANUALLY; THE FOUR DIAGONAL STRUTS WERE THEN INSTALLED. THIS PROCEDURE WORKED WELL, AND ALLOWED BOTH TEST SUBJECTS TO WORK ON THEIR SIDE OF THE STRUCTURE EFFICIENTLY AND INDEPENDENTLY.
- o IT SHOULD BE NOTED THAT THE ASSEMBLED STRUTS DO NOT GO TOGETHER EASILY, UNLESS EACH ONE IS EXACTLY THE RIGHT LENGTH AND THE ASSEMBLED CELL IS NOT BEING STRESSED EXTERNALLY. THE RMS, FOR EXAMPLE, ALMOST INEVITABLY PUTS SOME LOAD ON THE ASSEMBLED CELL WHILE IT IS HOLDING THE UPPER PORTION OF THE STRUCTURE ATTACHED TO IT.

II. DEPLOYMENT PROCEDURE

- o THE PROCEDURE OF DEPLOYING THE STRUCTURE WITH THE RMS WHILE THE TEST SUBJECTS PROVIDE GUIDANCE ON EACH SIDE WORKS WELL. ALL DEPLOYMENT PROBLEMS ENCOUNTERED WERE A DIRECT RESULT OF HARDWARE PROBLEMS DESCRIBED ABOVE.

III. STOWAGE PROCEDURE

- o STOWAGE OF THE STRUCTURE WAS PERFORMED BY REVERSING THE PROCEDURES USED DURING THE ASSEMBLY PROCESS. THUS MOST OF THE PROBLEMS ENCOUNTERED DURING STOWAGE WERE IDENTICAL TO THOSE LISTED ABOVE, AND RESULTED PRIMARILY FROM INADEQUATE HARDWARE.

SADE NB-50D TEST SUMMARY

I. ACCOMPLISHMENTS OF THIS TEST

- THE SADE STRUCTURE WAS ASSEMBLED IN ALMOST ITS FULL FLIGHT CONFIGURATION.
- ALL BASIC HARDWARE WAS EVALUATED, MODIFICATIONS OUTLINED, AND RESPONSIBILITIES ASSIGNED SO APPROPRIATE CHANGES CAN BE MADE.
- NEW HARDWARE REQUIREMENTS WERE IDENTIFIED AND PROCUREMENT INITIATED IN MOST CASES.
- ALL BASELINE ASSEMBLY, DEPLOYMENT, AND STOWAGE PROCEDURES (EXCEPT THOSE PERTAINING TO THE PORTABLE GRAPPLE FIXTURE) WERE VERIFIED.
- A PRELIMINARY ASSESSMENT OF FLIGHT-REALISTIC TIMELINES WAS OBTAINED FOR THE BASIC ASSEMBLY AND DISASSEMBLY OPERATIONS.

II. RECOMMENDATIONS FOR FURTHER TESTS

THE FOLLOWING TWO TEST SERIES ARE RECOMMENDED TO BRING SADE CLOSER TO FLIGHT:

1. A TEST IN JANUARY, 1985, TO EVALUATE NEW SUPPORT HARDWARE, TO DETERMINE WHICH CONNECTOR SHOULD BE USED TO REPLACE THE VOUGHT CLEVIS COUPLER, AND TO TEST NEW CAMERA AND INSTRUMENTATION SYSTEMS.

2. A TEST DURING THE SUMMER OF 1985 TO ASSEMBLE THE ENTIRE SEVEN CELL STRUCTURE; THIS WILL REQUIRE THAT THE CARGO BAY BE TURNED VERTICAL IN THE NEUTRAL BUOYANCY TANK. THIS TEST WILL ALSO INCLUDE ALL PERIPHERAL HARDWARE AND SYSTEMS AS CLOSE TO FLIGHT CONFIGURATION AS POSSIBLE.

SADE - JANUARY 1985 TEST SERIES

APPROACH

Four cells of the SADE structure will be built during this test series: two assembled cells and one double-cell deployable module. This will allow enough room for the LAP to be placed on a pallet in the payload bay, so that all of the lower interfaces of the structure with the Shuttle can be checked. Thus, for example, slidewire tethers can be used, recorder box mockups wil be installed, and more realistic work envelopes will be simulated.

NEW HARDWARE

- Three new configurations of the assembled cell, each one differing only by the joints used to replace the Vought clevis couplers, which were found to be unacceptable:
    - two inch diameter Langley connectors
    - "new" Langley connectors with the locking sleeve
    - MIT joints.
- Modifications of tip mass:
    - new connector fixtures to accomodate the new connectors listed above, and to allow stowage of tip mass in tracks on LAP
    - more handrails installed
    - repaired portable grapple fixture
- Mockups of recorder boxes

NEW HARDWARE (CONTINUED)

- NEW INSTRUMENTATION SYSTEM:
  - MOCKUPS OF ELECTRICAL CONNECTORS INSTALLED ON A REPRESENTATIVE NUMBER OF STRUTS, AND MOCKUPS OF A DATA COLLECTION BOXES
  - AN ACTIVE SET OF STRAIN GAGES INSTALLED ON ONE STRUT FOR COLLECTION OF LOADS DATA.

- NEW VIDEO SYSTEM:
  - FORWARD BULKHEAD CAMERAS, ONE OF WHICH SHOULD HAVE A WIDE-ANGLE ZOOM LENS
  - RMS CAMERAS
  - A DATA COLLECTION PROCEDURE USING TRACKING TARGETS INSTALLED ON THE EMU'S AND BACKPACKS, AND SOFTWARE AVAILABLE FOR ANALYSIS OF BODY DYNAMICS DATA.

SADE SUMMER 1985 TEST SERIES

APPROACH

THE SADE TEST SERIES TO BE CONDUCTED DURING THE SUMMER OF 1985 SHOULD BE A TEST OF THE FULL ALL-UP SADE FLIGHT EXPERIMENT. THIS WILL INCLUDE AT LEAST THE FOLLOWING OBJECTIVES:

- VERTICALLY ORIENTED SHUTTLE BAY MOCKUP
- THE FULL SEVEN CELL SADE STRUCTURE
- THREE FINAL CONFIGURATION ASSEMBLED CELLS
- FLIGHT DESIGN LATCH FIXTURES ON THE DEPLOYABLE MODULES
- FLIGHT DESIGN RESTRAINT FIXTURE AND LAP
- FLIGHT TYPE CONTROL SYSTEM FOR RMS
- COMPLETE VIDEO COVERAGE SYSTEM (BULKHEAD AND RMS CAMERAS)
- INSTRUMENTATION SYSTEM FOR LOADS DATA

APPENDIX B: SADE EXPERIMENT PLAN

1.0 INTRODUCTION

Many large scale space systems envisioned for the next two decades of the US space program rely on the availability of structural platforms as a strongback for mounting scientific experiments, communication antennae, materials processing and fabrication modules, or living quarters. Because of the size requirements for these platforms, they clearly cannot be launched in finished form in the cargo bay of the shuttle orbiter. For this reason, it will be necessary to either deploy or assemble the structure while on orbit. A near term flight experiment to demonstrate these capabilities and to identify potential problems is presented here.

1.1 Purpose

A structural assembly demonstration experiment (SADE) is a critical first step in the development of large space structures. It will help to determine how best to go about assembling structures, and what role crewmen can play in the construction procedure.

The fundamental purposes of SADE are as follows:

1. To establish a quantitative correlation between earth-based assembly simulations and on orbit operations
2. To obtain assembly data relating to orbital assembly with the Manned Maneuvering Unit (MMU) and the Remote Manipulator System (RMS)
3. To study the structural dynamics and thermal characteristics of an intermediate-scale space structure in a realistic environment

1.2 Scope

The purpose of the SADE Experiment Plan is to outline and guide the development of the scientific objectives of this flight experiment. This document details the following tasks:

- Identification of experiment objectives
- Planning of experimental approach
- Data acquisition methods
- Data analysis techniques

1.3 Experiment Rationale

Neutral buoyancy is currently the most effective medium for ground-based simulation and testing of assembly operations. However, in order to have confidence in the validity of the simulation results, it is necessary to have a full understanding of the relationship between neutral buoyancy and on-orbit timelines. Clearly, a near-term flight experiment using hardware previously tested in neutral buoyancy, will yield quantitative correlation factors for a wide variety of assembly-related tasks. In addition, more general insight into the strengths and limitations of neutral buoyancy as a simulation medium can be obtained. It is imperative to have this knowledge if neutral buoyancy is to be used in the future to successfully predict the number of flights, days, and EVA sorties necessary to complete the construction of a larger scale space platform.

The second fundamental purpose of this experiment is to obtain manual assembly data, both quantitative data on such things as productivity, and qualitative data relating to procedures and hardware evaluation. For this reason, the flight structure should be designed from the beginning as an apparatus to be assembled by pressure suited subjects. Once complete, however, it should yield significant scientific and engineering structural data while on-orbit. In addition, this structure should have validity as a space platform in its own right, incorporating hardware which may be a development model for future space systems.

2.0 EXPERIMENT OBJECTIVES

The prime objectives of the Structural Assembly Demonstration Experiment can be subdivided into the following three categories:

1. Simulation Correlation
2. Assembly Factors
3. Structural Study

The objectives of each category are described briefly in this section.

2.1 Simulation Correlation

To correlate neutral buoyancy simulations with on-orbit operations, the first objective is to establish a timeline data base for assembly tasks, then to calculate the correlation factors for each task, and finally to extrapolate these correlation factors to other assembly tasks and structures. In addition to this quantitative analysis, a better understanding of the neutral buoyancy environment will be obtained from this analysis so that the simulation can be improved for future projects.

2.2 Assembly Factors

One objective under this section is to quantify extra-vehicular (EV) kinematics. By studying the motions of both the astronaut and the components manipulated, it is possible to gain a fundamental insight into the physics of extravehicular activity (EVA). By using the on-orbit experience to validate sophisticated computer models, an EVA procedures designer will be able in the future to perform initial neutral buoyancy tests on the computer, saving hardware and test costs, and reducing the load on the highly limited number of neutral buoyancy facilities. A further assembly objective is to evaluate, from the point of view of the user, the structural hardware and peripheral equipment used in this flight experiment, and to identify possible improvements for future use. The key parameters characterizing ease of assembly or deployment will also be identified. (For example, is length or moment of inertia the significant variable for beam alignment?)

2.3 Structural Study

Instrumentation will be installed on the structure to meet the following objectives: the lowest natural frequencies and modes of the structure will be quantified; the loads imposed on the structure by deployment, by EVA assembly, by MMU-augmented assembly, by RMS operations, and by shuttle vernier thrusters will be measured; and damping for the structure as a whole will be analyzed.

3.0 EXPERIMENTAL APPROACH

This section describes the experimental hardware, the preparatory tests prior to the flight, the procedures to be used on orbit, and the post flight data analysis and testing.

3.1 Experimental Hardware

The central part of this flight experiment is to construct and subsequently disassemble a hybrid deployable-erectable structure in the space shuttle cargo bay (see figure 1). The deployable structure chosen is a single-fold double cell module designed by Vought Corporation (see figure 2). Two of these modules will be deployed on orbit and joined together using an interconnect module of eight individually erected structural elements. The erectable structural elements consist of four longitudinal elements and four diagonal elements. In order to study the effect of moment of inertia of a structural element on ease of assembly, two of the longitudinals will be made of lightweight material, and two will be of heavy material; the diagonals will be made in a similar manner. This difference in density will result in significantly different moments of inertia for the eight erectable elements. Table 1 shows the structural characteristics of all the elements of the structure.

Four different connector designs will be used as joints between the eight structural elements and the deployable modules. Sixteen connections will need to be made (two ends for each of eight elements), so there will be four uses of each connector design. Table 2 defines the connectors that are currently being considered for this purpose.

A Launch/Assembly Platform (LAP), will secure the deployable modules in their folded configuration for launch and will also restrain during launch and return all other hardware necessary for this experiment. A flight data recorder will be mounted on the pallet to record structural and thermal data obtained from sensors distributed throughout the structure.

The deployment and assembly of this structure will be performed with the aid of the Remote Manipulator System (RMS), and the Manned Maneuvering Unit (MMU). Both of these assembly aids will be stowed in their usual configuration prior to use.

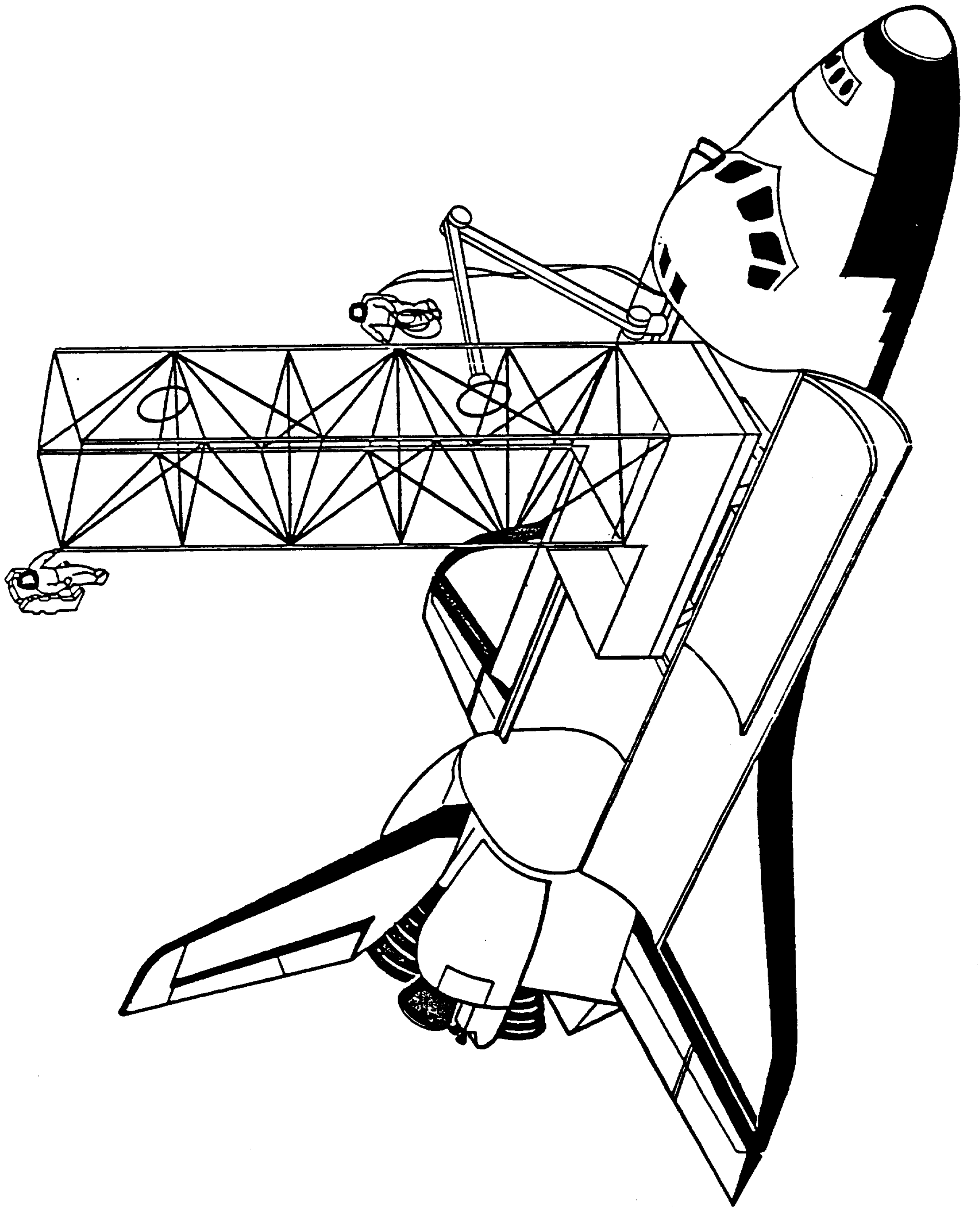

FIGURE 1 - SADE STRUCTURE

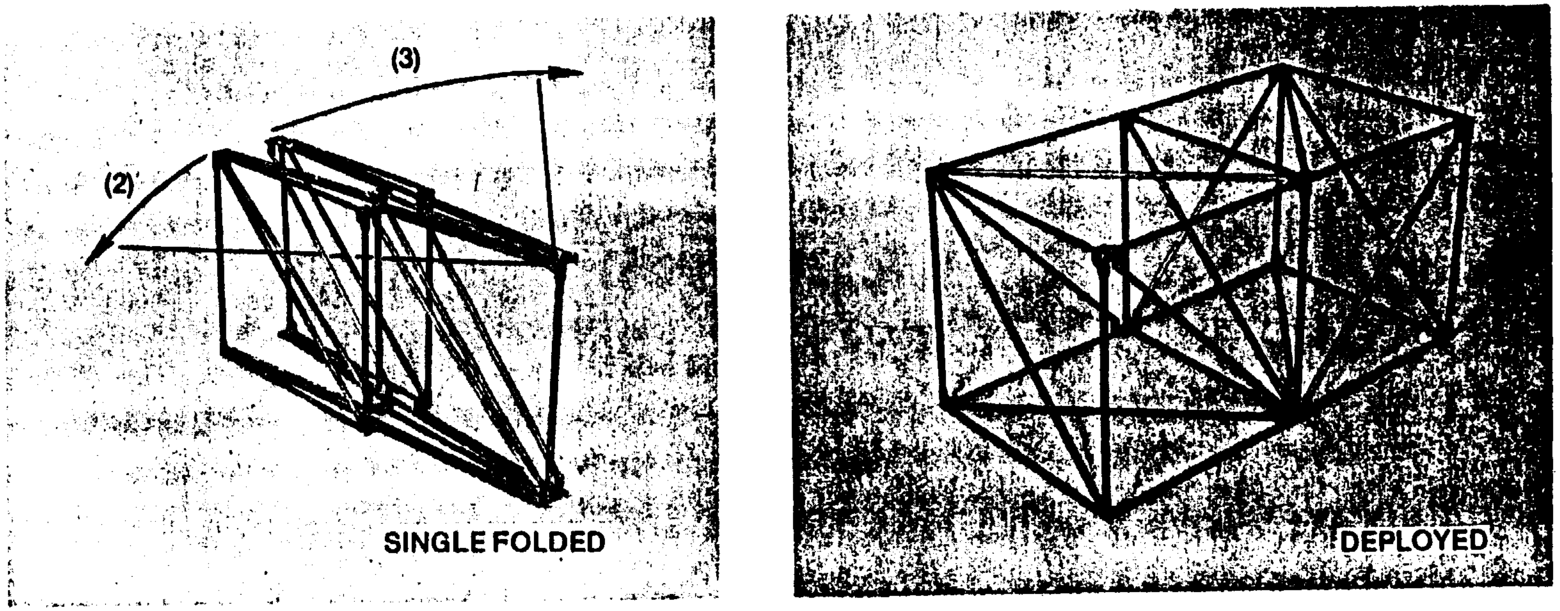

FIGURE 2 - DEPLOY SEQUENCE FOR SADE DEPLOYABLE MODULE

		RADIUS	THICKNESS	LENGTH	MASS	MOMENT OF INERTIA
DEPLOYED MODULE	LONGITUDINALS	3.175	0.089	300	1.438	4.31
	LATERAL/ VERTICALS	1.588	0.159	300	1.285	3.85
	DIAGONALS	1.588	0.159	424	1.816	10.88
INTERCONNECT	LIGHT LONGITUDINAL	1.905	0.089	300	0.844	2.53
	LIGHT DIAGONAL	1.905	0.089	424	1.193	7.15
	HEAVY LONGITUDINAL	1.905	0.635	300	14.907	44.72
	HEAVY DIAGONAL	1.905	0.635	424	21.069	126.25
	UNITS	cm	cm	cm	kg	kg m^2

TABLE 1 - STRUCTURAL CHARACTERISTICS OF SADE STRUCTURE

		LARC SNAP UNION	MIT CONNECTOR	VOUGHT CLEVIS COUPLER	VOUGHT AUTOLOCK COUPLER
ANGULAR TOLERANCE	HIGH			●	●
	LOW	●	●		
CAPTURE	YES	●		●	●
	NO		●		
RIGIDIZING	YES				
	NO	●	●	●	●
LATCHING	YES		●		
	NO	●		●	●

TABLE 2 - STRUCTURAL CONNECTORS FOR SADE STRUCTURE

3.2 Neutral Buoyancy Tests Prior to Flight

The neutral buoyancy tests that will be necessary prior to flight to attain the objectives listed in section 2, can be divided into three parts. The initial sequence of tests will be to define flight configuration hardware and an optimized set of assembly procedures , chosen so that all tasks can be performed in an identical manner in neutral buoyancy and in flight. This will enhance the correlation process significantly. The next test series will be devoted to verification of the hardware design and to further definition of the procedures. The third series of tests will be primarily to train the crew that will be assembling the structure on orbit. This is especially important so that a baseline timeline can be set up for comparison with the on-orbit results.

3.3 Test Procedures on orbit

The SADE experiment will take two six-hour EVA sessions to complete: one day to erect the structure, and one day to disassemble and stow it. The manpower allocation will be the same on both days: two crewmen will be EVA, one with the MMU, one without; one crewman on the aft flight deck, will control the video cameras, direct operations, and operate the RMS.

A preliminary set of procedures for erecting the SADE structure is shown in table 3, along with the primary data that is expected from each step. This is a "strawman" procedure that will serve primarily as a starting point for the early neutral buoyancy tests. Results of these early tests will no doubt modify the procedure to some extent, but the outline does indicate some of the more important operations that will be performed in flight:

- One deployable module will be unfolded using RMS, the other will be deployed with the MMU.
- Some of the manual assembly of structural elements in the interconnect structure will be performed with the subject in foot restraints, while some of it will have the subject out of foot restraints.
- Subjects will perform controlled alignment motions with structural elements both in and out of foot restraints, to evaluate the effect of mass and moment of inertia on body positioning, and to identify human control laws and applied torque levels as a function of foot restraints.
- A subject will translate along structure, once while carrying hardware and once without, so that loads imposed on structure by this process can be measured. Similarly, a subject with MMU will apply loads to the structure, to quantify these as well.

TASK	DATA OBTAINED ON
(1) UNSTOW TWO ELEMENTS OF INTERCONNECT CELL (LL, LD)	EVA OPERATIONS
(2) ROTATE EACH ELEMENT THROUGH 90° AND 180° IN FRONT OF CAMERA	HUMAN CONTROL LAWS & TORQUE LEVELS EFFECT OF MASS AND MOMENT OF INERTIA (WITH FOOT RESTRAINTS)
(3) INSTALL INTERCONNECT ELEMENTS ON FOLDED MODULE 1	ASSEMBLY IN FOOT RESTRAINTS CONNECTOR DESIGN
(4) REPEAT STEPS (1), (2), AND (3) FOR TWO MORE ELEMENTS OF INTERCONNECT CELL (HL, HD)	(AS LISTED ABOVE)
(5) ENGAGE GRAPPLE FIXTURE ON MODULE 1 WITH RMS	RMS OPERATIONS
(6) RELEASE MODULE 1 LAUNCH RESTRAINTS	EVA OPERATIONS
(7) DEPLOY MODULE 1 (CELLS 1 AND 2) WITH RMS	RMS DEPLOYMENT CAPABILITY

TABLE 3 - ASSEMBLY PROCEDURE: PART I

TASK	DATA OBTAINED
(8) Unstow 2 more elements of interconnect cell (LL, LD)	EVA operations
(9) Subject B translates along module 1 with LL element	Manual translation with hardware assembly loads
(10) Subject A moves to worksite at top of module 1 with LD	MMU translation with hardware
(11) Subjects rotate elements through 90° and 180° in front of cameras	Human control laws & torque levels Effects of mass & moment of inertia (without foot restraints)
(12) Connect elements to top of module 1	Assembly without body restraints Assembly loads
(13) Subjects translate back to launch assembly platform	Unencumbered manual translation Unencumbered MMU translation Assembly loads
(14) - (19) Repeat steps (8) through (13) with remaining 2 elements of interconnect cell (HA and HL)	(As listed above)

TABLE 3 - ASSEMBLY PROCEDURE: PART II

TASK	DATA OBTAINED
(20) SUBJECTS RELEASE MODULE 1 HOLDDOWNS	EVA OPERATIONS
(21) RMS MOVES MODULE 1 AND INTERCONNECT CELL UP, AFT, AND OUTBOARD PORT	MANIPULATION OF HIGH MOMENT OF INERTIA, LIGHTWEIGHT STRUCTURE WITH RMS
(22) RELEASE MODULE 2 LAUNCH RESTRAINTS	EVA OPERATIONS
(23) SUBJECT B DEPLOYS MODULE 2, CELL 1, MANUALLY	USE OF UNAIDED EVA FOR DEPLOYMENT
(24) SUBJECT A DEPLOYS MODULE 2, CELL 2, USING MMU	USE OF MMU FOR DEPLOYMENT
(25) SUBJECT B TRANSLATES TO TOP OF MODULE 2	UNENCUMBERED MANUAL TRANSLATION
(26) RMS ROTATES MODULE 1 180° AND BRINGS IT INTO POSITION OVER MODULE 2	MANIPULATION OF HIGH MOMENT OF INERTIA WITH RMS
(27) ATTACH INTERCONNECT CELL TO MODULE 2 WITH RMS GUIDED BY EVA CREW	INTEGRATED RMS/EVA ASSEMBLY OPERATIONS

TABLE 3 - ASSEMBLY PROCEDURE: PART III

3.4 Post Flight Tests

After the flight, the structural hardware used on orbit will be inspected to check for broken mechanisms. In addition, there is also the possibility of performing further neutral buoyancy tests if necessary; for example, if something unexpected happens in flight to prevent the crew from following established timelines.

4.0 DATA ACQUISITION

4.1 Time and Motion Data

Time and motion data for the two EVA crew members will be the primary source of the correlation data base. As such, collection of the necessary information for detailed time and motion analysis will be a high priority.

Besides serving as test conductor (reading off procedures to the EVA crew), the crew member on the aft flight deck will be responsible for direction and recording of video tape on the standard shuttle closed circuit television systems. Available camera angles will consist of the port and starboard forward and aft payload bay bulkhead mounts, and the RMS wrist and elbow cameras. It should be noted that RMS cameras will only be available for data collection when they are not required by the crew member in the port aft flight deck for RMS operations. Video tape data will be supplemented and backed up by a time lapse motion picture camera mounted in the aft flight deck, running at a rate no less than 1 frame/sec. This film camera will be mounted in such a location that a wide angle lense will pick up the maximum amount of crew activity, based on procedures developed in neutral buoyancy.

Since only one video channel may be recorded at a time, the interior crew member will be responsible for video mixing, as well as camera alignment. Experience with neutral buoyancy testing has shown that single-channel video can result in significant data loss, especially when two test subjects are working on separate tasks not in close proximity. In order to be assured of full correlation data, it will be necessary to have full time and motion data on each of the two EVA crew members. As part of the procedures checklist used in flight, closeups and significant camera angles will be listed for the camera operator. The time-lapse motion picture camera will be relied upon for data analysis of the second astronaut during video close-ups of the first, especially when the second is engaged in clearly evident activities such as translation. EVA timelines will be optimized to prevent the scheduling of tasks requiring video closeups when the other test subject is outside the vision angle of the film camera.

In addition to video and film records, crew members will be encouraged to give running verbal accounts of the assembly procedure, and their position on the timeline. This will allow another form of task time data, and will provide corroborating data for task times taken from the wide-angle view of the film camera. Actual time and motion analysis will be performed postflight: this procedure is covered in the following section.

4.2 Assembly Techniques

In addition to providing the majority of time and motion data, video tapes will also provide visual evidence of the relative ease of beam alignment, connector assembly, and so forth.

Body dynamics relates to the positioning of the body in weightlessness, and the human phase plane control laws for structural component alignment. While assembling the interconnect cell struts, the test subject will be required to rotate each strut through two 90 degree arcs, and one 180 degree one. These will be done such that the plane through which the beam is rotated is most nearly perpendicular to the sight vector from the recording video camera. The zoom setting of the camera will be such that the test subject's entire body will be visible on the screen. During post flight analysis, this will permit the beam position to be measured as a function of time, giving estimates for angular velocity by successive differencing and filtering. Image digitization of the resultant body motion will provide data on the forces applied, both to the beam and to the subject's work station on the structure.

Hardware evaluation and crew performance are highly subjective areas, which can best be quantified in terms of assembly time and difficulty. Completion times for each task will be found from videotapes, and by verbal marks given by the test subject when starting and completing the task. Difficulty of performing the task may be inferred by crew member cardiopulmonary rates, obtained through the EVA bioinstrumentation. It is important for this reason to have correlation marks of some sort between primary data collection media (video tapes and films) and the tapes of the bioinstrumentation readings. Crew qualitative evaluations will be given real time onto the audio track of the video tape, and discussed in more detail during post-flight debriefing.

4.3 Structural Data

Structural data will consist of strain gauge or load cell readings of stresses in the elements of the structure and of the launch assembly platform, along with accelerometer data from selected nodes and from the pallet (as an indicator of rigid-body orbiter motions). Sensors will be mounted to the structural elements prior to launch, to insure proper attachment procedures. Primary data recording will be performed by an LDEF experiment power and data system (EPDS), which receives data from sensors via wires connected by the EVA crew members. Since these wires cannot (in some cases) be attached until after the structure is complete, the load data during assembly will, if possible, be recorded on MIT solid state self-contained recorders (SSSCR's). These will be mounted on each structural element, and will be activated by the EVA crew. The EPDS will also have to be activated at the beginning of the run. After assembly, calibration of the sensors will be performed by loading the structure at a predetermined point by a known force (such as an MMU thrust at a specified node). Time of such loading will be noted by the test conductor, and entered into the flight log for calibration of the instrument recorders after the flight.

5.0 DATA ANALYSIS

5.1 Assembly Timeline Data Base

For the purposes of analysis, the entire SADE EVA procedure will be broken down into parts that are smaller and more specific at each level:

- First Level - the full set of extra-vehicular activities will be broken down into operations (e.g., cell deployment)
- Second Level - each operation will be broken down into component tasks (e.g., release launch restraints for module 1, cell 1)
- Third Level - each task will be broken down into component subtasks (e.g., activate latch safety release)

A data base will thus be established by recording the time for each operation, task, and subtask each time it is performed either underwater or on-orbit. A careful comparison can thus be made between the time required to perform a task in space and that required to perform the identical task underwater. In addition, time and effort spent on similar but different tasks in space (such as joining the various connectors) will be carefully studied.

5.2 Correlation Analysis

Simply comparing task times established in neutral buoyancy with those obtained on orbit will yield only a qualitative understanding of the difference between the two environments. A systematic statistical analysis of the flight experiment data, therefore, will also be performed to obtain quantitative correlation factors that are directly applicable to other neutral buoyancy tests and other assembly operations. This analysis will be carried out in the following manner:

- A chart showing timelines established on orbit in one column with the baseline timeline established in neutral buoyancy in a parallel column will be drawn up, so that it will be very apparent where the two procedures diverge and where they are most similar.
- Numerical factors for each subtask will then be calculated by computing the ratio of time spent on orbit for the subtask to time spent in neutral buoyancy for the same subtask. For example: if subtask 2.1.4, ingress foot restraints at work station B, takes 4:25 min on orbit and 3:36 min in neutral buoyancy, then the task time ratio for that specific subtask is 1.23.
- A more generally meaningful correlation factor will then be calculated by taking the average time spent for all the repetitions of a generic subtask. For example, if the foot restraints are ingressed 12 times during the assembly procedure the average time spent over these 12

repetitions will be compared with the same average established underwater.

- Multiple regression analyses will be performed for tasks which have more than one parameter. For example, ingressing foot restraints will require more or less time depending on local clearances, availability or absence of hand rails, and so forth. In this case, a time-variant linear regression analysis would be done, resulting in an equation for the time required to ingress foot restraints on orbit, as a function of the time required in neutral buoyancy. A variety of possible fit functions (logarithmic, power, exponential) will be tried for each of these multiple regressions, and the chosen model will be the curve fit with the highest coefficient of determination.
- Correlations will be performed for selected tasks based on MIT computer models of body motion in weightlessness. For example, the math model for translating a package indicates that the correct factor for nondimensionalizing the transport motion is

$$I(M+m)/MmDL$$

where I is the pitch moment of inertia of the EVA subject, M is the subject mass, m is the manipulated mass, and D and L are functions of the pressure suit dimensions. For manipulative translations, therefore, the nondimensionalized transfer times will be correlated between neutral buoyancy and space, as well as the raw times. Weighted linear regression correlation will also be performed, with weighting based on math model information of the specific task. This correlation procedure will apply to all tasks which can be accurately and reliably modeled. All correlations will include the coefficient of determination of the resultant curve fit.

- Based on the correlations obtained from the SADE flight, an EVA neutral buoyancy user's guide will be prepared, with details of extrapolation from SADE results to applicable correlation factors between general neutral buoyancy operations and expected timelines on-orbit.

5.3 Assembly Analysis

Body dynamics data will be digitized through the use of an X-Y digitizer attached to a video monitor, with a stop-motion video playback deck attached. Where necessary, data will be collected frame-by-frame: most of the data collection will be sufficient only to categorize gross body motions, and digitization frequencies will range down to .5 seconds/data point. Tracking targets on suit joints, backpack, and MMU will be necessary to allow location identification for sufficient accuracy in the digitizing process. Digitized body data will be stored on disk, and will be read into the computer for dynamic CAD reconstruction of body motion, comparison to math models to allow verification, and concurrent computer simulations with water drag to provide neutral buoyancy correlation independent of the time and motion data. At the same time, the beam alignment task data will be digitized, analyzed to provide beam angle as a function of time, differenced and filtered to provide angular velocity estimates as a function of time, and the phase plane control laws will then be generated, by plotting angular velocity versus angle.

EVA design criteria will be analyzed based heavily on crew comments, both during and after the assembly procedure. These comments will be the primary source of data for hardware evaluations from a user point of view. Video tapes will provide records of task time in performing the different tasks, while crew comments on the video tape will be used to find subjective reactions, as well as for refreshing the memories of the crew during post-flight debriefing. This information will be correlated with bioinstumentation sensor data to quantify the degree of difficulty of each assembly task. Learning on repetitious tasks will be analyzed in two ways: a power-law regresssion analysis on the task times (increase in speed) and on the net decrease in heart rate (decrease in difficulty). Productivity is the assembly rate at which the structure is completed. Fatigue will be found from the trends of heart rate or respiration as a function of time.

5.4 Structural Data Analysis

As mentioned earlier, structural data will be recorded on the LDEF experiment power and data system (EPDS), and possibly on the MIT solid-state self contained recorder (SSSCR), if that unit is qualified in time for flight. Wires for the EPDS sensors must be integrated into the structure, and connected by the EVA crew members. Data from strain gauges and accelerometers will be stored in essentially "raw" form in the EPDS.

With the development of the MIT system, data can be recorded in a variety of different forms, including digital waveform conversion, storage of Fourier coefficients, peak loads within a time frame, times of all structural loads exceeding a preset threshhold, and so on. Each SSSCR will be dedicated to its collection technique, and a number of such techniques will be tested for their utility in structural analysis. All sensors will be integrated on the structure prior to flight. Objectives of the structural loads study are to quantify loads placed on the structure by maneuvering around on it, RMS loads, loads during RMS and manual deployment, and loads in the structure due to a known force, such as a push on the structure at a given point with the RMS. A further objective of the structural analysis will be to identify damping, and to validate structural dynamic models with data returned from flight. Without the SSSCR's, only part of this data will be obtainable, since it will have to be stored in raw form, rather than partly conditioned, and will thus take up more room on tape. Under these conditions, for example, only some loads data will be storable, yielding little or no information on structural dynamics and damping in weightlessness.

6.0 BENEFITS FROM SADE

The benefits from performing the structural assembly demonstration experiment include

- An initial demonstration of the capability to both deploy and assemble structures in space from the shuttle
- Statistically meaningful data to allow correlation analysis between neutral buoyancy and zero-g for each category of task and subtask used in the SADE experiment
- A data base for future EVA planning, with experience for timeline construction of future EVA procedures
- Quantitative data on the control laws used by humans in space, and correlations of manipulative times to allow the estimation of the relative significance of mass and moment of inertia on-orbit
- Validation of math models of the human body in weightlessness, and indications of the existence of an instinctive adaptation to the weightless environment
- Human factors evaluation of all structural hardware and supporting equipment, including comparative evaluation of four specific joint designs, and qualitative conclusions as to the more favorable choices and importance of connector design criteria

- Structural loads data on components of the assembled and deployed structure during and after completion, and stresses induced by static and dynamic loading conditions
- Tests of the utility of manual and MMU aided deployment of large structures.
- Verification of the use of the RMS in structural deployment applications.

APPENDIX C: STRUCTURAL DYNAMICS ANALYSIS REPORT

NOMENCLATURE

An underbar denotes a matrix or vector.

A	Cross-sectional area
B	Y dimension of a truss bay
$\underline{C}$	Equivalent stiffness matrix
E	Young's Modulus
$\underline{f}$	Applied force vector
G	Shear modulus
H	Z dimension of a truss bay
$\underline{i}$	Unit vector
i_p	Polar mass moment of inertia per unit length
i_r	Rotary mass moment of inertia per unit length
I	Cross-sectional area moment of inertia
J	Cross-sectional polar area moment of inertia
$\underline{K}$	Finite element stiffness matrix
ℓ	Direction cosine
L	Length of a bar element or length of one bay
m	Mass per unit length
M	Applied moment
$\underline{M}$	Finite element mass matrix
N	Node number
P	Applied axial force
S	Applied shear force
t	Time
T	Applied torque
$\underline{T}$	Transformation matrix
u	Displacement in X direction
$\underline{u}$	Displacement vector
U	Strain energy
v	Displacement in Y direction
w	Displacement in Z direction
W	Work
xyz	Local Cartesian coordinates
XYZ	Global Cartesian coordinates

NOMENCLATURE (cont.)

δ	Denotes first variation
ε	Extensional or shearing strain
ε	Strain vector
θ	Rotation about X
κ	Curvature
Π	Total energy
ϕ	Rotation about Y
ψ	Rotation about Z
ω	Natural Frequency

1. INTRODUCTION

Large space structures are becoming increasingly important to the exploration and development of space. Many of these structures, such as the proposed NASA Space Station, are lattice structures, and will be extremely large and flexible. Others, such as large antennae or the Space Telescope, require a high degree of pointing accuracy in addition to being very flexible, which may necessitate active control to suppress vibrations (reference 1).

Finding the dynamic characteristics of such structures is a challenging problem. Conventional finite element models are extremely large and therefore expensive to implement, which makes them undesirable or impractical, especially in an advanced design stage. Testing large space structures to find their dynamic characteristics is impractical for several reasons. Many will be larger than any existing testing facility, and most will not be able to support their own weight on Earth. Structures such as the Space Station will be built by various contractors which also makes testing impractical (reference 2).

Controlling large space structures is also a very difficult task. The problem is compounded by the occurrence of closely spaced dynamic modes which can cause instabilities if not considered in controlling the structure. In addition, the dynamic model chosen for the structure has a profound effect on the design and performance of the controller (reference 3).

This thesis is a study of the dynamics of the Structural Assembly Demonstration Experiment (SADE) truss. SADE is a proposed Space Shuttle experiment designed to test the assembly and deployment of structures in space. The SADE truss consists of seven cubical bays arranged linearly to form a beam-like structure extending from the Shuttle bay, with a tip mass at the free end. The truss resembles a shorter version of the long central mast in the current proposed Space Station design.

The purpose of this thesis is to evaluate several methods for finding the dynamic characteristics of the SADE truss and to determine the effects of individual bar vibrations on the dynamic modes of a beam-like truss. Several finite element models are set up first, to find the modes of the SADE truss. These results are considered to be a reliable basis for comparison with subsequent results. Next, several methods are employed to determine the stiffness properties of the truss. These stiffness properties are then used in continuum models, yielding bending, torsional, and axial frequencies for comparison with finite element results. The stiffness properties are also used to set up a stiffness matrix for one bay of the truss. This super-finite element is employed in constructing a much smaller finite element model of the SADE truss from which the dynamic modes of the truss are found again. To study the effects of bar vibrations on the modes of a beam-like truss, and to estimate the global modes of the SADE truss, a two-dimensional version of the SADE truss is considered. This planar truss is analyzed with two standard finite element models and with a refined finite element model with additional nodes at bar midpoints. Finally, a two-dimensional truss with no lumped masses is considered to more generally assess the effects of individual bar vibrations on the global modes of a truss. This truss is analyzed with two standard finite element models, a refined finite element model with additional nodes at bar midpoints, and a finite element model with exact dynamic stiffness coefficients.

2. FINITE ELEMENT METHODS

2.1 DESCRIPTION OF SADE TRUSS

The SADE truss consists of seven cubical bays arranged in a row to form a beam-like structure three-hundred and eighty-five inches long (see figure 1). The four nodes at the restrained end of the truss are pinned, so the structure resembles a cantilevered beam, although rotational degrees of freedom are allowed at these four restrained nodes. The arrangement of the bar elements can be seen in Figure 1 and is specified in Table 1.

The bar elements are made from 6061 aluminum. Each bar has a circular cross section with an outer diameter of 2.0 inches and a thickness of 0.072 inches. The length of the shorter bars is 55.0 inches (the length of one bay) while the length of the longer diagonal members is $55.0\sqrt{2}$ inches.

The mass of the truss is 442.00 lb_m. The mass of the bars is 259.65 lb_m. The shorter bars have a mass of 2.3411 lb_m while the mass of the longer bars is 3.3109 lb_m. The remaining 182.35 lb_m is allocated to the joints. The amount of joint mass placed at a specific node is proportional to the number of bar elements which are joined at that node (see Table 2). Thus, node 10 has twice as much joint mass as node 2 since eight bars are joined at node 10 as opposed to four bars at node 2. In addition, there is a tip mass of 220.46 lb_m at the free end of the truss. This tip mass is equally divided between the four nodes at the free end (nodes 29, 30, 31, and 32).

2.2 PIN-JOINTED MODEL

The first model of the SADE truss considered was a pin-jointed finite element model with a consistent mass matrix. This model allows three degrees of freedom at each node. The three degrees of freedom are the translational

FIGURE 1

The SADE Truss

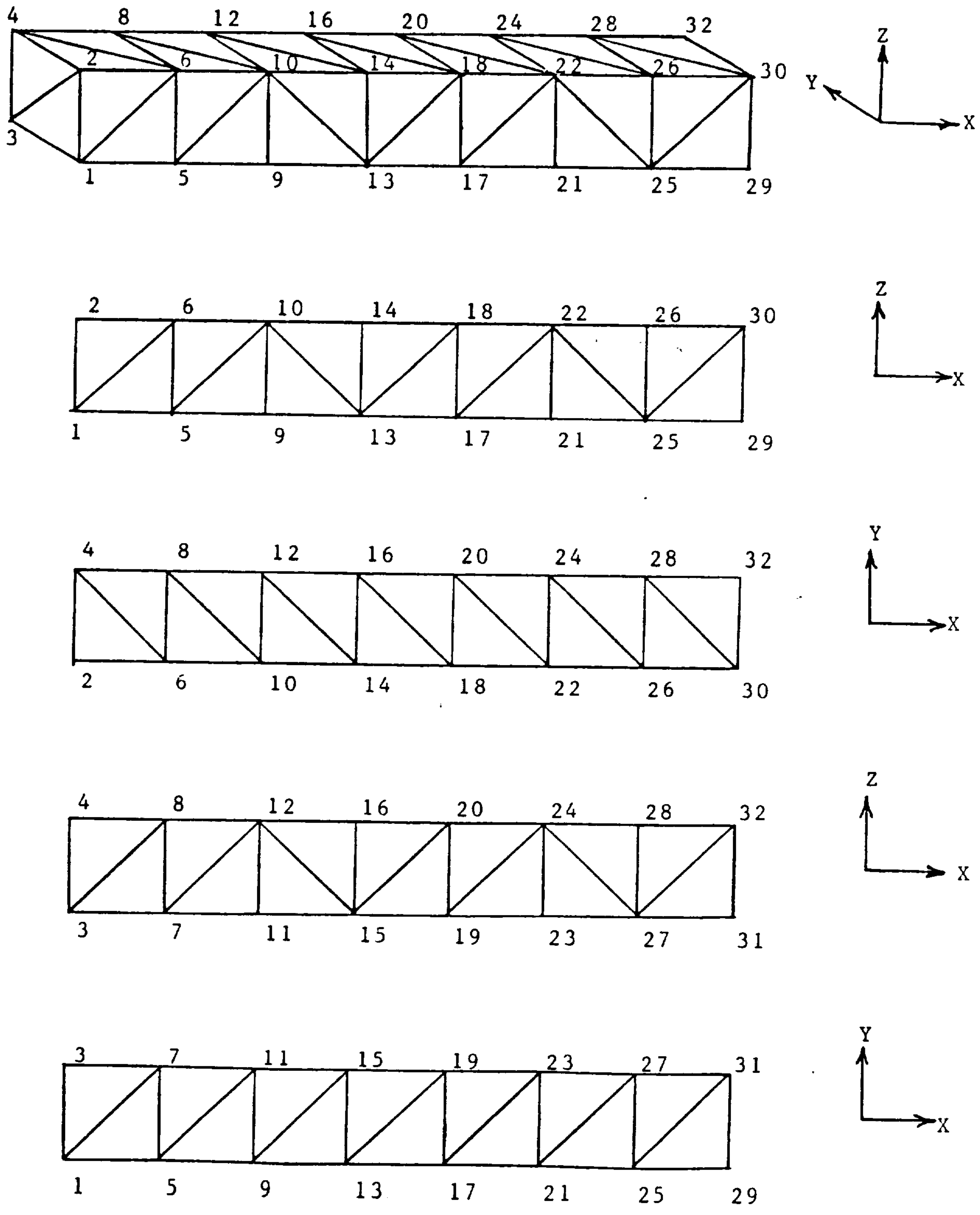

TABLE 1

SADE Bar Connectivities (From node i to node j)

1 - 2
1 - 3
1 - 5
1 - 6
1 - 7
2 - 3
2 - 4
2 - 6
3 - 4
3 - 7
3 - 8
4 - 6
4 - 8
5 - 6
5 - 7
5 - 9
5 - 10
5 - 11
6 - 7
6 - 8
6 - 10
7 - 8
7 - 11
7 - 12
8 - 10
8 - 12
9 - 10
9 - 11
9 - 13
9 - 15
10 - 11
10 - 12
10 - 13
10 - 14
11 - 12
11 - 15
12 - 14
12 - 15
12 - 16
13 - 14
13 - 15
13 - 17
13 - 18
13 - 19
14 - 15
14 - 16
14 - 18
15 - 16
15 - 19
15 - 20
16 - 18
16 - 20
17 - 18
17 - 19
17 - 21
17 - 22
17 - 23
18 - 19
18 - 20
18 - 22
19 - 20
19 - 23
19 - 24
20 - 22
20 - 24
21 - 22
21 - 23
21 - 25
21 - 27
22 - 23
22 - 24
22 - 25
22 - 26
23 - 24
23 - 27
24 - 26
24 - 27
24 - 28
25 - 26
25 - 27
25 - 29
25 - 30
25 - 31
26 - 27
26 - 28
26 - 30
27 - 28
27 - 31
27 - 32
28 - 30
28 - 32
29 - 30
29 - 31
30 - 31
30 - 32
31 - 32

TABLE 2

SADE Joint Masses

Node	Joint Mass ($lb\text{-}sec^2/in$)	Node	Joint Mass ($lb\text{-}sec^2/in$)
1	1.2290×10^{-2}	17	1.4747×10^{-2}
2	9.832×10^{-3}	18	1.7205×10^{-2}
3	1.2290×10^{-2}	19	1.7205×10^{-2}
4	9.832×10^{-3}	20	1.4747×10^{-2}
5	1.4747×10^{-2}	21	1.2290×10^{-2}
6	1.7205×10^{-2}	22	1.9663×10^{-2}
7	1.7205×10^{-2}	23	1.4747×10^{-2}
8	1.4747×10^{-2}	24	1.7205×10^{-2}
9	1.2290×10^{-2}	25	1.7205×10^{-2}
10	1.9663×10^{-2}	26	1.4747×10^{-2}
11	1.4747×10^{-2}	27	1.9663×10^{-2}
12	1.7205×10^{-2}	28	1.2290×10^{-2}
13	1.7205×10^{-2}	29	7.374×10^{-3}
14	1.4747×10^{-2}	30	1.4747×10^{-2}
15	1.9663×10^{-2}	31	1.2290×10^{-2}
16	1.2290×10^{-2}	32	9.832×10^{-3}

TABLE 3

SADE Bar Properties

EI (bending stiffness) = 2.0263×10^{6} lb-in^{2}

GJ (torsional stiffness) = 1.5236×10^{6} lb-in^{2}

EA (axial stiffness) = 4.3610×10^{6} lb

m (mass per unit length) = 1.1016×10^{-4} lb-sec^{2}/in

I_p/A (polar area moment of inertia divided by cross sectional area) = 9.2930×10^{-1} in^{2}

Diagonal bar length is $55\sqrt{2}$ in. Shorter bar length is 55 in.

displacements in the X, Y, and Z coordinate directions. Therefore, this model does not take into account the bending or torsional stiffness of the bar elements.

Since the truss contains thirty-two nodes, there are ninety-six unrestrained degrees of freedom in the model. Thus, the unrestrained displacement vector $\underline{u}$ is 96x1 while the unrestrained stiffness and mass matrices are each 96x96. The X displacement at node N is degree of freedom 3N-2, while the Y displacement is degree of freedom 3N-1 and the Z displacement is degree of freedom 3N.

A typical bar element is shown in Figure 2. The local coordinates are lowercase and the global coordinates are uppercase. The degrees of freedom in local coordinates of the bar are numbered. The element stiffness matrix for a bar in local coordinates is

$$\underline{K}_{xyz} = EA/L \begin{bmatrix} 1 & 0 & 0 & -1 & 0 & 0 \\ 0 & 0 & 0 & 0 & 0 & 0 \\ 0 & 0 & 0 & 0 & 0 & 0 \\ -1 & 0 & 0 & 1 & 0 & 0 \\ 0 & 0 & 0 & 0 & 0 & 0 \\ 0 & 0 & 0 & 0 & 0 & 0 \end{bmatrix} \qquad (2.1)$$

where E is Young's modulus, A is the cross sectional area of the bar, and L is the length of the bar.

The element stiffness matrix must be transferred to global coordinates. Let $\underline{i}_x$ be a unit vector along the bar from bar node 1 to bar node 2. $\underline{i}_y$ is a unit vector perpendicular to $\underline{i}_x$ and the unit vector $\underline{i}_z$ completes the right handed system for the local bar axes. Now define a 3x3 matrix $\underline{t}$:

$$\underline{t} = \begin{bmatrix} \underline{i}_X\cdot\underline{i}_x & \underline{i}_X\cdot\underline{i}_y & \underline{i}_X\cdot\underline{i}_z \\ \underline{i}_Y\cdot\underline{i}_x & \underline{i}_Y\cdot\underline{i}_y & \underline{i}_Y\cdot\underline{i}_z \\ \underline{i}_Z\cdot\underline{i}_x & \underline{i}_Z\cdot\underline{i}_y & \underline{i}_Z\cdot\underline{i}_z \end{bmatrix} \tag{2.2}$$

where $\underline{i}_X$, $\underline{i}_Y$, and $\underline{i}_Z$ are unit vectors in the global coordinate system along the coordinate axes. To find the elements of the direction cosine matrix $\underline{t}$ above, let

$$\underline{i}_x = \alpha\underline{i}_X + \beta\underline{i}_Y + \gamma\underline{i}_Z \tag{2.3}$$

where

$$\alpha=(X_2-X_1)/L \qquad \beta=(Y_2-Y_1)/L \qquad \gamma=(Z_2-Z_1)/L$$

$$L = \quad (X_2-X_1)^2 + (Y_2-Y_1)^2 + (Z_2-Z_1)^2$$

(X_2,Y_2,Z_2) is the global coordinate of bar node 2 while (X_1,Y_1,Z_1) is the global coordinate of bar node 1.
Also, let

$$\underline{i}_y = a\underline{i}_X + b\underline{i}_Y \tag{2.4}$$

Here, $\underline{i}_y$ needs no Z component since it is perpendicular to $\underline{i}_x$, and is assumed to lie in the X-Y plane. Since $\underline{i}_y$ is a unit vector,

$$\sqrt{a^2 + b^2} = 1 \tag{2.5}$$

or

$$b^2 = 1 - a^2 \tag{2.6}$$

Since $\underline{i}_y$ is perpendicular to $\underline{i}_x$,

$$\underline{i}_y\cdot\underline{i}_x = 0 \tag{2.7}$$

Therefore,

$$a\alpha + b\beta = 0 \tag{2.8}$$

which gives

$$a^2 = \frac{\beta^2}{\alpha^2 + \beta^2} \tag{2.9}$$

or

$$a = -\sqrt{\frac{(Y_2-Y_1)^2}{(X_2-X_1)^2+(Y_2-Y_1)^2}} \tag{2.10}$$

The negative sign is chosen as the convention here. From (2.8) we have

(2.11)

or

$$b = \frac{X_2-X_1}{Y_2-Y_1}\sqrt{\frac{(X_2-X_1)^2}{(Y_2-Y_1)^2+(X_2-X_1)^2}} \tag{2.12}$$

However, if $\beta=0$ then $a=0$ and we set $b=1$, which satisfies both the condition that $\underline{i}_y$ has unit magnitude and that $\underline{i}_y$ is perpendicular to $\underline{i}_x$. We have now defined $\underline{i}_x$ and $\underline{i}_y$ in terms of the global coordinates. For $\underline{i}_z$ we take the vector cross product of $\underline{i}_x$ and $\underline{i}_y$:

$$\underline{i}_z = \underline{i}_x \times \underline{i}_y \tag{2.13}$$

$$= -b\gamma\underline{i}_X + a\gamma\underline{i}_Y + (b\alpha-a\beta)\underline{i}_Z$$

Since we have defined $\underline{i}_x$, $\underline{i}_y$, and $\underline{i}_z$ in terms of the global coordinates we can rewrite (2.2) as

$$\underline{t} = \begin{bmatrix} \alpha & \beta & \gamma \\ a & b & 0 \\ -b\gamma & a\gamma & b\alpha - a\beta \end{bmatrix} \qquad (2.14)$$

where α, β, and γ are defined in (2.3), a is given by (2.10), and b is given by (2.12).

The element stiffness matrix in global coordinates $\underline{K}_{XYZ}$ can now be found from the element stiffness matrix in local coordinates. Let

$$\underset{6x6}{\underline{T}} = \left[\begin{array}{c|c} \underset{3x3}{\underline{t}} & \\ \hline & \underset{3x3}{\underline{t}} \end{array}\right] \qquad (2.15)$$

where the terms in the off-diagonal blocks are all zero (reference 4). Then

$$\underline{K}_{XYZ} = \underline{T}^T \underline{K}_{xyz} \underline{T} \qquad (2.16)$$

The element stiffness matrices in global coordinates are assembled to form the unrestrained structure stiffness matrix $\underline{K}$ by adding their stiffnesses to the proper elements of $\underline{K}$. This is done by considering the appropriate degrees of freedom.

The unrestrained structure consistent mass matrix $\underline{M}_C$ is formed in a similar manner. The element mass matrix in local coordinates is

$$\underline{M}_{xyz} = mL \begin{bmatrix} 1/3 & 0 & 0 & 1/6 & 0 & 0 \\ 0 & 1/3 & 0 & 0 & 1/6 & 0 \\ 0 & 0 & 1/3 & 0 & 0 & 1/6 \\ 1/6 & 0 & 0 & 1/3 & 0 & 0 \\ 0 & 1/6 & 0 & 0 & 1/3 & 0 \\ 0 & 0 & 1/6 & 0 & 0 & 1/3 \end{bmatrix} \qquad (2.17)$$

where m is the mass per unit length of the bar, and allowance is made for bar rotations as well as bar stretching. This element mass matrix is converted to global coordinates with the same transformation used for the element stiffness matrix:

$$\underline{M}_{XYZ} = \underline{T}^T \underline{M}_{xyz} \underline{T} \qquad (2.18)$$

The element mass matrices in global coordinates are then assembled to form the unrestrained structure consistent mass matrix $\underline{M}_C$.

To get the unrestrained structure mass matrix $\underline{M}$, the joint masses (and tip masses) at the nodes must be added to $\underline{M}_C$. The joint masses are modeled as point masses. Therefore, the point mass at node N is added to elements (3N-2,3N-2), (3N-1,3N-1), and (3N,3N) of $\underline{M}_C$, corresponding to the three translational degrees of freedom at that node.

The structure is restrained in degrees of freedom 1 through 12. Therefore, the rows and columns of $\underline{K}$ and $\underline{M}$ corresponding to these degrees of freedom are removed to form the restrained structure stiffness matrix $\underline{K}$ and the restrained structure mass matrix $\underline{M}$. Also, the first twelve entries of the unrestrained displacement vector $\underline{u}$ are removed (and set equal to zero) to form the restrained displacement vector $\underline{u}$.

The equation of motion of the truss is

$$\underline{M}\ddot{\underline{u}} + \underline{K}\underline{u} = \underline{0} \qquad (2.19)$$

Assuming $\underline{u}=\underline{U}\cos(\omega t+\phi)$, where ϕ is a phase angle, we obtain

$$(\underline{K}-\omega^2\underline{M})\ \underline{U} = \underline{0} \tag{2.20}$$

The characteristic equation

$$\det\ (\underline{K}-\omega^2\underline{M}) = 0 \tag{2.21}$$

is solved using the method of subspace iteration to obtain the desired number of lowest eigenvalues (squared natural frequencies) ω_r^2. These are used in (2.20) to find the associated eigenvectors $\underline{U}$, which specify the mode shapes.

The computer program that assembles the restrained structure stiffness and mass matrices (which is designed to work for a general space truss) is presented in Appendix D. The natural frequencies and mode shapes were found by using the output from this program in the Finite Element Analysis Basic Library of the Aeroelastic and Structures Research Laboratory at MIT. The eigenvectors for the first twelve modes are presented in Appendix C. The natural frequencies for the first sixteen modes and mode shape descriptions for the first twelve modes are presented in Table 4. The modes are well spaced except that the bending modes occur in closely spaced pairs. Also, if the truss is considered as a beam, the neutral axis in bending passes through diagonally opposite nodes. Another way of stating this is that the direction of bending motion is at a forty-five degree angle to the X and Y axes (see Figure 3).

This analysis was also performed using a lumped mass matrix formed by concentrating one-half of the mass of each bar element at each of the nodes at its ends. This method yielded results which were very close to those obtained with the consistent mass matrix (with concentrated joint masses), especially in the lower modes.

FIGURE 2

Pin-Jointed Bar Element

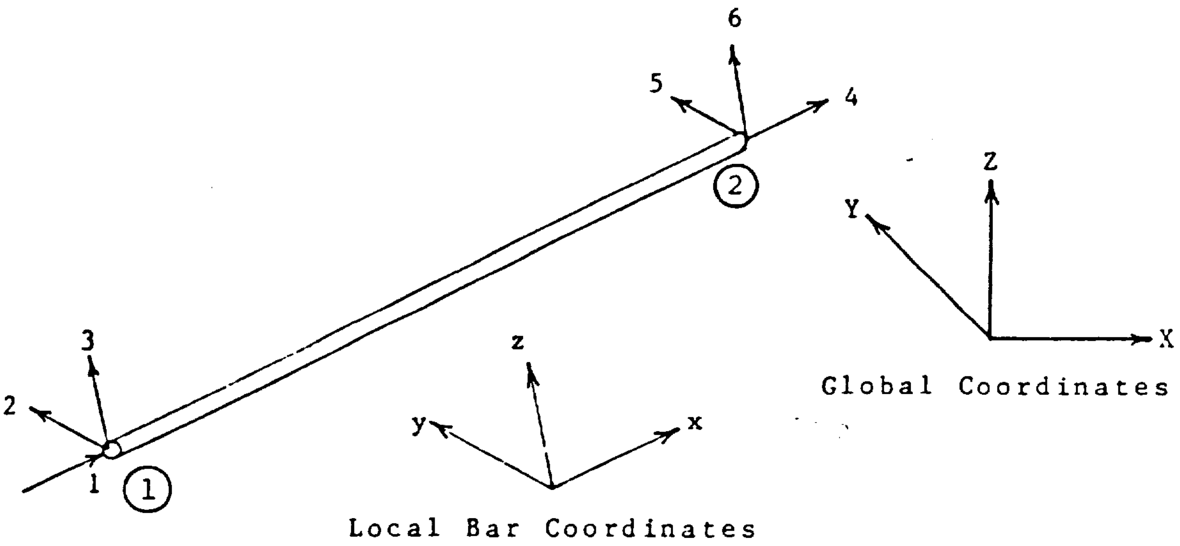

y axis is chosen to lie in a plane parallel to X-Y plane

FIGURE 3

First Bending Mode Pair of SADE Truss

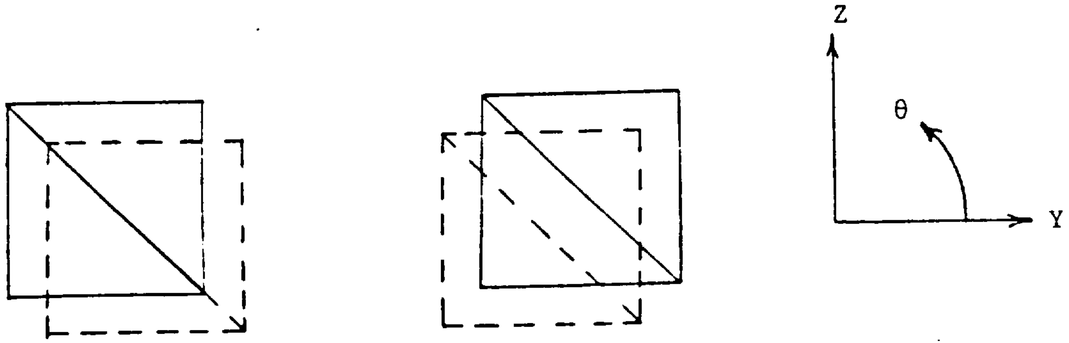

First Mode of First Bending Mode Pair

Second Mode of First Bending Mode Pair

2.3 RIGID-JOINTED MODEL

The rigid-jointed model of the SADE truss allows six degrees of freedom at each node. Three of these are the translations in the coordinate directions. The other three degrees of freedom are the rotations about axes in the coordinate directions. Therefore, this model takes into account the bending and torsional stiffness of the bar elements.

There are now one-hundred and ninety-two degrees of freedom in the model since the truss contains thirty-two nodes. The X, Y, and Z displacements at node N are degrees of freedom 6N-5, 6N-4, and 6N-3, respectively. The rotations about axes in the X, Y, and Z directions are denoted by θ, ϕ, and ψ, and the degrees of freedom associated with these rotations at node N are 6N-2, 6N-1, and 6N, respectively.

A typical element is shown in Figure 4. The 12x12 element stiffness and consistent mass matrices (in local coordinates) are given by Craig (reference 5, pp. 391,392):

$$\underline{K}_{xyz} = \left[\begin{array}{c|c} \underline{k}_a & \underline{k}_b \\ \hline \underline{k}_c & \underline{k}_d \end{array}\right] \qquad (2.22)$$

where

$$\underline{k}_a = \begin{bmatrix} EA/L & & & & & \\ & 12EI_z/L^3 & & & & 6EI_z/L^2 \\ & & 12EI_y/L^3 & & -6EI_y/L^2 & \\ & & & GJ/L & & \\ & & -6EI_y/L^2 & & 4EI_y/L & \\ & 6EI_z/L^2 & & & & 4EI_z/L \end{bmatrix}$$

$$\underline{k}_b = \begin{bmatrix} -EA/L & & & & & \\ & -12EI_z/L^3 & & & & 6EI_z/L^2 \\ & & -12EI_y/L^3 & & -6EI_y/L^2 & \\ & & & -GJ/L & & \\ & & 6EI_y/L^2 & & 2EI_y/L & \\ & -6EI_z/L^2 & & & & 2EI_z/L \end{bmatrix}$$

$$\underline{k}_d = \begin{bmatrix} EA/L & & & & & \\ & 12EI_z/L^3 & & & & -6EI_z/L^2 \\ & & 12EI_y/L^3 & & 6EI_y/L^2 & \\ & & & GJ/L & & \\ & & 6EI_y/L^2 & & 4EI_y/L & \\ & -6EI_z/L^2 & & & & 4EI_z/L \end{bmatrix}$$

$$\underline{k}_c = \underline{k}_b^T$$

and I_y and I_z are the area moments of inertia of the bar cross section about the y and z axes, G is the shear stiffness, and J is the polar area moment of inertia of the bar cross section; also,

$$\underline{M}_{xyz} = mL/420 \left[\begin{array}{c|c} \underline{m}_a & \underline{m}_b \\ \hline \underline{m}_c & \underline{m}_d \end{array}\right] \qquad (2.23)$$

where

$$\underline{m}_a = \begin{bmatrix} 140 & & & & & \\ & 156 & & & & 22L \\ & & 156 & & -22L & \\ & & & 140 I_p/A & & \\ & & -22L & & 4L^2 & \\ & 22L & & & & 4L^2 \end{bmatrix}$$

$$\underline{m}_b = \begin{bmatrix} 70 & & & & & \\ & 54 & & & & -13L \\ & & 54 & & 13L & \\ & & & 70 I_p/A & & \\ & & -13L & & -3L^2 & \\ & 13L & & & & -3L^2 \end{bmatrix}$$

$$\underline{m}_d = \begin{bmatrix} 140 & & & & & \\ & 156 & & & & -22L \\ & & 156 & & 22L & \\ & & & 140 I_p/A & & \\ & & 22L & & 4L^2 & \\ & -22L & & & & 4L^2 \end{bmatrix}$$

$$\underline{m}_c = \underline{m}_b{}^T$$

where I_p is the polar mass moment of inertia of the bar cross section. The element matrices are again transformed according to (2.16) and (2.18), except now

$$\underset{12\times12}{\underline{T}} = \begin{bmatrix} \underset{3\times3}{\underline{t}} & & & \\ & \underset{3\times3}{\underline{t}} & & \\ & & \underset{3\times3}{\underline{t}} & \\ & & & \underset{3\times3}{\underline{t}} \end{bmatrix} \qquad (2.24)$$

The joint mass at a node is added to the diagonal elements of the unrestrained structure consistent mass matrix which correspond to the translational degrees of freedom at that node. Thus, the joint mass at node N is added to elements (6N-5,6N-5), (6N-4,6N-4), and (6N-3,6N-3) of $\underline{M}_C$. Since the joint masses are assumed to be point masses they have zero moment of inertia, and consequently no lumped quantities are added to the diagonal elements of $\underline{M}_C$ which correspond to rotational degrees of freedom.

It is assumed that the four nodes at the base of the truss are pinned and not clamped. Therefore, degrees of freedom 1, 2, 3, 7, 8, 9, 13, 14, 15, 19, 20, and 21 are now restrained. The rows and columns of the unrestrained structure stiffness and mass matrices and the rows of the unrestrained displacement vector corresponding to these degrees of freedom are removed to form the restrained system. The resulting equation of motion is then solved using the same techniques as in the pin-jointed analysis to obtain natural frequencies and mode shapes.

The natural frequencies for the lowest sixteen modes again are presented in Table 4 and the eigenvectors are given in Appendix C. The frequency results correlate very well with those from the pin-jointed analysis in the lower modes.

As the mode number increases, the frequencies obtained using the rigid-jointed model become somewhat lower than those from the pin-jointed model. This is probably due to the influence of local bar element natural frequencies on the global structural modes. Note, however, that the last several modes of the rigid-jointed model are now very closely spaced. This phenomenon is associated with the vibrations relative to the joints of the individual bar elements and will be addressed in Chapters 6 and 7.

FIGURE 4

Rigid-Jointed Bar Element

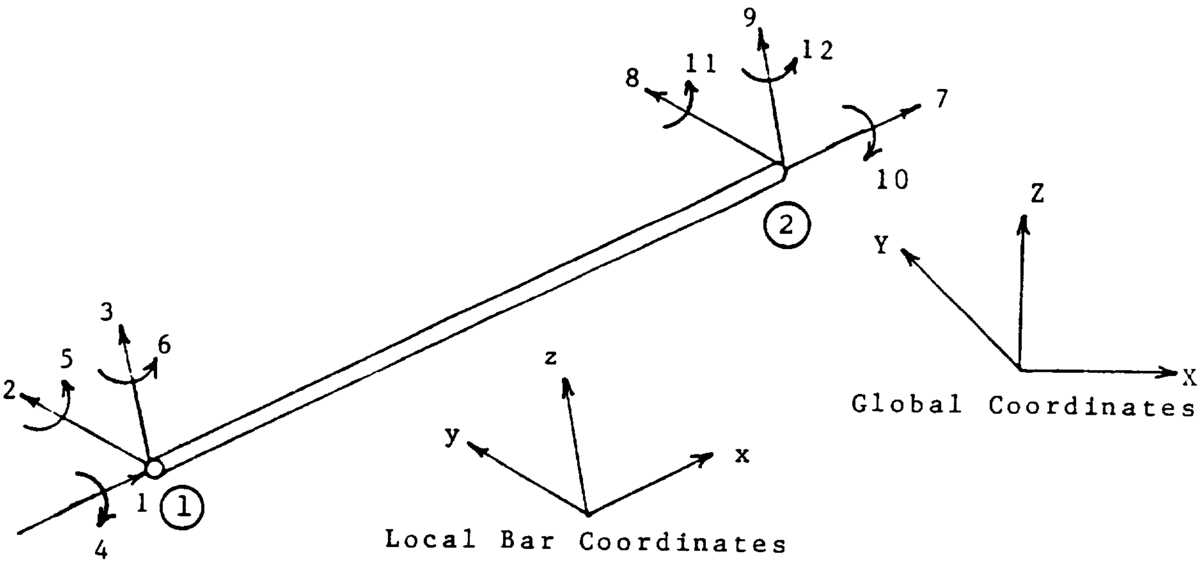

y axis is chosen to lie in a plane parallel to X-Y plane

3. CONTINUUM METHODS

3.1 GENERATION OF STIFFNESS PROPERTIES

If a beam-like truss is considered to be a beam in bending then a continuum equation of motion from beam theory can be used to find the natural frequencies for the bending modes of the truss. Similarly, continuum models for a torsional rod and an axial bar can be used to find the natural frequencies of the truss in its torsional and axial modes. However, to use these continuum models we must first define continuum stiffness and inertia properties for the truss. For bending, we need to define the bending stiffness EI and the shear stiffness GA if Timoshenko beam theory is used. The inertia properties needed are an equivalent mass per unit length m and an eqivalent rotary mass moment of inertia per unit length i_r. For torsion, a torsional stiffness GJ must be defined as well as a mass per unit length and a polar mass moment of inertia per unit length i_p. For axial vibrations, we need an axial stiffness EA as well as m.

Defining the equivalent inertia properties of the SADE truss is relatively straightforward. The analyses used to define m, i_r, and i_p are presented in sections 3.2 through 3.5 as these quantities are needed. However, methods for finding the continuum stifness properties are not as obvious. Two methods are presented in this section. The first finds the stiffness properties by performing a static pin-jointed finite element analysis of one bay of the truss. The second considers the energy of the bar elements in one bay and is based on the work of Noor, Anderson, and Greene (reference 6).

A. Static Pin-Jointed Truss Analysis for One Bay

Consider the bay at the base of the SADE truss. This bay extends from X=0 inches to X=55 inches (see Figure 1). It is bounded by nodes 1, 2, 3, and 4 at the fixed (X=0) end and by nodes 5, 6, 7, and 8 at the free (X=55 inches) end. To analyze the stiffness properties of the bay we restrain it at the fixed end by pinning nodes 1 through 4.

The restrained stiffness matrix $\underline{K}$ for the bay is found using the pin-jointed finite element procedure described in section 2.2. This matrix is 12x12 since there are four free nodes with three translational degrees of freedom at each node. Thus, degrees of freedom 1, 4, 7, and 10 are the X displacements at nodes 5, 6, 7, and 8, respectively. Degrees of freedom 2, 5, 8, and 11 are the Y displacements and degrees of freedom 3, 6, 9, and 12 are the Z displacements at these nodes.

Appropriate forces can be applied at the free end of the bay by way of a 12x1 force vector $\underline{f}$. We can find the corresponding 12x1 displacement vector $\underline{u}$ according to

$$\underline{Ku} = \underline{f} \quad \text{or} \quad \underline{u} = \underline{K}^{-1}\underline{f} \qquad (3.1)$$

Once $\underline{u}$ is determined, beam theory equations can be used to find the continuum stiffness properties of the bay.

For example, consider placing a pure moment M_Y (in the Y direction using the right hand rule) on the free end of the bay. This can be accomplished by letting

$$\underline{f}^T = [-100\ 0\ 0\ 100\ 0\ 0\ -100\ 0\ 0\ 100\ 0\ 0]\ \text{lb} \qquad (3.2)$$

The magnitude of the moment is chosen with regard to purely numerical considerations; any value would do in theory. The above value of $\underline{f}$ gives M_Y=11000 in-lb. We can find the corresponding displacement vector from (3.1):

$$\underline{u} = \begin{bmatrix} -1.26117\text{E}-03 \\ 1.26117\text{E}-03 \\ -1.26119\text{E}-03 \\ 1.26118\text{E}-03 \\ 1.26119\text{E}-03 \\ -1.26119\text{E}-03 \\ -1.26117\text{E}-03 \\ 1.26117\text{E}-03 \\ -1.26121\text{E}-03 \\ 1.26118\text{E}-03 \\ 1.26119\text{E}-03 \\ -1.26121\text{E}-03 \end{bmatrix} \text{in} \qquad (3.3)$$

From beam theory we have

$$M_Y = EI_Y\kappa_Y - EI_{YZ}\kappa_Z \qquad (3.4)$$

$$M_Z = -EI_{YZ}\kappa_Y - EI_Z\kappa_Z \qquad (3.5)$$

where M_Z (which is zero for now) is the moment on the free end of the bay in the Z direction, EI_Y (EI_Z) is the bending stiffness about the Y (Z) axis, EI_{YZ} is a coupling term, and κ_Y (κ_Z) is the curvature about the Y (Z) axis. κ_Y and κ_Z are approximated by

$$\kappa_Y = \frac{u_{X_6} + u_{X_8}}{2HL} - \frac{u_{X_5} + u_{X_7}}{2HL} \qquad (3.6)$$

$$\kappa_Z = \frac{u_{X_6} + u_{X_5}}{2BL} - \frac{u_{X_8} + u_{X_7}}{2BL} \qquad (3.7)$$

where u_{XN} is the X displacement at node N, L is the X dimension of the bay, H is the Z dimension of the bay, and B is the Y dimension of the bay (L=H=B in this case). We now have κ_Y, κ_Z, and M_Y with M_Z=0. Similarly, we can determine κ_Y and κ_Z with M_Z=11000 in-lb and M_Y=0 by letting

$$\underline{f}^T = [100\ 0\ 0\ 100\ 0\ 0\ -100\ 0\ 0\ -100\ 0\ 0]\ \text{lb} \qquad (3.8)$$

which yields

$$\underline{u} = \begin{bmatrix} 1.26117E-03 \\ 1.71793E-03 \\ -6.85117E-04 \\ 1.02256E-03 \\ 6.85117E-04 \\ -6.85117E-04 \\ -1.38048E-03 \\ 1.71793E-03 \\ 6.85145E-04 \\ -1.14187E-03 \\ 6.85117E-04 \\ 8.04447E-04 \end{bmatrix} \text{in} \qquad (3.9)$$

The system defined by (3.4) and (3.5) can be solved two separate times, the first time with M_Y=11000 in-lb and M_Z=0, using the corresponding values of κ_Y and κ_Z, and the second time with M_Z=11000 in-lb and M_Y=0 using the new values of κ_Y and κ_Z. Doing this yields $EI_Y=1.3192\times10^{10}$ lb-in^2, $EI_Z=1.3847\times10^{10}$ lb-in^2, and $EI_{YZ}=0$.

For the shear stiffness the equations to be solved are

$$-\frac{\psi}{2} + \frac{dv}{dX} = \frac{1}{GA_Y} S_Y + \frac{1}{GA_{YZ}} S_Z \qquad (3.10)$$

$$\frac{\phi}{2} + \frac{dw}{dX} = \frac{1}{GA_{YZ}} S_Y + \frac{1}{GA_Z} S_Z \qquad (3.11)$$

where ψ and ϕ are rotations about Z and Y, respectively, at X=L, and the terms on the left side of the equations are shear strains. Also, GA_Y (GA_Z) is the shear stiffness in the Y (Z) direction, $1/GA_{YZ}$ is the coupling term, S_Y (S_Z) is the shear force in the Y (Z) direction and v (w) is the deflection along the length of the bay in the Y (Z) direction. dv/dX, dw/dX, ϕ, and ψ are approximated by

$$\frac{dv}{dX} = \frac{u_{Y_5} + u_{Y_6} + u_{Y_7} + u_{Y_8}}{4L} \qquad (3.12)$$

$$\frac{dw}{dX} = \frac{u_{Z_5} + u_{Z_6} + u_{Z_7} + u_{Z_8}}{4L} \qquad (3.13)$$

$$\phi = \frac{u_{X_6} + u_{X_8}}{2L} - \frac{u_{X_5} + u_{X_7}}{2L} \qquad (3.14)$$

$$\psi = \frac{u_{X_6} + u_{X_5}}{2L} - \frac{u_{X_8} + u_{X_7}}{2L} \qquad (3.15)$$

The analysis procedure is the same as for the bending stiffness. We solve the system defined by (3.10) and (3.11) twice, once with S_Y=200 lb and S_Z=0, and next with S_Z=200 lb and S_Y=0. For S_Y=200 lb we set

$$\underline{f}^T = [0\ 50\ 0\ 0\ 50\ 0\ 0\ 50\ 0\ 0\ 50\ 0]\ \text{lb} \qquad (3.16)$$

with which we can use (3.1) to find

$$\underline{u} = \begin{bmatrix} 0.00000E+00 \\ 5.68727E-03 \\ -9.73155E-04 \\ 1.14187E-03 \\ 4.54028E-03 \\ -9.73155E-04 \\ -1.32083E-03 \\ 5.05668E-03 \\ -2.88033E-04 \\ 5.96540E-05 \\ 5.17087E-03 \\ -2.28380E-04 \end{bmatrix} \text{in} \qquad (3.17)$$

For S_Z=200 lb,

$$\underline{f}^T = [0\ 0\ 50\ 0\ 0\ 50\ 0\ 0\ 50\ 0\ 0\ 50]\ \text{lb} \qquad (3.18)$$

$$\underline{u} = \begin{bmatrix} 0.00000E+00 \\ -1.14155E-04 \\ 5.31492E-03 \\ -1.20154E-03 \\ -1.11721E-03 \\ 4.68434E-03 \\ 2.98183E-05 \\ -1.14155E-04 \\ 5.60306E-03 \\ -1.29104E-03 \\ -1.11721E-03 \\ 4.94263E-03 \end{bmatrix} \text{ in} \qquad (3.19)$$

Using these results for $\underline{u}$ in (3.10) and (3.11) we find that $GA_Y=2.1511\times10^6$ lb, $GA_Z=2.1417\times10^6$ lb, and $GA_{YZ}=-1.7866\times10^7$ lb.

We have now determined the stiffnesses needed for a continuum dynamic model of the beam-like truss in bending. However, such a model requires that the neutral axis for bending is defined. The finite element results of Chapter 2 showed that the neutral axes for the bending mode pairs are at a forty-five degree angle to the coordinate Y and Z directions. Bending about these neutral axes is assumed in the continuum model. A Mohr's circle transformation on the shear stiffnesses shows that the principal axes for shear are also at forty-five degree angles to the Y and Z axes, which is where the coupling term $1/GA_{YZ}$ equals zero. The first principal axis is at $\theta=135^\circ$, where θ is the angle about the X axis as measured from the Y axis (see Figure 3). The shear stiffness associated with this direction is $GA_1=1.9161\times10^6$ lb. The other principal axis for shear is at $\theta=45^\circ$ and the shear stiffness associated with this direction is $GA_2=2.4394\times10^6$ lb. The principal axes for the bending stiffnesses are the Y and Z axes since $EI_{YZ}=0$. If we denote EI_1 as the bending stiffness at $\theta=135^\circ$ and EI_2 as the bending stiffness at $\theta=45^\circ$, we find that $EI_1=EI_2=EI=1.3520\times10^{10}$ lb-in^2. Thus, the change in the bending stiffness is less than three percent as the axes are rotated. This is due to the fact that most of the bending stiffness is provided by the longitudinal (X-X) bars. If we take a cross section of the truss and calculate the bending stiffness considering only the longitudinal bars, we find that $EI_Y = EI_Z = EI_1 = EI_2 = 1.3192\text{x}10^{10}$ lb-in^2.

The torsional stiffness GJ is found by using the equation

$$\theta = \frac{TL}{GJ} \tag{3.20}$$

where θ is the angle of twist of the bay about the X axis. A torque T of $-1.1(10^6)$ in-lb produces an angle which is numerically reasonable for computational considerations. This torque can be produced by setting

$$\underline{f}^T = [0\ -5\ 5\ 0\ 5\ 5\ 0\ -5\ -5\ 0\ 5\ -5]\ \text{x}10^3 \text{ lb} \tag{3.21}$$

which yields

$$\underline{u} = \begin{bmatrix} 0.00000E+00 \\ -5.57312E-01 \\ 4.05366E-01 \\ 5.96678E-03 \\ 3.71118E-01 \\ 3.42308E-01 \\ 1.29101E-01 \\ -4.94253E-01 \\ -5.31502E-01 \\ 1.23138E-01 \\ 4.34177E-01 \\ -4.71425E-01 \end{bmatrix} \text{ in} \tag{3.22}$$

θ can be found by considering the Y and Z components of $\underline{u}$ and ignoring the X components. We can then define θ to be the average of the angles of rotation in the Y-Z plane of each of the four nodes at the free end of the bay. The angle of rotation of a node can be determined with vector analysis. We know the components of the vector which extends from the center of the bay cross section (in the Y-Z plane at X=L) to the undisplaced node. Since the Y and Z components of $\underline{u}$ have been found, we also know the components of the vector which extends from the bay center to the displaced node. The angle between these two vectors is the angle of rotation of the node and can be found by taking the dot product of the vectors. Once this is done for all four nodes, θ is determined and from (3.20) we find $GJ=3.6923\times10^9$ lb-in^2.

For EA we use the equation

$$u = \frac{PL}{EA} \qquad (3.23)$$

where P=400 lb is a force in the X direction. P is applied to the bay by setting

$$\underline{f}^T = [100\ 0\ 0\ 100\ 0\ 0\ 100\ 0\ 0\ 100\ 0\ 0]\ \text{lb} \qquad (3.24)$$

which yields

$$\underline{u} = \begin{bmatrix} 1.26117E-03 \\ -8.04441E-04 \\ -6.85137E-04 \\ 1.02257E-03 \\ 6.85136E-04 \\ -6.85137E-04 \\ 1.14187E-03 \\ -8.04441E-04 \\ -1.83728E-03 \\ 1.38049E-03 \\ 6.85137E-04 \\ -1.71797E-03 \end{bmatrix} \text{in} \qquad (3.25)$$

u is simply the average of the four X displacements in $\underline{u}$, so from (3.23) we find $EA=1.831\times10^7$ lb.

B. Energy of Bars Method for One Bay

The method for deriving the continuum stiffness properties of the SADE truss outlined below is based on the work of Noor, Anderson, and Greene (reference 6). First, we must place a new set of coordinate axes (x,y,z) on the bay considered in the previous article. These axes are placed at the stiffness center of the bay at the cross section at X=27.5 inches (the center of the bay). If we let a subscript 0 denote the location of the new coordinate system then $X_0=27.5$ inches and Y_0 and Z_0 will be determined later.

For now, the bay is assumed to be made up of a continuous medium. Let u, v, and w denote the translational displacements of a point on the cross section (in the xyz system) and θ, ϕ, and ψ denote the corresponding rotations about axes in the x, y, and z coordinate directions. Also, let ε_2^0 and ε_3^0 be the extensional strains in the y and z directions at $y=z=0$ and $2\varepsilon_{23}^0$ be the shearing strain in the y-z plane at $y=z=0$. For any point on the cross section we assume

$$\begin{aligned} u &= u^0 - y\psi + z\phi \\ v &= v^0 + y\varepsilon_2^0 + z(-\theta+\tfrac{1}{2}2\varepsilon_{23}^0) \\ w &= w^0 + y(\theta+\tfrac{1}{2}2\varepsilon_{23}^0) + z\varepsilon_3^0 \end{aligned} \tag{3.26}$$

where a superscript 0 denotes $y=z=0$. It is also assumed that u^0, v^0, w^0, θ, ϕ, ψ, ε_2^0, ε_3^0, and $2\varepsilon_{23}^0$ are functions of x only and therefore constant in the cross section.

Using the equations of elasticity, the strain in the cross section can be written as

$$\begin{aligned} \varepsilon_{11} &= \frac{du^0}{dx} - y\frac{d\psi}{dx} + z\frac{d\phi}{dx} \\ &= \varepsilon_1^0 - y\kappa_2^0 + z\kappa_3^0 \end{aligned} \tag{3.27}$$

$$\varepsilon_{22} = \varepsilon_2^0 \tag{3.28}$$

$$\varepsilon_{33} = \varepsilon_3^0 \tag{3.29}$$

$$2\varepsilon_{12} = -\psi + \frac{dv^0}{dx} + y\frac{d\varepsilon_2{}^0}{dx} + z\left(-\frac{d\theta}{dx}+\tfrac{1}{2}\frac{d(2\varepsilon_{23}{}^0)}{dx}\right)$$

$$= 2\varepsilon_{12}{}^0 + y\frac{d\varepsilon_2{}^0}{dx} + z\left(-\kappa_1{}^0+\tfrac{1}{2}\frac{d(\varepsilon_{23}{}^0)}{dx}\right) \qquad (3.30)$$

$$2\varepsilon_{13} = \phi + \frac{dw^0}{dx} + y\left(\frac{d\theta}{dx}+\tfrac{1}{2}\frac{d(2\varepsilon_{23}{}^0)}{dx}\right) + z\frac{d\varepsilon_3{}^0}{dx} \qquad (3.31)$$

$$= 2\varepsilon_{13}{}^0 + y\left(\kappa_1{}^0+\tfrac{1}{2}\frac{d(2\varepsilon_{23}{}^0)}{dx}\right) + z\frac{d\varepsilon_3{}^0}{dx}$$

$$2\varepsilon_{23} = 2\varepsilon_{23}{}^0 \qquad (3.32)$$

where the subscripts 1, 2, and 3 refer to the x, y, and z directions, respectively. If the distortion of the cross section is ignored, (3.30) and (3.31) can be rewritten as

$$2\varepsilon_{12} = 2\varepsilon_{12}{}^0 - z\kappa_1{}^0 \qquad (3.33)$$

$$2\varepsilon_{13} = 2\varepsilon_{13}{}^0 + y\kappa_1{}^0 \qquad (3.34)$$

The extensional strain ε in an arbitrary direction can be written as

$$\varepsilon = \sum_{i=1}^{3}\sum_{j=1}^{3}\varepsilon_{ij}\ell_i\ell_j \qquad (3.35)$$

where ℓ_i is the direction cosine from the arbitrary direction to the i direction and ε_{ij} are the strain components given in (3.27) to (3.34). Now if we assume the cross section does not change shape, we can set $\varepsilon_{22}=0$, $\varepsilon_{33} = 0$, and $2\varepsilon_{23}=0$, and we can write the extensional strain ε in any arbitrarily directed bar as

$$\varepsilon = \underline{a}^T\underline{\varepsilon} \qquad (3.36)$$

where

$$\underline{a}^T = \begin{bmatrix}\ell_1{}^2 & \ell_1\ell_2 & \ell_1\ell_3\end{bmatrix} \qquad (3.37)$$

$$\underline{\varepsilon}^T = \begin{bmatrix} \varepsilon_{11} & 2\varepsilon_{12} & 2\varepsilon_{13} \end{bmatrix} \tag{3.38}$$

Considering (3.27), (3.33), and (3.34), we have

$$\begin{aligned} \underline{\varepsilon} &= \begin{bmatrix} 1 & -y & z & 0 & 0 & 0 \\ 0 & 0 & 0 & 1 & 0 & -z \\ 0 & 0 & 0 & 0 & 1 & y \end{bmatrix} \begin{bmatrix} \varepsilon_1{}^0 \\ \kappa_2{}^0 \\ \kappa_3{}^0 \\ 2\varepsilon_{12}{}^0 \\ 2\varepsilon_{13}{}^0 \\ \kappa_1{}^0 \end{bmatrix} \\ &= \underline{E}_A \underline{\varepsilon}_A \end{aligned} \tag{3.39}$$

The potential energy U of the bay can be expressed by summing the energy of all the included bars as

$$\begin{aligned} U &= \tfrac{1}{2} \sum^{k \text{ bars}} E_k A_k L_k \varepsilon_k{}^2 \\ &= \tfrac{1}{2} \sum^{k} E_k A_k L_k \underline{\varepsilon}_k{}^T \underline{a}_k \underline{a}_k{}^T \underline{\varepsilon}_k \\ &= \tfrac{1}{2} \sum^{k} E_k A_k L_k \underline{\varepsilon}_A{}^T \underline{E}_{A_k}{}^T \underline{a}_k \underline{a}_k{}^T \underline{E}_{A_k} \underline{\varepsilon}_A \end{aligned} \tag{3.40}$$

where the quantities included in the summation are for the kth bar. U can also be expressed as

$$U = \tfrac{1}{2} L \underline{\varepsilon}_A{}^T \underline{C} \underline{\varepsilon}_A \tag{3.41}$$

where an L outside of the summation is the length of the bay and

$$\underline{C} = \begin{bmatrix} EA & & & & & \\ C_{21} & EI_Z & & \text{SYMMETRIC} & & \\ C_{31} & C_{32} & EI_Y & & & \\ C_{41} & C_{42} & C_{43} & GA_Y & & \\ C_{51} & C_{52} & C_{53} & C_{54} & GA_Z & \\ C_{61} & C_{62} & C_{63} & C_{64} & C_{65} & GJ \end{bmatrix} \qquad (3.42)$$

where the off-diagonal elements are coupling terms. Comparing (3.40) and (3.41) yields

$$\underline{C} = \frac{1}{L} \sum^{k} E_k A_k L_k \underline{E}_{A_K}{}^T \underline{a}_k \underline{a}_k{}^T \underline{E}_{A_k} \qquad (3.43)$$

To find Z_0, the Z location of the bay coordinate axes, we choose

$$C_{31} = \sum^{k} E_k A_k L_k z_k \ell_{1_k}{}^4 = 0 \qquad (3.44)$$

where $z_k = Z_k - Z_0$ and the reference point for every bar is its midpoint. This results in

$$Z_0 = \frac{\overset{k}{\Sigma}\; E_k A_k L_k Z_k \ell_{1_k}^{\;4}}{\overset{k}{\Sigma}\; E_k A_k L_k \ell_{1_k}^{\;4}} \tag{3.45}$$

Similarly, for Y_0 we choose $C_{21}=0$, which yields

$$Y_0 = \frac{\overset{k}{\Sigma}\; E_k A_k L_k Y_k \ell_{1_k}^{\;4}}{\overset{k}{\Sigma}\; E_k A_k L_k \ell_{1_k}^{\;4}} \tag{3.46}$$

For the bay of the SADE truss being considered,

$$\underline{C}= \begin{bmatrix} 2.36116E{+}07 & 6.93581E{-}08 & -6.93581E{-}08 & 0.00000E{+}00 & 3.08372E{+}06 & 8.48022E{+}07 \\ 6.93581E{-}08 & 1.55242E{+}10 & 0.00000E{+}00 & 0.00000E{+}00 & 1.08372E{-}08 & -2.33206E{+}09 \\ -6.93581E{-}08 & 0.00000E{+}00 & 1.55242E{+}10 & -8.48022E{+}07 & -1.09556E{-}08 & -7.62939E{-}07 \\ 0.00000E{+}00 & 0.00000E{+}00 & -8.48022E{+}07 & 3.08372E{+}06 & 0.00000E{+}00 & 1.73395E{-}08 \\ 3.08372E{+}06 & 1.08372E{-}08 & -1.09556E{-}08 & 0.00000E{+}00 & 3.08372E{+}06 & -1.73395E{-}08 \\ 8.48022E{+}07 & -2.33206E{+}09 & -7.62939E{-}07 & 1.73395E{-}08 & -1.73395E{-}08 & 4.66412E{+}09 \end{bmatrix} \tag{3.47}$$

where the units are in pounds, inches, and radians. The stiffness terms on the diagonal of the $\underline{C}$ matrix compare favorably with those obtained from the finite element analysis of one bay.

C. Comparison of the Two Methods for Stiffness Property Determination

A direct comparison between the two methods can be made by transforming the results obtained with the finite element anaysis to the form of the $\underline{C}$ matrix. We have already found the 12x12 restrained stiffness matrix for the bay using the methods of Chapter 2. A different restrained stiffness matrix can be derived for the bay if we consider (3.1) where now

$$\underline{f}^T = \begin{bmatrix} P & M_Z & M_Y & S_Y & S_Z & T \end{bmatrix} \qquad (3.48)$$

$$\underline{u}^T = \begin{bmatrix} u & \psi & \phi & v & w & \theta \end{bmatrix} \qquad (3.49)$$

Therefore, $\underline{K}$ is now 6x6. The elements of $\underline{K}^{-1}$ can be found by considering the forces in $\underline{f}$ to be applied one at a time, and determining each of the resulting components of $\underline{u}$. For example, P has been applied to the bay through (3.24). Equation (3.25) gives the corresponding deflections. These can be used to find the elements of the new 6x1 displacement vector $\underline{u}$. For u, v, or w, we simply average the X, Y, or Z deflections at the four free nodes. ϕ and ψ are given by (3.14) and (3.15). θ is found by considering the rotations of the four free nodes as is described in the derivation of GJ in article A.

We have now determined the first column of $\underline{K}^{-1}$:

$$(\underline{K}^{-1})_{i1} = u_i/P \qquad i=1,6 \qquad (3.50)$$

By applying the other five forces one at a time the other five columns of $\underline{K}^{-1}$ can be found:

$$\underline{K}^{-1} = \begin{bmatrix} 3.00381E-06 & -5.42318E-09 & 4.54546E-13 & -1.49130E-07 & -3.07845E-06 & -5.86831E-08 \\ -5.42318E-09 & 3.97197E-09 & 0.00000E+00 & 1.09229E-07 & 2.71300E-09 & 2.03531E-09 \\ 4.54546E-13 & 0.00000E+00 & 4.16917E-09 & 1.14653E-07 & -1.14654E-07 & -3.12397E-14 \\ -1.49130E-07 & 1.09229E-07 & 1.14653E-07 & 2.55689E-05 & -3.07840E-06 & 5.59704E-08 \\ -3.07845E-06 & 2.71300E-09 & -1.14654E-07 & -3.07840E-06 & 2.56812E-05 & 5.80120E-08 \\ -4.03524E-08 & 3.16811E-09 & -3.08491E-10 & 6.38888E-08 & 4.79282E-08 & 1.48957E-08 \end{bmatrix} \qquad (3.51)$$

where the units are in pounds, inches, and radians. The symmetry is very good except for the sixth row and column. We replace the sixth row with the sixth column and round off the other elements where needed to obtain symmetry. The elements of the sixth column are more reliable than those of the sixth row because the terms in the sixth row represent bay rotations about the X axis. The bay does not rotate uniformly, except when a torque is applied. For example, when S_Y is applied node 6 rotates positively but node 8 rotates negatively, and the definition of bay rotation does not make sense.

The symmetric $\underline{K}^{-1}$ can be inverted to obtain

$$\underline{K}=\begin{bmatrix} 4.15378E+05 & -2.16980E+05 & 1.45828E+06 & 6.41260E-02 & 5.30286E+04 & 1.45955E+06 \\ -2.16980E+05 & 3.09879E+08 & 3.99367E+07 & -1.41664E+06 & 3.56055E+04 & -3.80114E+07 \\ 1.45828E+06 & 3.99367E+07 & 3.17855E+08 & -1.41665E+06 & 1.41966E+06 & 8.29681E+04 \\ 6.04642E-02 & -1.41664E+06 & -1.41665E+06 & 5.15143E+04 & -4.89010E-03 & -1.37428E+00 \\ 5.30286E+04 & 3.56055E+04 & 1.41966E+06 & -2.46706E-03 & 5.16232E+04 & 3.00011E+03 \\ 1.45955E+06 & -3.80114E+07 & 8.29711E+04 & -1.25984E+00 & 3.00033E+03 & 7.80655E+07 \end{bmatrix} \tag{3.52}$$

where the units are in pounds, inches, and radians.

$\underline{K}$ can be transformed to $\underline{C}$ by relating the strains $\underline{\varepsilon}_A$ in the energy method as defined in (3.39) to the displacements $\underline{u}$ in the finite element method as defined in (3.49). In matrix form, the strains $\underline{\varepsilon}_A$ are approximated by

$$\begin{bmatrix} \varepsilon_1^0 \\ \kappa_2^0 \\ \kappa_3^0 \\ 2\varepsilon_{12}^0 \\ 2\varepsilon_{13}^0 \\ \kappa_1^0 \end{bmatrix} = \begin{bmatrix} 1/L & & & & & \\ & 1/L & & & & \\ & & 1/L & & & \\ & -1/2 & & 1/L & & \\ & & 1/2 & & 1/L & \\ & & & & & 1/L \end{bmatrix} \begin{bmatrix} u \\ \psi \\ \phi \\ v \\ w \\ \theta \end{bmatrix}$$

or

$$\underline{\varepsilon}_A = \underline{Ru} \tag{3.53}$$

We already have an expression for the potential energy of the bay in (3.41). The potential energy can also be expressed as

$$U = \tfrac{1}{2}\underline{u}^T\underline{K}\underline{u} = \tfrac{1}{2}\underline{\varepsilon}_A^T\underline{R}^{-T}\underline{K}\underline{R}\underline{\varepsilon}_A \qquad (3.54)$$

Comparing (3.41) and (3.54) yields

$$\underline{C} = \frac{1}{L}(\underline{R}^{-T}\underline{K}\underline{R}^{-1}) \qquad (3.55)$$

Substituting the values for L, $\underline{R}$, and $\underline{K}$, we obtain

$$\underline{C}=\begin{bmatrix} 2.28458E+07 & -1.19338E+07 & -4.46836E+02 & 3.52693E+00 & 2.91657E+06 & 8.02752E+07 \\ -1.19338E+07 & 1.49007E+10 & -1.77292E+04 & 1.28000E+02 & 1.95829E+06 & -2.09062E+09 \\ -5.28000E+02 & -1.78735E+04 & 1.53347E+10 & -7.79157E+07 & 1.13600E+03 & 2.55830E+04 \\ 3.32553E+00 & 1.39636E+02 & -7.79157E+07 & 2.83328E+06 & -2.68955E-01 & -7.55852E+01 \\ 2.91657E+06 & 1.95830E+06 & 1.15433E+03 & -1.35688E-01 & 2.83928E+06 & 1.65006E+05 \\ 8.02753E+07 & -2.09062E+09 & 2.54100E+04 & -6.92912E+01 & 1.65018E+05 & 4.29360E+09 \end{bmatrix} \qquad (3.56)$$

where the units are in pounds, inches, and radians. The diagonal elements of (3.56) are in excellent agreement with those of (3.45). The axial and bending stiffnesses differ by less than five percent while the torsional and shear stiffnesses differ by less than ten percent. The off-diagonal coupling elements also agree if we consider the coupling ratios,

$$q_{ij} = \left| \frac{c_{ij}}{\sqrt{c_{ii}c_{jj}}} \right| \quad i \neq j \qquad (3.57)$$

If q_{ij} is less than about 0.1, coupling between degrees of freedom i and j is unimportant. In both cases, $q_{ij} << 0.1$

except for C_{43}, C_{51}, C_{61}, and C_{62}. These important coupling terms are in excellent agreement between the two methods. Thus, the energy of bars method for one bay and the finite element pin-jointed truss analysis for one bay each produce about the same stiffnesses when the results from the truss analysis are transformed into the form of those from the energy method. However, the original stiffnesses from the finite element truss analysis of one bay produce frequencies which better match the finite element results of Chapter 2 than do those from the energy of bars method.

3.2 BENDING FREQUENCIES FROM BERNOULLI-EULER BEAM THEORY

Consider the equation of motion of a Bernoulli-Euler beam in bending,

$$EI\frac{\partial^4 w}{\partial X^4} + m\frac{\partial^2 w}{\partial t^2} = 0 \qquad (3.58)$$

where w is the transverse deflection of the beam. If we assume harmonic motion with frequency , and if we define $\overline{w}$=w/L, where L is the length of the beam, and ξ=X/L, we can write

$$\bar{w}^{(iv)} - \omega^2\left(\frac{mL^4}{EI}\right)\bar{w} = 0 \qquad (3.59)$$

where the derivatives are now with respect to ξ. The solution to this equation is

$$\bar{w} = C_1\cos\lambda\xi + C_2\sin\lambda\xi + C_3\cosh\lambda\xi + C_4\sinh\lambda\xi \qquad (3.60)$$

$$\lambda^4 = \omega^2\left(\frac{mL^4}{EI}\right) \qquad (3.61)$$

The geometric boundary conditions at X=0 are

$$\begin{aligned} w &= 0 \\ w' &= 0 \end{aligned} \qquad (3.62)$$

With a concentrated mass M_c and a concentratd moment of inertia I_c at the tip of the beam, the natural boundary conditions at X=L are

$$\begin{aligned} \bar{w}''' + \beta\bar{w} &= 0 \\ \bar{w}'' - \alpha\bar{w}' &= 0 \end{aligned} \qquad (3.63)$$

where

$$\begin{aligned} \beta &= \omega^2 \frac{M_c L^3}{EI} = \lambda^4 \frac{M_c}{mL} \\ \alpha &= \omega^2 \frac{I_c L}{EI} = \lambda^4 \frac{I_c}{mL^3} \end{aligned} \qquad (3.64)$$

If we place (3.60) in (3.62) and (3.63), we obtain the characteristic equation in λ:

$$\begin{aligned} &\lambda^3\{\sin\lambda - \sinh\lambda + \gamma(\cos\lambda + \cosh\lambda)\} \\ &+ \beta\{\cos\lambda - \cosh\lambda - \gamma(\sin\lambda - \sinh\lambda)\} = 0 \\ &\gamma = \frac{\lambda(\cos\lambda + \cosh\lambda) - \alpha(\sin\lambda + \sinh\lambda)}{\lambda(\sin\lambda + \sinh\lambda) + \alpha(\cos\lambda - \cosh\lambda)} \end{aligned} \qquad (3.65)$$

We can solve this equation for λ and then use (3.61) to find the natural bending frequencies of the beam, ω.

For the SADE truss, the concentrated mass M_c is equal to the tip mass plus the joint mass at nodes 29, 30, 31, and 32, which adds up to 0.61479 lb-sec^2/in. To obtain the concentrated moment of inertia I_c, we average the joint mass at the four nodes at the free end of the truss and calculate the moment of inertia of these point masses about the neutral axis for bending, which passes through either nodes 29 and 32 or nodes 30 and 31. This moment of inertia is equal to 464.94 $\text{lb-sec}^2\text{-in}$. Note that Bernoulli-Euler beam theory does not distinguish between bending about the two neutral axes, which correspond to the pairs of closely spaced bending modes in the finite element analysis of Chapter 2. This is a result of $EI_1 = EI_2 = 1.3520\times10^{10}$ lb-in^2 and the fact that the shear stiffness is not accounted for.

The only quantity left to be found is the mass per unit length m. To calculate m we first average the joint mass over all joints (excluding the joint mass at nodes 29, 30, 31, and 32 at the tip of the truss). We then find the mass of a typical segment of the truss, such as the segment from X=27.5 inches to X=82.5 inches. In this segment there are eight 55 inch bars, five diagonal bars, and four average joints. We sum the mass of the bars and the joints and divide by 55 in. to obtain $m=2.733\times10^{-3}$ $\text{lb-sec}^2/\text{in}^2$. Since the length L of the SADE truss is 385 in., we then have $M_c/(mL)=0.58429$ and $I_c/(mL^3)=2.9811\times10^{-3}$.

The frequencies for the first four modes of the Bernoulli-Euler model are presented in Table 4. These results correspond to the first four bending mode pairs of the SADE truss.

3.3 BENDING FREQUENCIES FROM TIMOSHENKO BEAM THEORY

The equations of motion for a Timoshenko beam with no applied forces are

$$GA\left(\frac{\partial^2 w}{\partial X^2} + \frac{\partial \psi}{\partial X}\right) = m\ddot{w}$$

$$EI\frac{\partial^2 \psi}{\partial X^2} - GA\left(\frac{\partial w}{\partial X} + \psi\right) = i_R\ddot{\psi} \qquad (3.66)$$

where i_r is the rotary mass moment of inertia per unit length, w is the deflection of the midline, and ψ is the angle of rotation of the cross section (see Figure 5). If we assume harmonic motion with frequency ω and nondimensionalize by setting $\bar{w}=w/L$ and $\xi=X/L$, we can rewrite (3.66) as

$$\bar{w}'' + b^2 S\bar{w} + \psi' = 0$$

$$-\bar{w}' + S\psi'' - (1-b^2SR)\psi = 0 \qquad (3.67)$$

where a prime indicates differentiation with respect to ξ, and

$$b^2 = \omega^2\left(\frac{mL^4}{EI}\right)$$

$$S = \frac{EI}{GAL^2} \qquad (3.68)$$

$$R = \frac{i_R}{mL^2}$$

If $1-b^2SR > 0$ and we define

$$\lambda_{1,2} = \frac{b}{\sqrt{2}}\sqrt{\mp(S+R) + \sqrt{(S+R)^2 + 4\left(\frac{1}{b^2} - SR\right)}} \qquad (3.69)$$

we can rewrite the solution to (3.67) as

$$\bar{w} = C_1\cosh\lambda_1\xi + C_2\sinh\lambda_1\xi + C_3\cos\lambda_2\xi + C_4\sin\lambda_2\xi \quad (3.70)$$

$$\psi = C_1'\sinh\lambda_1\xi + C_2'\cosh\lambda_1\xi + C_3'\sin\lambda_2\xi + C_4'\cos\lambda_2\xi$$

However, from (3.67) we have

$$\psi' = -\bar{w}'' - b^2S\bar{w} \quad (3.71)$$

This equation can be used with (3.70) to give

$$\begin{aligned} C_1' &= -F_1C_1 \\ C_2' &= -F_1C_2 \\ C_3' &= F_2C_3 \\ C_4' &= -F_2C_4 \end{aligned} \quad (3.72)$$

$$F_1 = \frac{\lambda_1^2 + b^2S}{\lambda_1}$$

$$F_2 = \frac{\lambda_2^2 - b^2S}{\lambda_2}$$

There are four boundary conditions to consider. The two geometric boundary conditions at X=0 are

$$\begin{aligned} w &= 0 \\ \psi &= 0 \end{aligned} \quad (3.73)$$

The two natural boundary conditions at X=L are

$$-EI\frac{\partial\psi}{\partial X} = I_c\ddot{\psi}$$

$$-GA\left(\frac{\partial w}{\partial X} + \psi\right) = M_c\ddot{w} \qquad (3.74)$$

Using (3.68), we can rewrite the boundary conditions as

$$\bar{w} = 0$$

$$\psi = 0$$

$$\psi' - b^2\bar{I}_c\psi = 0 \qquad (3.75)$$

$$\bar{w}' - b^2 S\bar{M}_c\bar{w} + \psi = 0$$

$$\bar{I}_c = \frac{I_c}{mL^3}$$

$$\bar{M}_c = \frac{M_c}{mL}$$

If (3.70) are substituted into (3.75) the boundary conditions can be expressed in matrix form as

$$\begin{bmatrix} A_{11} & A_{12} & A_{13} & A_{14} \\ A_{21} & A_{22} & A_{23} & A_{24} \\ A_{31} & A_{32} & A_{33} & A_{34} \\ A_{41} & A_{42} & A_{43} & A_{44} \end{bmatrix} \begin{bmatrix} C_1 \\ C_2 \\ C_3 \\ C_4 \end{bmatrix} = \underline{0} \qquad (3.76)$$

where

$A_{11} = 1$ $\quad A_{12} = 0$ $\quad A_{13} = 1$ $\quad A_{14} = 0$

$A_{21} = 0$ $\quad A_{22} = -F_1$ $\quad A_{23} = 0$ $\quad A_{24} = -F_2$

$$A_{31} = F_1(b^2\bar{I}_c\sinh\lambda_1 - \lambda_1\cosh\lambda_1)$$

$$A_{32} = F_1(b^2\bar{I}_c\cosh\lambda_1 - \lambda_1\sinh\lambda_1)$$

$$A_{33} = F_2(\lambda_2\cos\lambda_2 - b^2\bar{I}_c\sin\lambda_2)$$

$$A_{34} = F_2(\lambda_2\sin\ {}_2 + b^2\bar{I}_c\cos\lambda_2)$$

$$A_{41} = (\lambda_1-F_1)\sinh\lambda_1 - b^2S\bar{M}_c\cosh\lambda_1$$

$$A_{42} = (\lambda_1-F_1)\cosh\lambda_1 - b^2S\bar{M}_c\sinh\lambda_1$$

$$A_{43} = (-\lambda_2+F_2)\sin\lambda_2 - b^2S\bar{M}_c\cos\lambda_2$$

$$A_{44} = (\lambda_2-F_2)\cos\lambda_2 - b^2S\bar{M}_c\sin\lambda_2$$

For the boundary conditions to be satisfied

$$\det(\underline{A}) = 0 \qquad (3.77)$$

This is the characteristic equation, which must be solved for b^2. Once we have a value of b^2 we can use (3.68) to find the corresponding natural frequency, ω.

In section 3.1, article A, it was shown that the bending of the SADE truss occurs in two principal directions, with corresponding bending stiffnesses EI_1 and EI_2 and shear stiffnesses GA_1 and GA_2. In addition, I_c changes slightly depending on the bending direction. The joint masses of nodes 29, 30, 31, and 32 from Table 2 can be used with Figure 3 to calculate I_{c1}=472.37 lb-sec^2-in and I_{c2}=457.50 lb-sec^2-in. The length L of the truss is 385 inches. The only quantity left to be found is the rotary inertia per unit length i_r. For i_r, consider one segment of the truss, such as the segment from X=27.5 inches to X=82.5 inches. The planes about which bending occurs pass through diagonally opposite nodes, slicing the truss cross section into two triangles. The rotary inertia of the segment is the sum of the products of the infinitessimal masses in the segment and their perpendicular distances to the bending plane. The rotary inertias of the bars can be found using integration and inertia transfer theorems; calculating the rotary inertia of the joint masses is straightforward. Once the total inertia is determined it is divided by 55 inches, yielding $i_{r1}=1.7592$ lb-sec^2 and $i_{r2}=1.6807$ lb-sec^2.

The results are presented in Table 4. Bending in principal direction 1 corresponds to the lower of the two frequencies in each bending mode pair from the finite element analysis. Bending in principal direction 2 corresponds to the higher of the two frequencies in each bending pair.

FIGURE 5

Timoshenko Beam

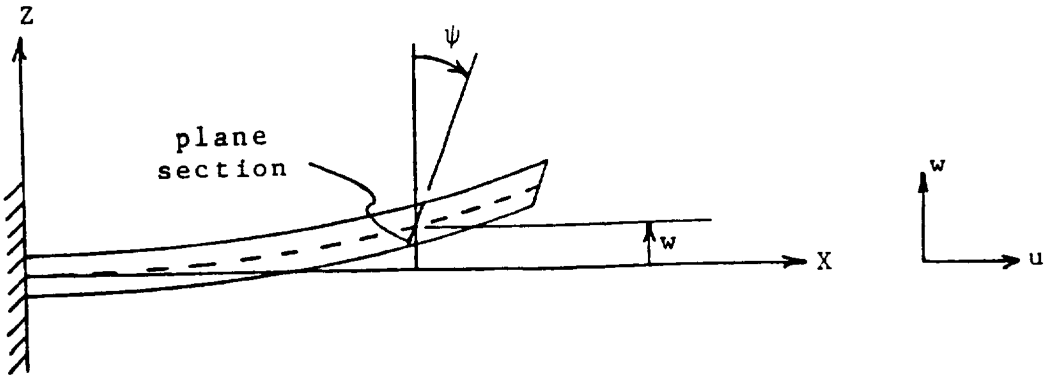

3.4 TORSIONAL FREQUENCIES

The equation of motion for a rod in torsion is

$$GJ\frac{\partial^2\theta}{\partial X^2} - i_p\frac{\partial^2\theta}{\partial t^2} = 0 \qquad (3.78)$$

where θ is the angular deflection along the rod. If we assume harmonic motion with frequency ω, and if we define $\xi=X/L$, we can write

$$\theta'' + \omega^2\frac{i_pL^2}{GJ}\theta = 0 \qquad (3.79)$$

where the derivatives are now with respect to ξ. The solution to this equation is

$$\theta = C_1\cos\lambda\xi + C_2\sin\lambda\xi \qquad (3.80)$$

$$\lambda^2 = \omega^2\frac{i_pL^2}{GJ} \qquad (3.81)$$

The geometric boundary condition at X=0 is

$$\theta = 0 \qquad (3.82)$$

With a concentrated polar moment of inertia I_p at the tip, the natural boundary condition at X=L is

$$\theta' - \alpha\theta = 0$$
$$\alpha = \omega^2\frac{I_cL}{GJ} = \lambda^2\frac{I_c}{i_pL} \qquad (3.83)$$

Placing (3.80) in (3.82) and (3.83), we obtain the characteristic equation in λ :

$$\lambda\cos\lambda - \alpha\sin\lambda = 0 \qquad (3.84)$$

We can solve this equation for λ and use (3.81) to find the torsional frequencies of the rod, ω.

For the SADE truss, the concentrated polar moment of inertia I_p is calculated about an axis in the X direction passing through the point Y=Z=27.5 inches using the tip mass and joint masses at nodes 29 through 32. It equals 929.87 lb-sec^2-in. For i_p consider a typical segment of the truss, such as the segment from X=27.5 inches to X=82.5 inches. We calculate the polar moment of inertia of the bars in this segment about an axis in the X direction passing through Y=Z=27.5 inches. We add to this the polar moment of inertia of four average joint masses (as derived in section 3.2) to obtain the total polar moment of inertia of this segment of the truss. Dividing this quantity by 55 inches yields the polar moment of inertia per unit length i_p=3.4399 lb-sec^2. GJ was found to be 3.6923x10^9 lb-in^2 in section 3.1, article A. With L=385 inches, $(I_pL)/(GJ)$=0.70213. We can now solve for the torsional frequencies of the SADE truss. The results are presented in Table 4.

3.5 AXIAL FREQUENCIES

The equation of motion of an axial bar is

$$EA\frac{\partial^2 u}{\partial X^2} - m\frac{\partial^2 u}{\partial t^2} = 0 \qquad (3.85)$$

This equation is of the same form as (3.78) for a torsional rod. If we define $\bar{u}$=u/L, the analysis for the natural frequencies of the axial bar is exactly the same as for the torsional rod. We only need to substitute EA for GJ, m for i_p, $\bar{u}$ for θ, and M_c for I_p.

For the SADE truss, EA was found to be 1.8310×10^7 lb in section 3.1, article A. M_c and m were calculated in section 3.2, so we know the parameters needed to solve for the axial frequencies of the SADE truss.

The result is presented in Table 4. Only the first axial frequency is calculated since the second axial mode is the eighteenth overall mode of the SADE truss with a pin-jointed finite element analysis, for which no finite element results were obtained.

4. SUPER-FINITE ELEMENT METHOD

The displacement vector $\underline{u}$ in (3.49) can be used to define the degrees of freedom of a super-finite element for the SADE truss. This super beam element consists of one bay of the truss. There are twelve degrees of freedom for this element: three translations and three rotations at each end. Thus, (3.49) defines the degrees of freedom at one end of an element.

Since there are seven bays in the SADE truss, it takes seven super-finite elements to model the truss. Therefore, there are now eight nodes in the finite element model. Since there are six degrees of freedom at each node, the model of the unrestrained structure has forty-eight degrees of freedom. Thus, the super-finite element model is much smaller than the ninety-six degree of freedom pin-jointed and one-hundred-and-ninety-two degree of freedom rigid-jointed finite element models of Chapter 2.

The 12x12 element stiffness matrix $\underline{K}_{xyz}$ for one bay can be found by using some of the results from Chapter 3. From (3.55), we can solve for $\underline{K}$ in terms of the $\underline{C}$ matrix, which was obtained by considering the bar energy of one bay:

$$\underline{K} = L\,\underline{R}^T\,\underline{C}\,\underline{R} \qquad (4.1)$$

Let $\underline{K}_R$ be the matrix defined in (4.1) after the rows and columns of $\underline{K}$ are rearranged to correspond to the degrees of freedom in $\underline{u}$ (as given by (3.49)). $\underline{K}_R$ is the 6x6 stiffness matrix for one bay when that bay is restrained at X=0, as discussed in Chapter 3. This matrix is the same for all bays of the SADE truss since $\underline{C}$ is the same for all bays. Now let $\underline{u}_2$ be the 6x1 displacement vector at the free end (X=L) of the bay as defined in (3.49), with $\underline{f}_2$ the corresponding 6x1 force vector as defined in (3.48). Also, let $\underline{u}_1$ and $\underline{f}_1$ be the displacement vector and force vector at X=0. ($\underline{u}_1=\underline{0}$ for now, since we have restrained this end of the bay). Then

$$\begin{bmatrix} \underline{f}_1 \\ \\ \underline{f}_2 \end{bmatrix} = \left[\begin{array}{c|c} \underline{K}_R' & \underline{K}_S \\ \hline \underline{K}_S^T & \underline{K}_R \end{array}\right] \begin{bmatrix} \underline{u}_1 \\ \\ \underline{u}_2 \end{bmatrix}$$

$$= \underline{K}_{xyz} \begin{bmatrix} \underline{u}_1 \\ \\ \underline{u}_2 \end{bmatrix} \qquad (4.2)$$

where $\underline{K}_R'$ and $\underline{K}_S$ are yet to be determined.

To determine $\underline{K}_S$ set $\underline{u}_1=\underline{0}$. Also, let all elements of $\underline{u}_2$ be zero except the ith element, which is set equal to one. We can find the force vector $\underline{f}_2$ which corresponds to this unit displacement state from $\underline{f}_2=\underline{K}_R\underline{u}_2$ (since $\underline{u}_1=\underline{0}$). The corresponding $\underline{f}_1$ can then be found by imposing the six static equilibrium conditions on the bay. This $\underline{f}_1$ is then the ith column of $\underline{K}_S$. $\underline{K}_R'$ is found in the same way, that is, $\underline{u}_2$ is set equal to $\underline{0}$ and we find $\underline{f}_2$ from $\underline{f}_2=\underline{K}_S{}^T\underline{u}_1$ with only the ith column of $\underline{u}_1$ nonzero and equal to one. Then $\underline{f}_1$ is found from the conditions of static equilibrium to give the ith column of $\underline{K}_R'$.

Performing the above analysis yields

$$\underline{K}_R = \begin{bmatrix} 4.29302E+05 & 0.00000E+00 & 5.60676E+04 & 1.54186E+06 & 1.54186E+06 & 0.00000E+00 \\ 0.00000E+00 & 5.60676E+04 & 0.00000E+00 & 0.00000E+00 & -1.54186E+06 & -1.54186E+06 \\ 5.60676E+04 & 0.00000E+00 & 5.60676E+04 & 0.00000E+00 & 1.54186E+06 & 0.00000E+00 \\ 1.54186E+06 & 0.00000E+00 & 0.00000E+00 & 8.48021E+07 & 0.00000E+00 & -4.24011E+07 \\ 1.54186E+06 & -1.54186E+06 & 1.54186E+06 & 0.00000E+00 & 3.24659E+08 & 4.24011E+07 \\ 0.00000E+00 & -1.54186E+06 & 0.00000E+00 & -4.24011E+07 & 4.24011E+07 & 3.24659E+08 \end{bmatrix} \qquad (4.3)$$

$$\underline{K}_R' = \begin{bmatrix} 4.29302E+05 & 0.00000E+00 & 5.60676E+04 & 1.54186E+06 & -1.54186E+06 & 0.00000E+00 \\ 0.00000E+00 & 5.60676E+04 & 0.00000E+00 & 0.00000E+00 & -1.54186E+06 & 1.54186E+06 \\ 5.60676E+04 & 0.00000E+00 & 5.60676E+04 & 0.00000E+00 & -1.54186E+06 & 0.00000E+00 \\ 1.54186E+06 & 0.00000E+00 & 0.00000E+00 & 8.48021E+07 & 0.00000E+00 & -4.24011E+07 \\ -1.54186E+06 & -1.54186E+06 & -1.54186E+06 & 0.00000E+00 & 3.24659E+08 & -4.24011E+07 \\ 0.00000E+00 & 1.54186E+06 & 0.00000E+00 & -4.24011E+07 & -4.24011E+07 & 3.24659E+08 \end{bmatrix} \qquad (4.4)$$

$$\underline{K}_S = \begin{bmatrix} -4.29302E+05 & 0.00000E+00 & -5.60676E+04 & -1.54186E+06 & -1.54186E+06 & 0.00000E+00 \\ 0.00000E+00 & -5.60676E+04 & 0.00000E+00 & 0.00000E+00 & 1.54186E+06 & 1.54186E+06 \\ -5.60676E+04 & 0.00000E+00 & -5.60676E+04 & 0.00000E+00 & -1.54186E+06 & 0.00000E+00 \\ -1.54186E+06 & 0.00000E+00 & 0.00000E+00 & -8.48021E+07 & 0.00000E+00 & 4.24011E+07 \\ 1.54186E+06 & 1.54186E+06 & 1.54186E+06 & 0.00000E+00 & -2.39857E+08 & -4.24011E+07 \\ 0.00000E+00 & -1.54186E+06 & 0.00000E+00 & 4.24011E+07 & 4.24011E+07 & -2.39857E+08 \end{bmatrix} \tag{4.5}$$

where the units are in pounds, inches, and radians. Therefore, we now have the element stiffness matrix in local coordinates $\underline{K}_{xyz}$. In this case, the local coordinates are in the same directions as the global coordinates, so we can assemble seven element stiffness matrices $\underline{K}_{xyz}$ to determine the 48x48 unrestrained structure stiffness matrix.

To assemble a structure mass matrix we lump the mass and inertia of the bays at their endpoints. The bay endpoints are now the nodes of the finite element model. Thus, node 1 is at X=0, node 2 is at X=55 inches, etc., and node 8 is at X=385 inches (see Figure 1). All eight nodes are at Y=Z=27.5 inches. The first three diagonal elements of the 48x48 unrestrained structure mass matrix are the lumped mass at node 1. The next diagonal element (element (4,4)) is the lumped polar inertia at node 1, about an axis in the X direction through the nodes. Element (5,5) is the lumped rotary inertia at node 1, about a plane at Z=27.5 inches parallel to the X-Y plane (for bending about Y), and element (6,6) is the lumped rotary inertia at node 1, about a plane at Y=27.5 inches parallel to the X-Z plane (for bending about Z). This sequence of six lumped parameters is repeated for the remaining seven nodes to make up the forty-eight diagonal elements of the lumped unrestrained structure mass matrix.

The lumped mass at a node is made up of the four joint masses at the X location of that node as well as the bar masses on each side of it. Let X_N be the X coordinate of node N. Then we lump the bar mass from $X=X_N-L/2$ to $X=X_N+L/2$ at node N, where L is the length of the bay. For node 1 this quantity equals 0.10630 lb-sec^2/in. For nodes

2 through 7 it is 0.15522 lb-sec^2/in and for node 8 it is 0.67686 lb-sec^2/in (including the tip mass). The lumped polar inertia at node N is the sum of the polar moments of inertia of all bar and joint masses from X_N-L/2 to X_N+L/2. At node 1 this quantity equals 131.28 lb-sec^2-in, at nodes 2 through 7 it is 196.63 lb-sec^2-in, and at node 8 it is 994.23 lb-sec^2-in. The lumped rotary inertia, which is the same for bending about Y or Z, is the sum of the rotary moments of inertia of all bar and joint masses from X_N-L/2 to X_N+L/2. For node 1 it equals 65.642 lb-sec^2-in, for nodes 2 through 7 it is 98.314 lb-sec^2-in, and for node 8 it is 497.12 lb-sec^2-in.

The structure must now be totally restrained at its base (X=0). Therefore, rows and columns 1 through 6 are removed from the unrestrained structure stiffness and mass matrices to form the restrained structure stiffness and mass matrices, and rows 1 through 6 are removed from the 48x1 unrestrained displacement vector. The restrained system (2.19) has now been defined. The natural frequencies and mode shapes are solved for using the methods of Chapter 2. The results are presented in Table 4.

5. COMPARISON OF METHODS FOR FREQUENCY DETERMINATION

The results from chapters 2, 3, and 4 are presented in Table 4. The pin-jointed and rigid-jointed finite element results are in very good agreement through the third bending mode pair (modes 8 and 9). After mode 9, the rigid-jointed model encounters closely spaced modes caused by the vibrations of individual bar members of the truss (this phenomenon will be addressed in the two subsequent chapters). Therefore, up to mode 9, both standard finite element models can be used as a basis to judge the continuum and super-finite element results. Past mode 9, the continuum and super-finite element results should be judged against the pin-jointed finite element frequencies only, since the pin-jointed, continuum, and super-finite element models do not account for the closely spaced bar modes, while the rigid-jointed model does account for the closely spaced bar modes.

The first frequency from the Bernoulli-Euler continuum model provides a good estimate of the average of the finite element frequencies for the first bending mode pair. However, the subsequent frequency values diverge rapidly from the finite element results.

In contrast, the Timoshenko continuum model does an excellent job of finding the bending frequencies of the SADE truss. As discussed in section 3.3, the Timoshenko model distinguishes between the two modes in each bending mode pair. In the first two bending mode pairs, which correspond to overall structural modes 1, 2, 4, and 5, the Timoshenko continuum frequencies differ from both the pin-jointed and rigid-jointed finite element results by less than four percent. In modes 8 and 9, the Timoshenko continuum results differ by four percent from the pin-jointed frequencies and by less than nine percent from the rigid-jointed frequencies. In the modes 11 and 12, the difference from the pin-jointed frequencies is still less than seven percent.

The torsional continuum model provides good agreement with the finite element results in the first two torsional modes. The first torsional mode of the SADE truss is the third overall structural mode. In this mode the torsional continuum result differs from the finite element results by less than five percent. In the second torsional mode, which is the seventh overall mode, the torsional continuum frequency differs by less than seven percent from the finite element results. The results start to diverge in the third torsional mode, which is the tenth overall mode. Here the torsional continuum frequency differs from the pin-jointed result by fifteen percent.

The frequency obtained from the axial continuum model for the first axial mode of the SADE truss is in excellent agreement with the finite element results, differing by only three percent. Only the first axial frequency is calculated since the second axial mode is the eighteenth overall mode of the SADE truss with a pin-jointed finite element analysis, for which no finite element results were obtained.

The super-finite element model has two inherent advantages over the continuum models: it yields frequencies for all three mode types (bending, torsional, and axial, including all couplings) at once, and it provides eigenvectors to specify the mode shapes. In bending, the super-finite element model does as well as the Timoshenko continuum model in the lower modes, although it does slightly worse in higher modes, where the seven element discretization comes into play. For the first bending mode pair the super-finite element results differ from the finite element frequencies by less than two percent. In the second pair the difference is about five percent or less. For the third bending mode pair the frequencies from the super-finite element model differ from the pin-jointed results by less than seven percent and from the rigid-jointed results by less than thirteen percent. In the fourth bending mode pair, corresponding to the eleventh and twelfth overall modes of the SADE truss, the difference is less than thirteen percent from the pin-jointed results. The super-finite element model is not quite as good at matching the torsional finite element frequencies as is the torsional continuum model. It differs from the finite element results by twelve percent in the first torsional mode, by over eight percent in the second torsional mode, and by twelve percent from the pin-jointed frequency in the third torsional mode. The super-finite element result for the first axial mode is not in as good agreement as the axial continuum result, although it only differs from the finite element results by about six percent.

TABLE 4

SADE Natural Frequencies
(All frequencies in Hz)

Finite Element Methods		Continuum Methods				Super-Finite Element Method	Mode Number	Mode Shape*
Pinned Joints	Rigid Joints	Bernoulli-Euler	Timoshenko	Torsional	Axial			
4.05	4.07	4.55	4.21			4.12	1	1 Bending
4.50	4.51		4.28			4.57	2	"
12.6	12.7			13.2		14.1	3	1 Torsional
25.8	25.6	37.3	25.3			26.5	4	2 Bending
27.0	26.7		26.9			28.2	5	"
35.9	35.6				34.8	37.9	6	1 Axial
44.9	44.8			47.8		48.6	7	2 Torsional
59.5	55.8	100.	57.4			61.0	8	3 Bending
60.5	57.2		61.9			64.3	9	"
76.5	68.9			88.0		85.4	10	3 Torsional
80.2	69.8	182.	85.2			90.2	11	4 Bending
89.5	71.0		92.7			98.9	12	"
95.0	71.2					106.		
102.	72.8					116.		
110.	72.9					124.		
112.	73.5					132.		
118.	73.8					134.		

---

*Mode shapes apply to all methods except the rigid-jointed finite element model past the third bending mode pair, since the subsequent closely spaced modes obtained with this model are chacterized by local bar vibrations. No eigenvectors were obtained for modes past mode 12.

6. VIBRATIONS OF A TWO-DIMENSIONAL MODEL OF THE SADE TRUSS

6.1 STANDARD FINITE ELEMENT METHODS

To determine the effects of individual bar natural frequencies on the global modes of a space truss, a simpler, two-dimensional version of the SADE truss is considered. This truss has the same configuration as the general two-dimensional truss of Figure 6. The bar elements have the same dimensions and properties as the bars of the three-dimensional truss of Chapter 2. The joint masses of the SADE truss from Table 2 are averaged, and this average joint mass is placed at each node of the two-dimensional truss. Also, one-half of the SADE tip mass is divided equally between nodes 15 and 16. In addition, the mass of the bars in the three-dimensional truss which would enter the nodes of the two-dimensional truss from the Z dimension is accounted for. This extra mass is from those half bars which do not lie in the X-Y plane which remain after the three-dimensional truss is sliced down the middle at Z=27.5 inches. The mass of each half bar is lumped at that node of the two-dimensional model where the bar would enter from the Z dimension.

The two-dimensional truss is analyzed with three types of finite element models. First, a standard pin-jointed finite element model is employed (see section 2.2), using a consistent mass matrix to model the mass of the bars in the truss. This model has two translational degrees of freedom at each node. Nodes 1 and 2 are pinned to restrain the structure, so there are 28 degrees of freedom in the restrained model. Next, a standard rigid-jointed finite element model is used (see section 2.3). There are now three degrees of freedom, two translations and one rotation, per unrestrained node, plus the rotations at nodes 1 and 2, yielding 44 degrees of freedom in the restrained model. The results for these two standard finite element models are presented in Table 5 and discussed in the section below.

6.2 REFINED FINITE ELEMENT MODEL WITH ADDITIONAL NODES AT BAR MIDPOINTS

The truss is analyzed next with a refined rigid-jointed finite element model, with extra nodes at all bar midpoints. There are now forty-five nodes with three degrees of freedom per node. The two translational degrees of freedom at nodes 1 and 2 of Figure 6 are restrained, so the restrained model now contains 131 degrees of freedom.

The frequency results for the standard finite element models and the refined finite element model with additional nodes at bar midpoints are presented in Table 5, and the eigenvectors are in Appendix C. The standard pin-jointed frequencies provide good estimates of the pin-jointed bending and axial frequencies of the three dimensional SADE truss (compare Tables 4 and 5). The frequencies from the standard rigid-jointed model of the two-dimensional truss match the pin-jointed frequencies for the two-dimensional truss through the fourth mode. However, the fifth through eleventh modes of the rigid-jointed model of the two-dimensional truss are closely spaced. These closely spaced modes are characterized by the domination of vibrations, relative to the joints, of the seven individual diagonal bars in the truss. This phenomenon is explained more fully in Chapter 7.

The eigenvectors of the refined rigid-jointed model with additional nodes at bar midpoints validate the fact that the closely spaced modes are a result of individual bar vibrations. The frequencies obtained with this model match the results from the two standard finite element models up to the fourth mode. However, the refined rigid-jointed model more accurately locates the closely spaced modes than does the standard rigid-jointed model, placing them in a lower frequency band. Now modes 5 through 11 are characterized by vibrations of the seven diagonal bars. The eigenvectors for these modes show that the largest deflections occur at the midpoints of these bars. The diagonal bars also vibrate relative to the joints in modes 3 and 4, although not as severely as in the band of closely spaced modes from mode 5 to mode 11. In mode 12, the displacements of the shorter bar midpoints are about two orders of magnitude greater than the displacements of the diagonal bar midpoints. The displacements of the shorter bar midpoints are also larger than the joint displacements in mode 12, so it appears that a band of modes which are characterized by vibrations of the shorter bars begins with mode 12.

The finite element models of the two-dimensional truss do not accurately predict the closely spaced bar modes in the three-dimensional truss. For the three-dimensional SADE truss, the bar modes begin with mode 10 at 68.9 Hz, according to the standard rigid-jointed model (see Table 4). In contrast, the standard rigid-jointed model for the two-dimensional truss shows the bar modes beginning at 82.0 Hz. (The correct value for the two-dimensional truss, as given by the refined rigid-jointed finite element model with nodes at bar midpoints, is actually 59.5 Hz.) The difference between the three-dimensional and two-dimensional cases appears to be due to the presence of many more diagonal bars in the three-dimensional truss than in the two-dimensional truss. This would result in a greater number of closely spaced modes characterized by vibrations of the diagonal bars for the three-dimensional truss. Since there are more modes, it makes sense that the frequency band containing these modes is larger than the two-dimensional band, and thus, the band for the three-dimensional truss begins at a lower frequency than does the band for the two-dimensional truss.

TABLE 5

Natural Frequencies of a Two-Dimensional Model of SADE Truss
(All frequencies in Hz)

Finite Element Model			Mode No.	Mode Shape for Pin-Jointed Model
Pin-Jointed	Rigid-Jointed	Rigid-Jointed with Additional Nodes at Bar Midpoints		
4.17	4.18	4.19	1	1 Bending
25.7	25.7	25.6	2	2 Bending
34.8	34.7	34.6	3	1 Axial
58.9	57.9	55.5	4	3 Bending
87.8	81.9	61.4	5	4 Bending
103.	82.0	61.5	6	5 Bending
125.	83.8	62.4	7	2 Axial
137.	84.9	63.5	8	6 Bending
155.	88.6	64.2	9	7 Bending
173.	93.5	68.6	10	8 Bending
190.	94.7	70.7	11	3 Axial
196.	99.0	82.8	12	9 Bending
224.	101.	84.5		
257.	105.	88.8		
318.	111.	91.5		
340.	113.	100.		
352.	130.	103.		

7.1 STANDARD FINITE ELEMENT METHODS

A simple two-dimensional truss with no lumped masses is considered to illustrate the effects of individual bar natural frequencies on the global modes of the truss. The truss is shown in Figure 6. The only mass in the truss is from the bars, which have the same dimensions and properties as the bars of the three dimensional truss of Chapter 2 (see Table 3).

The truss is first analyzed with a standard pin-jointed finite element model (see section 2.2), using a consistent mass matrix to model the bar mass. There are two translational degrees of freedom at each node, which yields 28 restrained degrees of freedom after nodes 1 and 2 are pinned. The results are presented in Table 6 and Appendix C. The frequencies are substantially higher than those of the two-dimensional SADE model of Chapter 6, due to the absence of the joint masses and tip mass.

The truss is also analyzed using the continuum methods of Chapter 3. Using the methods of section 3.1, part A, we find that the equivalent stiffness properties of the truss are $EI=6.5960\times10^{9}$ lb-in^{2}, $GA=1.0693\times10^{-1}$ lb, and $EA=8.7220\times10^{6}$ lb. The equivalent mass properties are $m=4.8627\times10^{-4}$ lb-sec^{2}/in^{2} and $i_r = 1.9438\times10^{-1}$ lb-sec^{2}. The resulting continuum frequencies are also shown in Table 6. The Bernoulli-Euler continuum bending frequencies are not reliable, except in the first mode. However, the axial continuum frequencies and Timoshenko continuum bending frequencies compare very well with the pin-jointed finite element results, even in the higher modes.

The truss is next analyzed with a standard rigid-jointed finite element model (see section 2.3), with nodes only at bar endpoints. There are now three degrees of freedom, two translations and one rotation, at each node. The translational degrees of freedom at nodes 1 and 2 are restrained to yield 44 degrees of freedom in the restrained model. The results are presented in Table 6 and Appendix C.

The results obtained with the standard rigid-jointed model are in good agreement with the pin-jointed results in the first two modes. However, the results start to diverge in the third mode. The third natural frequency is near the first natural bending frequency of the longer, diagonal bars in the truss. The first natural bending frequency of the diagonal bars is 79.8 Hz with clamped endpoints and 35.2 Hz with pinned endpoints (using standard Bernoulli-Euler beam theory). The first natural bending frequency of the shorter, 55 inch bars is 160. Hz with clamped endpoints and 70.4 Hz with pinned endpoints. The seven closely spaced modes from 82.0 Hz to 99.2 Hz obtained with the standard rigid-jointed model appear to be characterized by vibrations, relative to the joints, of the diagonal bars.

The pin-jointed finite element model completely missed this phenomenon. After mode 2, the results obtained with this model (or the continuum models) are completely unreliable. The element stiffness matrices in the pin-jointed model contain only extensional stiffnesses. Therefore, the pin-jointed model cannot account for bending vibrations relative to the joints of the bar elements of the truss. The continuum models are inherently unable to account for the bending vibrations of individual elements of the truss. However, the rigid-jointed element stiffness matrices do account for the bending stiffnesses of the individual bars in the truss. The rigid-jointed model therefore is influenced by first bending mode vibrations of the diagonal bars, near the first clamped-clamped natural frequency of these bars (79.8 Hz). The standard rigid-jointed model of the three-dimensional SADE truss also found closely spaced modes from 68.9 Hz characterized by vibrations of the diagonal bars (see Table 4). However, the results in the next two sections show that although the standard rigid-jointed model finds the closely spaced bar modes, it does not place these modes in the correct frequency band.

7.2 REFINED FINITE ELEMENT METHOD WITH ADDITIONAL NODES AT BAR MIDPOINTS

The general two dimensional truss of Figure 6 is now analyzed with a refined rigid-jointed finite element model, with an extra node at all bar midpoints. Therefore, the refined model contains forty-five nodes. Since there are three degrees of freedom per node (two translations and one rotation), the restrained model contains 131 degrees of freedom, after nodes 1 and 2 in Figure 6 are pinned. The first bending modes of the individual bars can now be modeled more accurately since the refined model with nodes at bar midpoints takes the deflection at the bar midpoints into account. This model can also accurately account for the second bending mode of the bars, since it also considers the rotations at the bar midpoints.

The results from the refined rigid-jointed model are presented in Table 6 and Appendix C. The frequency for the first mode at 12.3 Hz matches those from the pin-jointed and standard rigid-jointed finite element analyses. This mode is the usual first bending mode of the truss. Table 7 shows that the maximum deflection at a diagonal bar midpoint, the maximum deflection at a joint, and the maximum deflection at a shorter, 55 inch bar midpoint, are about the same for the first mode. The maximum deflections occur at the free end of the truss, as would be expected in the first bending mode. The first mode is plotted in Figure 6, using the eigenvector from the refined rigid-jointed finite element model with additional nodes at bar midpoints. The actual physical truss is 385 inches long, and the eigenvectors are normalized to a maximum deflection of one inch in a coordinate direction. In the figure, the truss is 4.2 inches long and the maximum deflection of any node in a coordinate direction is shown as 0.2 inches. The eigenvectors were scaled accordingly to make the plots.

The frequency for the second mode from the refined rigid-jointed model, at 49.8 Hz, is slightly lower than the corresponding second mode frequencies from the pin-jointed and standard rigid-jointed models, but this mode is still the second bending mode, as the eigenvector plot of Figure 6 shows. However, notice that the diagonal bars have started to vibrate relative to the joints and that the maximum deflections occur at the diagonal bar midpoints. Table 7 shows that the maximum of the diagonal bar midpoint deflections is about twice as great as the maximum of the joint deflections or the maximum of the shorter bar midpoint deflections.

The third natural frequency from the refined rigid-jointed model, at 61.3 Hz, is not at all close to the corresponding frequencies from the pin-jointed and standard rigid-jointed models. With the pin-jointed and standard rigid-jointed models, the third mode is an axial mode, but the refined rigid-jointed model shows that the third mode of the structure is not an axial mode. The plot of the third mode (at 61.3 Hz) in Figure 6 reveals that this mode is characterized by severe vibrations of the diagonal bars, while the deflections of the joints is imperceptible. While some of the shorter bar midpoints show a deflection, these deflections only occur in those bays of the truss where the diagonal bars are most excited. Table 7 shows that the maximum deflection of a diagonal bar midpoint is two orders of magnitude greater than the maximum deflection at a joint and significantly greater than the maximum deflection at a shorter bar midpoint. The deflection of the shorter bar midpoints appears to be a secondary phenomenon caused by the need for the boundary conditions to be satisfied at the rigid joints. While a joint is free to rotate, the relative angles at a joint between the bars which are connected at that joint must remain constant.

The next six modes from the refined rigid-jointed model are similar to the third mode, at 61.3 Hz. Table 7 and the eigenvectors in Appendix C reveal that all seven of the modes in the closely spaced band from 61.3 Hz to 74.2 Hz are characterized by vibrations of the diagonal bars, although the joint deflections become more significant as frequency is increased. As discussed above, the pin-jointed finite element model and the continuum models completely miss this band, while the standard rigid-jointed finite element model found the band, but placed it in the wrong location (see Table 6). The analysis of the truss with a finite element model employing exact dynamic stiffness coefficients presented in the next section validates the results of the refined rigid-jointed finite element model. The first natural bending frequency of the diagonal bars is 35.2 Hz with pinned endpoints and 79.8 Hz with clamped endpoints, so the band of diagonal bar modes lies somewhere between these two values, but closer to that obtained with the clamped (rigid) endpoints.

The next three modes, modes 10, 11, and 12, from the refined rigid-jointed model are very similar to each other. They are characterized by severe vibrations relative to the joints of the shorter, 55 inch bars. Mode 10, at 82.7 Hz, is plotted in Figure 6. Note the symmetry and the second bending mode shape of the diagonal bars, which deflect slightly to satisfy the boundary conditions at the joints. However, Table 7 shows that the deflections of the shorter bar midpoints are two orders of magnitude greater than the deflections of the joints and one order of magnitude greater than the deflections of the diagonal bar midpoints. Thus, it appears that a band of modes characterized by vibrations of the shorter bars begins at 82.7 Hz. The first natural bending frequency of the shorter bars is 70.4 Hz with pinned endpoints and 160. Hz with clamped endpoints. Therefore, the band of shorter bar modes begins after the first natural pinned bending frequency of the shorter bars. Since there are twenty-two shorter bars in the truss, there are most likely twenty-two modes in the band of shorter bar modes, so this band may extend to near the first natural clamped bending frequency of the shorter bars.

7.3 FINITE ELEMENT MODEL WITH EXACT DYNAMIC STIFFNESS COEFFICIENTS

To validate the natural frequencies obtained for the general two-dimensional truss with the refined rigid-jointed finite element model with additional nodes at bar midpoints, a finite element analysis with exact dynamic stiffness coefficients is performed. The dynamic stiffness coefficients modify the terms in the rigid-jointed bar element stiffness matrix of section 2.3 (see (2.22)), making these terms frequency dependent. Note that for the general two-dimensional truss of Figure 6 in the X-Y plane, the rows and columns of the element stiffness matrix (2.22) corresponding to the translational degree of freedom in Z and the rotational degrees of freedom about X and Y are not needed, but the more general case is presented here.

The dynamic stiffness coefficients used, which neglect transverse shear and rotary inertia, are those of Anderson (reference 7), as obtained from Howson (reference 8). For nonzero terms $K_{i,j}$ of the element stiffness matrix (2.22), a dynamic stiffness coefficient $F_{i,j}$ is multiplied by $K_{i,j}$, and the resulting frequency dependent product replaces $K_{i,j}$ in the element stiffness matrix. We assume that there is no prestressing and use the notation of Chapter 2, where L is the length of the bar element, and define

FIGURE 6

General Two-Dimensional Truss
and Mode Shapes with Additional Nodes at Bar Midpoints

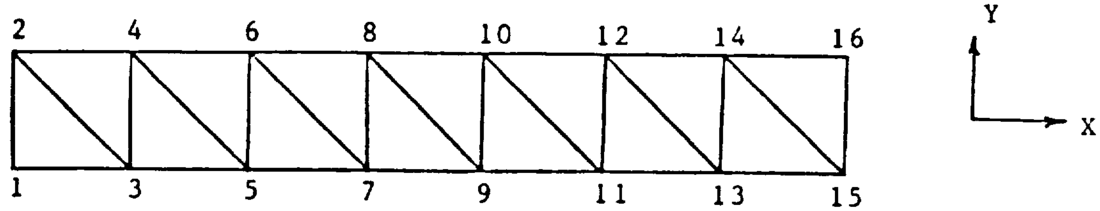

General Truss
(Nodes at bar midpoints are not labelled)

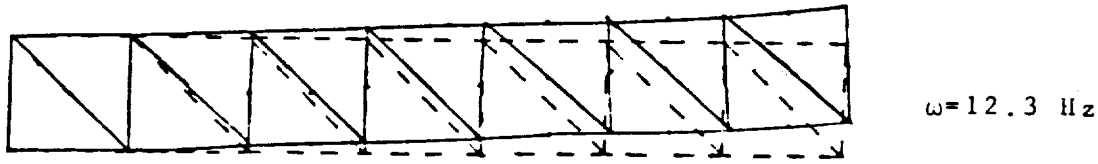

First Bending

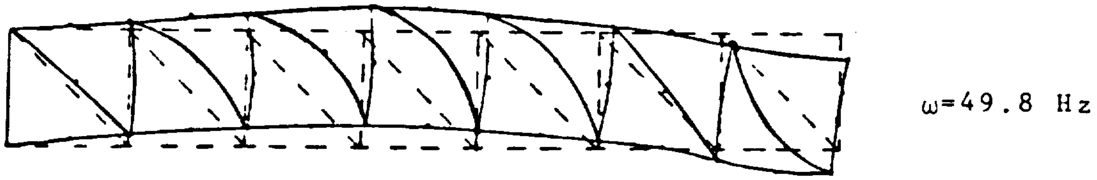

Second Bending

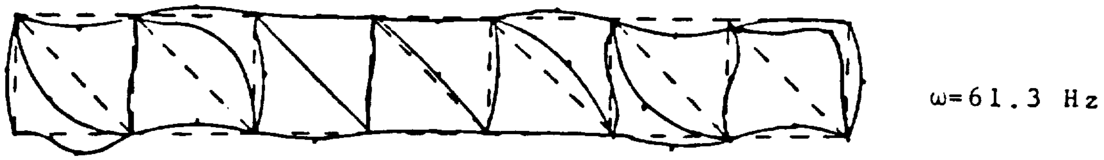

First of Seven Closely Spaced Modes
Characterized by Diagonal Bar Vibrations

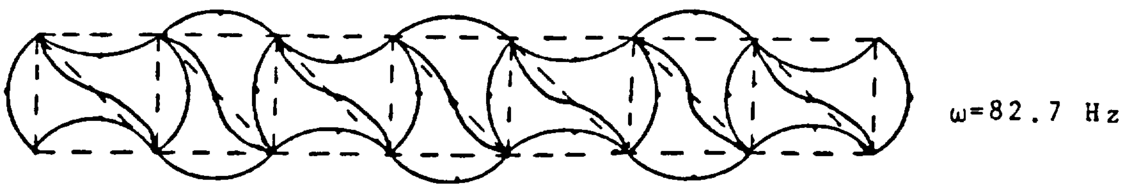

First of the Closely Spaced Modes Characterized
by Shorter 55 inch Bar Vibrations

$$g^2 = \omega^2 \frac{mL^2}{EA} \qquad h^2 = \omega^2 \frac{mL^2}{GJ} \tag{7.1}$$

$$d_k^4 = \omega^2 \frac{mL^4}{EI_k} \tag{7.2}$$

where k can be 2 or 3, with k=2 corresponding to EI_Y and k=3 corresponding to EI_Z. Also let

$$\Delta_k = 1 - \cosh d_k \cos d_k \tag{7.3}$$

Then for the nonzero elements in the upper triangle (j>i) of (2.22),

$$F_{1,1} = g \cot g$$

$$F_{1,7} = g \csc g$$

$$F_{2,2} = \frac{d_3^2(\cosh d_3 \sin d_3 + \sinh d_3 \cos d_3)}{12\Delta_3}$$

$$F_{2,6} = \frac{d_3^3 \sinh d_3 \sin d_3}{6\Delta_3}$$

$$F_{2,8} = \frac{d_3^3(\sin d_3 + \sinh d_3)}{12\Delta_3}$$

$$F_{2,12} = \frac{d_3^2(\cosh d_3 - \cos d_3)}{6\Delta_3}$$

$$F_{3,3} = \frac{d_2^3(\cosh d_2 \sin d_2 + \sinh d_2 \cos d_2)}{12\Delta_2}$$

$$F_{3,5} = \frac{d_2^2 \sinh d_2 \sin d_2}{6\Delta_2}$$

$$\begin{aligned}
F_{3,9} &= \frac{d_2^{\,3}(\sin d_2 + \sinh d_2)}{12\Delta_2} \\
F_{3,11} &= \frac{d_2^{\,2}(\cosh d_2 - \cos d_2)}{6\Delta_2} \\
F_{4,4} &= h\coth \\
F_{4,10} &= h\operatorname{csch} \\
F_{5,5} &= \frac{d_2(\cosh d_2 \sin d_2 - \sinh d_2 \cos d_2)}{4\Delta_2} \\
F_{5,9} &= F_{3,11} \\
F_{5,11} &= \frac{d_2(\sinh d_2 - \sin d_2)}{2\Delta_2} \\
F_{6,6} &= \frac{d_3(\cosh d_3 \sin d_3 - \sinh d_3 \cos d_3)}{4\Delta_3} \\
F_{6,8} &= F_{2,12} \\
F_{6,12} &= \frac{d_3(\sinh d_3 - \sin d_3)}{2\Delta_3}
\end{aligned} \tag{7.4}$$

and

$$F_{i+6,j+6} = F_{i,j}$$

The frequency dependent restrained structure stiffness matrix for the general two-dimensional truss of sections 7.1 and 7.2 is assembled in the same manner as is the standard rigid-jointed restrained stiffness matrix of section 7.1. Therefore, the node numbering scheme is that of Figure 6, and the frequency dependent restrained structure stiffness matrix $\underset{\sim}{K}(\omega)$ is of order 44. No mass matrix is needed, since the mass of the bars is accounted for in the frequency dependent dynamic stiffness coefficients. We need only to solve

$$\det(\underline{K}(\omega)) = 0 \qquad (7.5)$$

to obtain the natural frequencies of the truss. If lumped inertias were present at the nodes, they would be placed in a diagonal mass matrix $\underline{J}$ and the equation to be solved for the natural frequencies would be

$$\det(\underline{K}(\omega) - \omega^2\underline{J}) = 0 \qquad (7.6)$$

For the general two dimensional truss, which contains no lumped inertias, the results are presented in Table 6. The maximum difference in the first twelve modes between frequencies from the finite element model with exact dynamic stiffness coefficients and the refined rigid-jointed finite element model with additional nodes at bar midpoints is 1.1 percent in mode 6. The maximum difference in the first eighteen modes is 2.5 percent in mode 17. Therefore, the results from the finite element model with exact dynamic stiffness coefficients validate the frequencies obtained with the refined rigid-jointed model.

TABLE 6

Natural Frequencies of General Two-Dimensional Truss
(All frequencies in Hz)

Continuum Methods			Finite Element Methods				Mode No.	Mode Shape for Continuum and Pin-Jointed Finite Element Models
Bernoulli -Euler	Timoshenko	Axial	Pinned Joints	Rigid Joints	Rigid Joints with Additional Nodes at Bar Midpoints	Rigid Joints with Exact Dynamic Stiffness Coefficients		
13.9	12.6		12.2	12.2	12.3	12.2	1	1 Bending
87.1	55.8		55.3	53.2	49.8	49.5	2	2 Bending
		87.0	88.1	76.6	61.3	60.7	3	1 Axial
244.	120.		123.	82.0	61.4	60.8	4	3 Bending
478.	184.		195.	82.8	62.4	61.8	5	4 Bending
790.	248.		254.	85.1	63.3	62.6	6	5 Bending
		261.	276.	87.9	64.1	63.5	7	2 Axial
1180.	308.		336.	92.1	64.6	64.0	8	6 Bending
1650.	356.		379.	94.7	74.7	74.1	9	7 Bending
2200.	388.		404.	99.2	82.7	82.1	10	8 Bending
		435.	421.	105.	84.4	83.8	11	3 Axial
2820.	442.		498.	111.	91.2	90.4	12	9 Bending
			572.	128.	99.6	98.8		
			656.	133.	102.	101.		
			718.	149.	108.	107.		
			751.	157.	116.	114.		
			757.	188.	123.	120.		

TABLE 7

Node Deflections of General Two-Dimensional Truss

Mode No.	Modal Frequency (Hz)	Magnitude of Node Deflection		
		Largest Deflection at a Joint	Largest Deflection at a Diagonal Bar Midpoint	Largest Deflection at a 55 inch Bar Midpoint
1	12.3	1.005	0.938	1.000
2	49.8	0.657	1.148	0.657
3	61.3	0.092	1.330	0.432
4	61.4	0.062	1.412	0.466
5	62.4	0.053	1.396	0.412
6	63.3	0.072	1.406	0.354
7	64.1	0.127	1.313	0.394
8	64.6	0.227	1.297	0.496
9	74.7	0.422	1.170	0.537
10	82.7	0.062	0.127	1.001
11	84.4	0.059	0.236	1.000
12	91.2	0.099	0.362	1.002

8. CONCLUSIONS

The dynamic modes of the SADE truss have been obtained using finite element and continuum models, and the results are presented in Table 4 and Appendix C. The dynamics of a two-dimensional model of the SADE truss and a general two-dimensional truss have also been analyzed, and these results are presented in Tables 5 and 6 and Appendix C.

The results of the truss analyses accomplished in this study yield two major conclusions. Firstly, continuum models of beam-like trusses can produce global natural frequencies which are very close to standard pin-jointed finite element results. However, the results from refined finite element models reveal that the modes obtained with standard finite element and continuum models are inaccurate except in the lowest modes, since the standard finite element and continuum models do not adequately account for the effects of individual bar vibrations on the global modes of the truss.

The Timoshenko continuum model, the torsional continuum model, and the axial continuum model yield results which are close to the bending, torsional, and axial frequencies, respectively, obtained with a standard finite element model with pin-jointed bar elements (three degrees of freedom per node). The Bernoulli-Euler continuum model produces an accurate bending frequency only for the first bending mode.

The standard finite element model with rigid-jointed bar elements (six degrees of freedom per node) with nodes only at bar endpoints yields results which are very close to the pin-jointed finite element results in the lower modes. However, above a frequency corresponding to the lowest natural bending frequency of the individual bars in the truss, assuming pinned endpoints, the standard rigid-jointed finite element model yields a group of closely spaced bar modes characterized by vibrations, relative to the joints, of the individual bars in the truss. These bar modes occur between the first natural bending frequency of a bar with pinned endpoints and the first natural bending frequency of a bar with clamped endpoints. For the trusses considered in this study, there are two types of bars in the truss (with the same cross-sectional properties but different lengths), so the standard rigid-jointed model finds two groups of closely spaced bar modes characterized by first bending mode vibrations of the individual bars.

The standard pin-jointed finite element and continuum models completely miss these groups of bar modes. Therefore, it appears that continuum models such as those of Noor, Anderson, and Greene (reference 6) and Berry, Yang, and Skelton (reference 9) may not be directly applicable to determining the modes of lattice structures, except in the lowest modes and perhaps those modes with frequencies which are relatively far from any bar natural frequencies. These continuum methods do not adequately model the individual bars of the truss.

While a standard rigid-jointed finite element model with nodes only at bar endpoints finds the closely spaced bar modes, it does not place these modes at the right frequencies. Therefore, analyses of lattice structures which take advantage of the periodicity of such structures and which employ standard rigid-jointed bar elements with nodes only at bar endpoints, such as that of Leung (reference 10), may yield inaccurate results. A refined rigid-jointed finite element model with additional nodes at all bar midpoints places the closely spaced bar modes in a significantly lower frequency band than does the standard rigid-jointed model, although the band still lies between the first pinned natural bending frequency and the first clamped natural bending frequency of that type of bar. The frequencies from the refined rigid-jointed model are validated by a finite element analysis employing exact dynamic stiffness coefficients. Related analyses of these types of trusses with individual bar vibration effects have been done by Schroeder (reference 11). However, even the refined rigid-jointed finite element model may yield inaccurate results if the slenderness ratios of the bars are high enough, due to buckling and eccentricity effects, unless the stiffness of the bars is modified as is shown by Regelbrugge and Park (reference 12). But in general, it appears that a refined rigid-jointed model with additional nodes at all bar midpoints is the simplest finite element model which accurately determines the modes of a lattice structure.

LIST OF REFERENCES

(1) Mills, R.A., "Active Vibration Control of a Cantilevered Beam: A Study of Control Actuators," Paper IAF-ST-83-11 of the 34th Congress of the International Astronautical Federation, Budapest, Hungary, October 10-15, 1983.

(2) Garnek, M., "Large Space Structure Analysis Using Substructure Modal Test Data," AIAA Paper 84-0942-CP, May, 1984.

(3) Yousuff, A. and Skelton, R.E., "Controller Reduction by Component Cost Analysis," IEEE Transactions on Automatic Control, Vol. AC-29, No. 6, June, 1984, pp. 520-530.

(4) Przemieniecki, J.S., Theory of Matrix Structural Analysis, McGraw-Hill, New York, 1968.

(5) Craig, R.R., Structural Dynamics, John Wiley & Sons, New York, 1981.

(6) Noor, A.K., Anderson, M.S., and Greene, W.H., "Continuum Models for Beam- and Platelike Lattice Structures," AIAA Journal, Vol. 16, No. 12, December, 1978, pp. 1219-1228.

(7) Anderson, M.S., "Vibration of Prestressed Periodic Lattice Structures," AIAA Journal, Vol. 20, No. 4, April, 1982, pp. 551-555.

(8) Howson, W.P. and Williams, F.W., "Natural Frequencies of Frames with Axially Loaded Timoshenko Members," Journal of Sound and Vibration, Vol. 26, No. 4, 1973, pp. 503-515.

(9) Berry, D.T., Yang, T.Y., and Skelton, R.E., "Dynamics and Control of Lattice Beams Using Complex and Simplified Finite Element Models," Proceedings of the AIAA/ASME/ASCE/AHS 25th Structures, Structural Dynamics and Materials Conference, Palm Springs, Calif., May 14-16, 1984, pp. 422-430.

(10) Leung, A. Y.-T., "Dynamic Analysis of Periodic Structures," Journal of Sound and Vibration, Vol. 72, No.4, September-October, 1980, pp. 451-468.

(11) Schroeder, R.A., Dynamic Analysis of a Two-Dimensional Lattice Structure, M.I.T. Department of Mechanical Engineering Master's thesis, May, 1983.

(12) Regelbrugge, M.E. and Park, K.C., "Local-Global Interactions in the Transient Response of Lattice -Truss Plates," AIAA Paper 84-0945-CP, February, 1984.

(13) Vander Velde, W.E. and Carignan, C.R., "Number and Placement of Control System Components Considering Possible Failures," Journal of Guidance, Control, and Dynamics, Vol. 7, No. 6, November-December, 1984, pp. 703-709.

(14) Juang, J.-N. and Rodriguez, G., "Formulations and Applications of Large Structure Actuator and Sensor Placements," Proceedings of the Second VPI&SU/AIAA Symposium on Dynamics and Control of Large Flexible Spacecraft, Blacksburg, Va., June 21-23, 1979, pp. 247-262.

(15) Saucy, Y. and Vigneron, T.R., "Identification of Structural Properties of a Continuous Longeron Space Mast," Proceedings of The AIAA/ASME/ASCE/AHS 25th Structures, Structural Dynamics and Materials Conference, Palm Springs, Calif., May 14-16, 1984, pp. 130-139.

APPENDIX A

SADE Sensor Placement

This appendix outlines a scheme for instrumenting the Structural Assembly Demonstration Experiment (SADE) truss to obtain structural dynamics data on a Space Shuttle flight. The type, number, and placement of sensors is considered. Since the truss would extend from the Shuttle bay, impulse force inputs could be applied to the base of the truss by the Shuttle attitude control system for lower mode excitation. Actuators could be used on the truss to excite higher modes.

To obtain the global modes of the truss, sensors should be placed only at the joints of the truss. Placing sensors on the bars would not give results which would be useful for obtaining global modes except for the lowest few modes, since in many modes the bars vibrate relative to the joints, as explained in Chapters 6 and 7. Therefore, sensors for obtaining global modes would be placed only at cross-sectional stations along the truss (along the X dimension in Figure 1) where joints occur. The first bending mode deflections of the bars could be obtained by placing two accelerometers at the center of each bar, normal to the bar and to each other. However, the bar deflections could probably be measured adequately and less expensively by placing strain guages at the centers of the bars. To find the bar vibration modes, sensors would probably be needed at only a few of the longer diagonal bars and a few of the shorter, 55 inch bars (see Figure 1). However, these modes might be impossible to separate since the rigid-jointed finite element models indicate that they are closely spaced.

Six accelerometers would be needed at a given cross-sectional station to determine the global mode characteristics at that station. Three mutually orthogonal accelerometers would be placed at each of two diagonally opposite joints at the station. For example, for the station at the free end of the truss, at X=385, inches (see Figure 1), three accelerometers would be placed at each of nodes 29 and 32 or nodes 30 and 31. The accelerometers at a given joint would be aligned with the X, Y, and Z directions. The two X accelerometers at diagonally opposite joints of a station would sense axial motion and be able to distinguish an axial mode from a bending mode. For an axial mode, the readings from the two X accelerometers would be in phase but for a bending mode they would be out of phase, except when the neutral axis for bending passed through the two joints with the accelerometers. To accomodate this case, accelerometers at successive stations could be placed at joints which define orthogonal axes. For example, if the accelerometers at X=330 inches were placed at diagonally opposite nodes 26 and 26, the accelerometers at X=385 inches would be placed at diagonally opposite nodes 29 and 32. The Y and Z accelerometers at a station would yield the magnitude and direction of bending at that station and an average torsional deflection for that cross-section which would be used to obtain the torsional modes. However, more accelerometers would be needed if the state of distortion of the cross section were desired.

The number of stations to be instrumented would depend on cost versus accuracy and the number of modes desired. There are seven stations where accelerometers could be placed (discounting the station at the base of the truss, at X=0), so the maximum number of accelerometers which could be used for obtaining the global modes would be forty-two. Vander Velde and Carignan (reference 13) and Juang and Rodriguez (reference 14) present methods for obtainig optimum sensor locations for a given number of sensors, based on the minimization of the state estimation error. These methods could be used to determine the best X stations for accelerometer placement if less than seven stations were instrumented. However, for this relatively short truss, it might be more practical to place the sensors at stations equal distances apart, as was done for the Astromast (reference 15). In any case, it would certainly be desirable to place sensors at the station at the free end of the truss because large deflections could be expected there in the lower modes, especially since the truss supports a relatively large tip mass.

APPENDIX B

Coupled Timoshenko Equations for a Cantilevered Beam-Like Structure

The strain energy U for a beam of length L can be expressed as

$$U = \tfrac{1}{2}\int_0^L \underline{\varepsilon}^T \underline{C\varepsilon} \, dX \qquad \text{(B.1)}$$

This equation is the continuum analog of (3.39), which is applicable to a discretized structure. $\underline{C}$ is given by (3.40), and $\underline{\varepsilon}$ is defined by

$$\underline{\varepsilon}^T = \begin{bmatrix} \frac{du}{dX} & \frac{d\psi}{dX} & \frac{d\phi}{dX} & (\frac{dv}{dX} - \psi) & (\frac{dw}{dX} + \phi) & \frac{d\theta}{dX} \end{bmatrix} \qquad \text{(B.2)}$$

where u, v, and w are the translations in the X, Y, and Z directions, respectively, and θ, ϕ, and ψ are the rotations about X, Y, and Z, respectively. Also let p_X, p_Y, and p_Z be forces per unit length and m_X, m_Y, and m_Z be moments per unit length with the obvious senses. Let P_X, P_Y, and P_Z be concentrated forces at X=L, and let M_X, M_Y, and M_Z be concentrated moments at X=L.

The first variation of the total energy of the system must equal zero:

$$\delta\Pi = \delta U - \delta W = 0 \qquad \text{(B.3)}$$

where Π is the total energy. δU, the first variation of the strain energy, can be found by expanding (B.1), taking the first variation of the resulting scalar integral expression, and then integrating by parts. The resulting expression contains an integral portion and boundary terms. The first variation of the work W is

$$\delta W = \int_0^L (p_X\delta u+p_Y\delta v+p_Z\delta w+m_X\delta\theta+m_Y\delta\phi+m_Z\delta\psi)\,dX$$

$$+P_X\delta u(L)+P_Y\delta v(L)+P_Z\delta w(L)+M_X\delta\theta(L)+M_Y\delta\phi(L)+M_Z\delta\psi(L) \qquad (B.4)$$

Substituting for δU and δW in (B.3) yields the six coupled Timoshenko equations for the cantilevered beam and six natural boundary conditions at X=L:

$$C_{11}\frac{d^2u}{dX^2}+C_{12}\frac{d^2\psi}{dX^2}+C_{13}\frac{d^2\phi}{dX^2}+C_{14}\frac{d}{dX}\left(\frac{dv}{dX}-\psi\right)+C_{15}\frac{d}{dX}\left(\frac{dw}{dX}+\phi\right)+C_{16}\frac{d^2\theta}{dX^2} = -p_X$$

$$C_{14}\frac{d^2u}{dX^2}+C_{24}\frac{d^2\psi}{dX^2}+C_{34}\frac{d^2\phi}{dX^2}+C_{44}\frac{d}{dX}\left(\frac{dv}{dX}-\psi\right)+C_{45}\frac{d}{dX}\left(\frac{dw}{dX}+\phi\right)+C_{46}\frac{d^2\theta}{dX^2} = -p_Y$$

$$C_{15}\frac{d^2u}{dX^2}+C_{25}\frac{d^2\psi}{dX^2}+C_{35}\frac{d^2\phi}{dX^2}+C_{45}\frac{d}{dX}\left(\frac{dv}{dX}-\psi\right)+C_{55}\frac{d}{dX}\left(\frac{dw}{dX}+\phi\right)+C_{56}\frac{d^2\theta}{dX^2} = -p_Z$$

$$C_{16}\frac{d^2u}{dX^2}+C_{26}\frac{d^2\psi}{dX^2}+C_{36}\frac{d^2\phi}{dX^2}+C_{46}\frac{d}{dX}\left(\frac{dv}{dX}-\psi\right)+C_{56}\frac{d}{dX}\left(\frac{dw}{dX}+\phi\right)+C_{66}\frac{d^2\theta}{dX^2} = -m_X$$

$$C_{13}\frac{d^2u}{dX^2}-C_{15}\frac{du}{dX}+C_{23}\frac{d^2\psi}{dX^2}-C_{25}\frac{d\psi}{dX}+C_{33}\frac{d^2\phi}{dX^2}+C_{34}\frac{d}{dX}\left(\frac{dv}{dX}-\psi\right)-C_{35}\frac{d\phi}{dX}$$

$$+C_{35}\frac{d}{dX}\left(\frac{dw}{dX}+\phi\right)+C_{36}\frac{d^2\theta}{dX^2}-C_{45}\left(\frac{dv}{dX}-\psi\right)-C_{55}\left(\frac{dw}{dX}+\phi\right)-C_{56}\frac{d\theta}{dX} = -m_Y$$

$$C_{12}\frac{d^2u}{dX^2}+C_{14}\frac{du}{dX}+C_{22}\frac{d^2\psi}{dX^2}+C_{23}\frac{d^2\phi}{dX^2}+C_{24}\frac{d\psi}{dX}+C_{24}\frac{d}{dX}\left(\frac{dv}{dX}-\psi\right)+C_{25}\frac{d}{dX}\left(\frac{dw}{dX}+\phi\right)$$

$$+C_{26}\frac{d^2\theta}{dX^2}+C_{34}\frac{d\phi}{dX}+C_{44}\left(\frac{dv}{dX}-\psi\right)+C_{45}\left(\frac{dw}{dX}+\phi\right)+C_{46}\frac{d\theta}{dX} = -m_Z$$

At X=L,

$$C_{11}\frac{du}{dX}+C_{12}\frac{d\psi}{dX}+C_{13}\frac{d\phi}{dX}+C_{14}\left(\frac{dv}{dX}-\psi\right)+C_{15}\left(\frac{dw}{dX}+\phi\right)+C_{16}\frac{d\theta}{dX} = P_X$$

$$C_{14}\frac{du}{dX}+C_{24}\frac{d\psi}{dX}+C_{34}\frac{d\phi}{dX}+C_{44}\left(\frac{dv}{dX}-\psi\right)+C_{45}\left(\frac{dw}{dX}+\phi\right)+C_{46}\frac{d\theta}{dX} = P_Y$$

$$C_{15}\frac{du}{dX}+C_{25}\frac{d\psi}{dX}+C_{35}\frac{d\phi}{dX}+C_{45}\left(\frac{dv}{dX}-\psi\right)+C_{55}\left(\frac{dw}{dX}+\phi\right)+C_{56}\frac{d\theta}{dX} = P_Z$$

$$C_{16}\frac{du}{dX}+C_{26}\frac{d\psi}{dX}+C_{36}\frac{d\phi}{dX}+C_{46}\left(\frac{dv}{dX}-\psi\right)+C_{56}\left(\frac{dw}{dX}+\phi\right)+C_{66}\frac{d\theta}{dX} = M_X$$

$$C_{13}\frac{du}{dX}+C_{23}\frac{d\psi}{dX}+C_{33}\frac{d\phi}{dX}+C_{34}\left(\frac{dv}{dX}-\psi\right)+C_{35}\left(\frac{dw}{dX}+\phi\right)+C_{36}\frac{d\theta}{dX} = M_Y$$

$$C_{12}\frac{du}{dX}+C_{22}\frac{d\psi}{dX}+C_{23}\frac{d\phi}{dX}+C_{24}\left(\frac{dv}{dX}-\psi\right)+C_{25}\left(\frac{dw}{dX}+\phi\right)+C_{26}\frac{d\theta}{dX} = M_Z$$

Sub-appendices C and D of Appendix C have not been included in this report for the sake of brevity. Sub-appendix C lists in tabular form the eigenvalues and eigenvectors of the SADE structure. Sub-appendix D contains program listings for the analyses presented in Appendix C. Readers interested in these details should contact the MIT Space Systems Laboratory, and request SSL Report 12-85.